PONTIFICIA UNIVERSIDAD CATOLICA DE CHILE

SCHOOL OF ENGINEERING

MINERAL ADMIXTURE-BASED RHEOLOGICAL DESIGN OF CONCRETE

IVAN NAVARRETE LESCHOT

Thesis submitted to the Office of Graduate Studies in partial fulfillment of the requirements for the Degree of Doctor in Engineering Sciences

Advisors:

MAURICIO LOPEZ

YAHYA KURAMA

Santiago de Chile, April, 2021

PONTIFICIA UNIVERSIDAD CATOLICA DE CHILE
SCHOOL OF ENGINEERING

MINERAL ADMIXTURE-BASED RHEOLOGICAL DESIGN OF CONCRETE

IVÁN IGNACIO NAVARRETE LESCHOT

Members of the Committee:

MAURICIO LÓPEZ

YAHYA KURAMA

BRAD WELDON

ÁLVARO PAÚL

WERNHER BREVIS

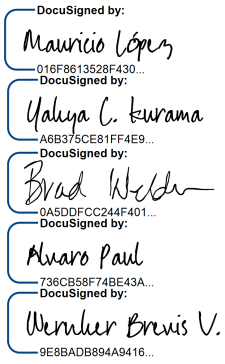

Thesis submitted to the Office of Graduate Studies in partial fulfillment of the requirements for the Degree Doctor in Engineering Sciences

Santiago de Chile, April, 2021

ACKNOWLEDGMENTS

I would like to thank my mother Janine, my father Ivan, my sister Catalina, my girlfriend Maria Ignacia, and my friends for their continuous support and encouragement during this process. Thank you for encouraging me to follow my dreams, even when that means that we will not be together for a long time. In addition, I want to dedicate this work to my aunt Marisa and my grandmother Angela, who are the stars that guide my path.

I would like to express my gratitude to my advisors, Drs. Mauricio Lopez and Yahya Kurama, for their guidance, support, and for always looking out for my personal and professional wellbeing. In addition, I want to acknowledge the assistance and commentaries of Drs. Wernher Brevis and Nestor Escalona. Thank you also to the faculty, staff, thesis readers, and fellow students of Pontificia Universidad Catolica de Chile and the University of Notre Dame, especially to Mauricio Guerra, Luis Gonzalez, and Brent Bach for your support during the experimental work.

Finally, I would like to thank the financial support of ANID/PCHA/Doctorado Nacional/2017-21170247, ANID/FONDECYT 1190641, ANID/FONDEF VIU16E0094, and the Department of Civil and Environmental Engineering and Earth Sciences of the University of Notre Dame.

MINERAL ADMIXTURE-BASED RHEOLOGICAL DESIGN OF CONCRETE

Abstract

by

Ivan Navarrete Leschot

The use of supplementary cementitious materials (SCMs; e.g., slag, fly ash) to reduce the amount of ordinary Portland cement in concrete construction has increased significantly over the last 20 years. Previous research has shown that, as an important benefit, SCMs can improve the long-term mechanical properties and durability of concrete. However, there is limited and inconclusive information on the relationship between SCM properties and concrete workability. This is particularly important for technologies that require high workability control, such as self-consolidating concrete (SCC).

This thesis provides an experimental-based quantitative assessment and understanding of the effects of the particle size and physicochemical properties of SCMs and their interactions with the primary mixture parameters (such as water-to-cementitious materials ratio, SCM replacement, and reactivity of cement) on the rheology of cementitious paste (i.e., cementitious mixture with no coarse or fine aggregates). The results from this research are intended to improve the mixture design of new construction technologies that require better rheological control, through the use of SCMs. As a specific application, improved design of SCC to achieve better interlayer bonding is investigated. This is important for the construction of large concrete elements, where casting of multiple concrete lifts is required. Specifically, due to the lack of mechanical consolidation when casting SCC, the interfaces between multiple layers can result in reduced mechanical resistance in the final structure.

The specific objectives of this research are to experimentally investigate, develop and validate empirical models for the effects of: 1) SCM properties and their interactions with the primary mixture parameters on the increase of static yield stress on time of cementitious paste before initial set; 2) SCM properties and their interactions with the primary mixture parameters on the viscosity of cementitious paste before initial set; and 3) concrete mixture design (i.e., cementitious paste rheology and aggregate-to-cementitious paste ratio), building process (i.e., layer-to-layer free-fall height and delay time), and their interactions on the layer-to-layer flexural and shear bond strength in multilayer SCC.

CONTENTS

FIGURES

TABLES

CHAPTER 1:

INTRODUCTION

1.1 Motivation

According to a report by the Mckinsey Global Institute (McKinsey Global Institute 2017), the global labor-productivity growth in construction lags far behind that of other manufacturing fields or the total economy. The main reason of the low productivity in the construction industry is the use of traditional construction systems, which are highly labor demanding (Proverbs et al. 1999). In the last several decades, new technologies that can improve the productivity of concrete construction through better workability control (Khayat and Feys 2010; Navarrete et al. 2017a; Wangler et al. 2016), such as self-consolidating concrete (SCC) and 3D concrete printing, have been developed.

The workability of fresh concrete is a very important property that determines how well and easily the material can be mixed, placed, consolidated, and finished. The cementitious paste and its interactions with fine and coarse aggregates govern the workability of concrete and its evolution with time. As such, rheological measurements of

the cementitious paste are reasonable indicators of concrete workability (Ferraris et al. 2001a).

Most of the concrete produced worldwide in current construction contains chemical admixtures, such as viscosity enhancers and high-range water-reducers (i.e., superplasticizers), to improve the rheological properties of concrete and reduce the amount of cement (Roussel 2012). However, the effectiveness of a chemical admixture depends on many factors, including the type and amount of cement, water content, mixing time, and temperatures of the concrete and air (PCA 2018). In addition, the use of high-range water-reducers, one of the most commonly types of chemical admixtures, accelerates the loss of workability over time (Mardani-Aghabaglou et al. 2013). Therefore, it is difficult to predict and control the effect of a chemical admixture on the rheological properties of concrete, which hinders the development of new concrete technologies that require better reliability of workability.

Moreover, the use of blended cements through the introduction of supplementary cementitious materials (SCMs), also known as mineral admixtures (e.g., fly ash, blast furnace slag), in the cement industry has increased significantly over the last three decades. Most SCMs are industrial byproducts, and thus, their use improves the sustainability of concrete. In 1995, only 44% of the cements produced in the United States were blended cements. By 2009, this figure had increased to over 80% (Schneider et al. 2011). Most of

the SCMs possess different surface potentials than cement (Ersoy et al. 2014). Importantly, the adsorption of chemical admixtures onto SCMs is lower than the adsorption onto cement particles, which reduces the effectiveness of chemical admixtures on concretes produced with blended cements (Park et al. 2005). As a result, the amount of cement required in many applications is controlled by concrete workability and not by its strength. This effect is more relevant in new concrete technologies requiring better workability control, such as SCC, which use high amounts of cement, with a detrimental effect on their cost and environmental impacts.

Most of the previous research on SCMs has focused on the effects of these materials on the mechanical properties and durability of concrete. Many studies have found that most SCMs increase the concrete strength at later ages (Bendapudi and Saha 2011; Dhanya et al. 2018). In addition, SCMs reduce the permeability of concrete and, therefore, improve its durability (He and Shi 2008; Juenger and Siddique 2015; Mo et al. 2017; Narasimha Reddy and Kavyateja 2020). On the other hand, fewer studies have focused on the effects of SCMs on concrete workability. Figure 1.1 from previous research shows that SCMs have significant effects on the rheology of cementitious materials, and therefore, on concrete workability. However, contradictory results and trends have been found between different studies on this topic. Ultimately, a deeper understanding of the relationships between the chemical and physical properties of SCMs and the rheology of cementitious paste will improve the mixture design of new concrete construction technologies that

require better workability control. This information may also lead to higher replacements of cement by SCMs, thus reducing the environmental impact and costs of the concrete mixture and resulting in more sustainable construction.

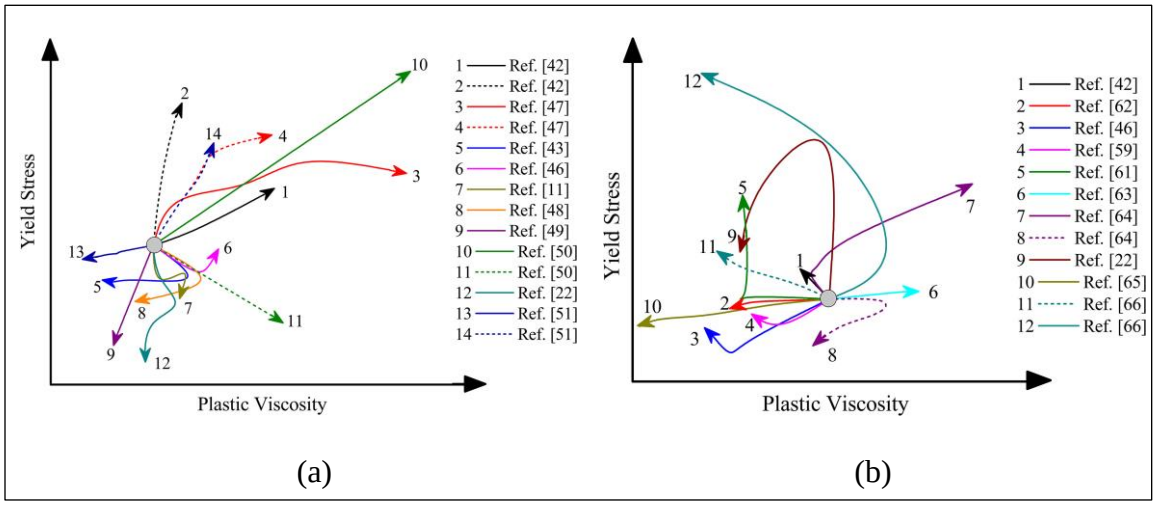

Figure 1.1: Effect of fly ash (a) and blast furnace slag (b) on rheological properties of cementitious materials (Jiao et al. 2017).

Among the new concrete technologies requiring better workability control, self-consolidating concrete (SCC) is the most widely used. The construction of large concrete elements, such as in long wall elements, often require the casting of multiple SCC lifts. In such cases, lack of mechanical consolidation can lead to the formation of distinctly weak interfaces between the successive lifts that are still in the fresh state, which can reduce the mechanical properties and durability of the final concrete product.

Roussel (Roussel and Cussigh 2008) has shown that during placement, a layer of SCC often has a short time (i.e., less than 60 minutes) to rest and flocculate before the next layer of concrete is cast above it. If the fine particles are allowed to flocculate, the structural build-up (A_{thix}) of the concrete at rest increases beyond a critical value, which prevents the two layers to combine, leading to the formation of a weak interface. Losses of layer-to-layer bond strength of more than 40% have been reported, and can exceed 50% when the SCC is highly thixotropic and when the elapsed time between the casting of two layers exceeds 30 minutes (Megid and Khayat 2017, 2019; Roussel and Cussigh 2008).

The bond strength between two successive layers is highly affected by the aggregate interlock and the surface roughness of the first layer (Megid and Khayat 2017), which are mainly governed by the aggregate size, shape and texture, and the aggregate-to-cementitious paste ratio. Surface roughness can be improved by applying external mechanical vibration to the existing concrete layer, which would reduce its yield stress (Chia et al. 2005) and, therefore, increase the bond strength. Another approach would be to increase the free-fall height of the new concrete onto the existing material, which increases the interlock resulting from the penetration of the top concrete layer into the lower layer (Megid and Khayat 2019). However, these methods involving mechanical vibration and increased free-fall height can also cause segregation or bleeding, which can lead to impaired bond between the successive layers.

Previous researchers have studied the individual effects of mixture design (e.g., aggregate-to-cementitious paste ratio (Roussel and Cussigh 2008), rheology of cementitious paste [i.e., A_{thix} (Assaad and Issa 2016; Megid and Khayat 2019)], and construction process [i.e., free-fall height and delay time (Megid and Khayat 2017)] on the layer-to-layer bond strength of multilayer SCC. However, the interactions between these parameters on the bond strength between SCC lifts require further investigation.

1.2 Objectives

In accordance with the research needs and gaps discussed above, the main goal of this research is to assess and understand the fundamental effects and interactions between SCMs and other mixture constituents on the rheology of cementitious paste (i.e., paste with ordinary Portland cement, SCM, and water). Additionally, the findings are applied specifically to SCC, a commonly used concrete technology, for improved layer-to-layer flexural and shear bond strength in multilayer casting. The resulting three specific objectives of the research are as follows:

1. To understand and quantify the effects of the particle size and physicochemical properties of SCMs and their interactions with the primary mixture parameters (such as water-to-cementitious materials ratio, SCM replacement, and reactivity of cement) on the structural build-up (A_{thix}) of cementitious paste before initial set.

2. To understand and quantify the effects of the particle size and type of SCMs and their interactions with the primary mixture parameters on the viscosity of cementitious paste.

3. To assess and quantify the effects of mixture design (i.e., cementitious paste rheology and aggregate-to-cementitious paste ratio), construction process (i.e., free-fall height and delay time), and their interactions on the layer-to-layer bond strength in multilayer casting of SCC.

The results of this research are intended to enhance the fundamental understanding of the SCM properties that affect the rheology of cementitious pastes. Ultimately, this work can lead to better use of SCMs for the control of workability in concrete applications.

1.3 Hypotheses

The following three hypotheses guide this research. The first two hypotheses are related with the first specific objective, while the last hypothesis is related to the second specific objective.

1. A rise in the specific surface area of the supplementary cementitious materials allows for more nucleation points and the growth of hydration products, increasing the rate of growth of yield stress of cement paste.

2. An increase in the hydraulic reactivity of the supplementary cementitious materials accelerate the growth of hydration products, and therefore, increases the rate of growth of yield stress of cement paste.

3. A higher specific surface area of the supplementary cementitious materials produces an increase in the adsorbed water, which rises the solid effective volume fraction; and thus, increasing the cement paste viscosity.

1.4 Approach

To achieve the above objectives, a series of face centered central composite designs (FCCCD) were used to develop a comprehensive experimental program. These designs were chosen due to the resulting efficiency in the number of experimental runs required to effectively analyze the results and trends from experiments with four or more parameters. In the case of objectives 1 and 2, five experimental parameters were studied, while to realize objective 3, four experimental parameters were studied.

The FCCCD is based on an embedded fractional factorial design with center points augmented by a group of axial points, which allow the estimation of curvature in the resulting trends (NIST/SEMATECH 2012). The axial points are at the center of each face of the factorial space and, therefore, three levels (i.e., -, 0 and +) are required in selecting the values for each parameter. This design allows the measured response to be empirically

modelled by a second order polynomial regression (SOPR) equation, which permits the main, quadratic, and interactive effects of the experimental parameters on the property under study to be determined (Montgomery and Runger 2003). Analysis of variance and backward elimination algorithm (Montgomery and Runger 2003) were conducted with the results of the FCCCD to establish the significant factors on the studied properties for each objective and develop SOPR equations. In addition to the FCCCD mixtures tested to develop the SOPR models for each objective, additional samples (i.e., six mixtures for objectives 1 and 2, and four mixtures for objective 3) were characterized to validate these SOPR models. These validations were achieved based on the predicted residual error sum of squares statistic (Montgomery and Runger 2003) calculated using the SORP prediction residuals for the validation mixture data.

1.5 Scope

The study described in this thesis is based on the following considerations:

- The developed relationships are empirical, using the results from testing laboratory mixtures.
- All mixtures are produced at ambient temperature (i.e., 17 to 23 °C).
- Class C fly ash, class F fly ash, metakaolin, rice husk ash, inert silica powder, and slag are used as SCM. These SCMs have similar ranges of particle size distribution as cement. Very fine powders, such as silica fume or nanomaterials, are out of scope.
- Water-to-cementitious materials ratio ranges between 0.40 and 0.50 by mass.

- SCM replacement ranges between 20 and 40% of cement volume.
- A crushed limestone coarse aggregate with maximum aggregate size of 3/8 in. is used in all of the SCC mixtures.
- A high-range water-reducing admixture (i.e., MasterGlenium 7920) is used in all the SCC mixtures.
- Measurements of rheology are made using a TA Discovery Hybrid Rheometer 2. A 25-mm diameter parallel-plate configuration is used, with a smooth stationary base plate, a serrated superior plate, and 1000 μm gap between the plates.
- Viscosity is quantified using the equilibrium flow curve measured 8 min after the contact of cementitious materials with water.
- Structural build-up (A_{thix}) of cementitious paste is quantified by measuring the growth of static yield stress with time. The first measurement is performed 15 min after the contact of cementitious materials with water and repeated every 15 min until 120 min.
- Bond strength in multilayer casting of SCC is characterized on small-scale unreinforced specimens by measuring the shear strength and flexural strength of the bonding plane at 28 days after concrete mixing.

1.6 Outline

This document is written in the format of three independent journal articles produced based on this research, where each chapter is a self-contained paper. The first paper has been published in *Cement and Concrete Research*, while the second paper has

been submitted to the same journal, and the third paper has been submitted to *Construction and Building Materials*. As such, the remaining chapters of this document are organized as follows:

Chapter 2 (journal paper 1; published) aims to assess and understand the effects of particle size and physicochemical properties of five different SCMs and their interactions with the primary mixture parameters on the structural build-up (A_{thix}) of cementitious paste, which is the first specific objective of this research.

Chapter 3 (journal paper 2; submitted) aims to assess and understand the effects of particle size and surface potential of SCMs and their interactions with the primary mixture parameters on the viscosity of cementitious paste, which is the second specific objective of this research.

Chapter 4 (journal paper 3; submitted) aims to assess the effects of the cementitious paste volume, structural build-up of mortar, and their interactions with the casting process (i.e., free fall height and delay time) on the residual bond strength of multi-layer SCC under shear and flexural stresses.

Finally, Chapter 5 repeats (for the convenience of the reader) the conclusions listed at the ends of Chapters 2-4 regarding each specific objective and discusses future directions.

CHAPTER 2:

IMPACT OF PHYSICAL AND PHYSICOCHEMICAL PROPERTIES OF SUPPLEMENTARY CEMENTITIOUS MATERIALS ON STRUCTURAL BUILD-UP OF CEMENT-BASED PASTES

This chapter focuses on the effect of supplementary cementitious material (SCM) particle size and physicochemical behavior, and their interactions with the primary mixture parameters, on the structural build-up (A_{thix}) of cementitious pastes, which is the first specific objective of this research. To this end, a fractional face centered central composite experimental design, composed of 29 mixtures with two SCMs, was conducted. The measurements from these mixtures were then used to develop second order polynomial regression (SOPR) models, which were validated based on the results from 6 additional mixtures with three different SCMs. The increase of static yield stress with time was used to characterize the A_{thix} of cementitious pastes. Calorimetric curves were also measured to characterize the effect of the studied parameters on the growth and nucleation rates of cement.

This chapter includes a detailed characterization of the SCM properties and an assessment of the effect of those properties on A_{thix}. The results demonstrate that the effect of SCMs on A_{thix} is governed by the particle number density and surface potential. In addition, A_{thix} can be increased by increasing the number of particle contact points, the growth rate of calcium silicate hydrate (C-S-H) bridges between particles, and/or the reactivity of cement.

2.1 Introduction

The workability of fresh concrete is a very important property that determines how well the material can be mixed, placed, consolidated, and finished. The cementitious paste and its interaction with the aggregates govern the workability and its evolution with time. As such, rheological measurements of the cementitious paste are reasonable indicators of concrete workability (Ferraris et al. 2001a).

Fresh cement-based materials (CBM) (Jiao et al. 2017), as well as other yield stress fluids (Cheng 1986; Sun and Gunasekaran 2009), exhibit dynamic and static yield stresses. The dynamic yield stress (τ_0^D) is the minimum stress required for maintaining flow and is commonly obtained from the equilibrium flow curve. The static yield stress (τ_0^S) is the stress required to initiate flow (Malvern Instruments 2012). Due to the structural states of these conditions, τ_0^S is expected to be higher than τ_0^D (Qian and Kawashima 2018).

Fresh CBM can be defined as yield stress fluids (Tattersall and Banfill 1983). The main characteristic of these materials is that they behave like solids when the applied stress is below a critical shear stress value, called yield stress, and like liquids if the applied stress is above the yield stress (Roussel 2012). The most common method to measure the rheology of CBM is the equilibrium flow curve, plotted as the equilibrium shear stress versus the shear rate (Qian and Kawashima 2018). The yield stress in this method is equal to the shear stress at a shear rate of zero. Among the constitutive equations that have been proposed to represent the equilibrium flow curve of CBM, the Bingham model (Bingham 1922), the Herschel – Bulckley model (de Larrard et al. 1998), and the modified Bingham model (Yahia and Khayat 2001) are the most common.

The dynamic yield stress, τ_0^D of CBM has been widely studied (Ferraris 1999; Matos et al. 2018; Park et al. 2005; Qian and Kawashima 2018) and been related to measurements from common field tests, such as the slump flow test (Bouvet et al. 2010a; Lu et al. 2015). On the other hand, in the last decade, with the growing use of self-consolidating concrete (SCC) and development of new technologies that require better workability control (Navarrete et al. 2017a; Wangler et al. 2016), such as 3D printing of concrete, more attention has been paid to the static yield stress, τ_0^S.

It has been shown that τ_0^S of fresh CBM at rest increases over time (Mostafa and Yahia 2016; Perrot et al. 2016; Roussel 2006; Tattersall and Banfill 1983). Within a few

minutes at rest, the cement particles flocculate and form a three-dimensional network due to electrostatic and van der Waals forces (Ferron et al. 2013; Yim et al. 2013). In addition, nucleation of C-S-H at the pseudo-contact points between cement and other particles during the dormant period (Mostafa and Yahia 2017; Roussel et al. 2012) generates formation and growth of C-S-H bridges, making τ_0^S of the material to increase.

The term "thixotropy" is often used to describe the increase of τ_0^S of fresh CBM. One of the main properties of thixotropy is that it is a reversible process. However, for CBM at rest, both reversible (i.e., flocculation) and irreversible (i.e., cement hydration bonding, such as C-S-H bridges) processes happen simultaneously (Mostafa and Yahia 2017), and it is not simple to separate these two effects. As such, for CBM, structural build-up (A_{thix}), which involves both reversible and irreversible processes, is a more accurate term than thixotropy (Yuan et al. 2017).

A_{thix} is an important property that affects the constructability and performance of concrete structures. Previous researchers (Bellotto 2013; Bentz et al. 2017) have found that for CBM, setting time is highly influenced by A_{thix}. In the case of SCC, formwork pressure (Assaad and Khayat 2006a; Barnes and Johnston 2003; Roussel 2006), concrete stability after casting (Navarrete and Lopez 2016; Shen et al. 2014), and bond strength in multi-layer casting (Megid and Khayat 2017, 2019; Roussel and Cussigh 2008) are governed by this property. It is also important to control A_{thix} in 3D-printed concrete in order to assure

adequate bonding between the printed layers and adequate strength and stiffness for the layers to withstand the weight of the layers above (Le et al. 2012; Ma and Wang 2018; Malaeb et al. 2015; Panda et al. 2016).

To accurately measure the A_{thix} of cementitious paste at rest, the sample should not be distressed during the test. Previous authors have used either small-amplitude oscillatory shear (SAOS) tests (Ma et al. 2018; Mostafa and Yahia 2017) or growth of static yield stress tests (Bentz et al. 2017; Huang et al. 2019; Lecompte and Perrot 2017; Roussel et al. 2012; Yuan et al. 2018) to measure the development of A_{thix}. SAOS is considered a non-destructive test, which is less invasive and less prone to distressing the sample. On the other hand, the growth of static yield stress test is the most common technique, which according to Yuan et al. (Yuan et al. 2017), provides appropriate testing parameters and gives comparable results with the SAOS test.

The A_{thix} of cementitious paste is affected by mixture parameters, such as the mixture composition, constituent properties, ambient conditions, and shear stress history. Previous studies have shown that increased water-to-cementitious materials volumetric ratio (w/c) reduces A_{thix} (Khayat and Assaad 2007; Mostafa and Yahia 2017). Cement properties, such as fineness (Bentz et al. 2018), electrokinetic behavior (Mostafa and Yahia 2017), and chemical composition (Assaad and Khayat 2004), also affect the change of τ_0^S over time. Temperature has been shown as an important factor as well (Huang et al. 2019;

Petit et al. 2006; Vanhove et al. 2013), where a nonlinear increase in A_{thix} was observed in the range of 10 to 40 C° (Huang et al. 2019). Additionally, Ma et al. (Ma et al. 2018) have shown that the A_{thix} of cement paste is highly affected by the pre-shear and rest condition of the sample.

In current construction technology, most of the concrete produced worldwide contains chemical admixtures, such as viscosity enhancing admixtures and high-range water-reducing admixtures, to improve the rheological properties of concrete and reduce the amount of cement. Several studies (Assaad et al. 2004; Khayat and Assaad 2007; Ma et al. 2018) have shown that the dosage and type of chemical admixtures have considerable effects on the rate of A_{thix}. However, the effectiveness of a chemical admixture depends on many factors, including the cement chemical composition, the mixture design and the mixing process (PCA 2018). Therefore, it is difficult to predict and control the effect of a chemical admixture on the rheological properties of concrete, which hinders concrete technologies that require better control of workability (such as 3D printing).

Supplementary cementitious materials (SCMs), also known as mineral admixtures (e.g., fly ash, silica fume), considerably affect the rheology of CBM as well. Most of the previous studies (Bentz et al. 2012; Burgos et al. 2014; Felekoğlu et al. 2006; Ferraris et al. 2001a; Fuentes et al. 2014; Jiao et al. 2017; Khan et al. 2014; Laskar and Talukdar 2008) have investigated the effect of SCMs on τ_0^D and viscosity of cementitious materials. In

comparison, only a few researchers have studied the effect of SCMs on A_{thix} (Assaad and Khayat 2006b; Bentz et al. 2018; Huang et al. 2019; Saleh et al. 2015; Yuan et al. 2018). Importantly, contradictory results have been found between different studies on this topic. For example, some researchers (Saleh et al. 2015) have found that the use of fly ash and silica fume increases the A_{thix} of SCC, while others (Assaad and Khayat 2004) have found the opposite. A possible explanation of this discrepancy could be the packing density of particles, which depends on the range of the particle size distribution of the whole solid particles network (Kashani et al. 2014). To the best of the authors' knowledge, relationships for the physical and physicochemical properties of SCMs with the A_{thix} of cementitious paste have not been investigated.

2.2 Research significance

In accordance with the research gap identified above, this chapter discusses the effects of the particle size and physicochemical properties of SCMs and their interactions with the primary mixture parameters (such as w/c ratio, SCM replacement, and reactivity of cement) on the A_{thix} of cementitious paste. The results presented in the chapter can contribute to enhance the fundamental understanding of the SCM properties that affect A_{thix}. Ultimately, this work can lead to better usage of SCMs for the control of A_{thix} in CBM at rest for applications such as SCC and 3D-printed concrete.

2.3 Experimental design, materials and methods

2.3.1 Experimental design

The effects of the SCM properties and their interactions with the main design parameters of the cement paste mixture on A_{thix} were experimentally determined using a fractional face centered central composite design (FFCCD). This design was chosen due to the resulting efficiency in the number of required test runs and physical constraints in the levels of the experimental factors (i.e., parameters). The FFCCD is based on an embedded fractional factorial design (FFD) with center points (CP) augmented by a group of axial points (AP), which allow estimation of curvature (NIST/SEMATECH 2012). The AP are at the center of each face of the factorial space and, therefore, three levels (i.e., -, 0 and +) are required in selecting the values for each factor. This design allows the measured response to be modelled by a second order polynomial regression (SOPR) equation, which permits the main, quadratic, and interactive effects of the experimental factors on the property under study to be determined (Montgomery and Runger 2014).

Table 2.1 lists the five experimental factors that were studied as follows: (1) SCM particle size (A); (2) w/c; (3) SCM replacement (R); (4) physicochemical behavior of SCM (D); and (5) cement reactivity (C_R). A 2^{5-1} fractional factorial design with 3 CP, and 2*5 AP were used, resulting in 29 experimental rows (i.e., Series I) as shown in Table 2.2. Six

additional rows (i.e., Series II) were also produced to validate the models developed with the FFCCD.

Table 2.1: Experimental factors and their selected levels

	Levels		
Experimental Factors	-	0	+
SCM particle size, A	100% Fine	50% Fine + 50% Coarse	100% Coarse
w/c (by volume)	1.24	1.39	1.55
SCM replacement, R (%vol)	20	30	40
SCM physicochemical behavior, D	100% IF	50%IF + 50% FFA	100% FFA
Cement reactivity, C_R	100% IPC	50%IPC + 50%OPC	100% OPC

Class F fly ash (FFA) and a silica powder (quartz) inert filler (IF) were used to develop the Series I mixtures. The use of these materials allowed the effects from the SCM particle size (A) and SCM physicochemical behavior (D) to be decoupled. To evaluate the particle size effect, parts of the FFA and IF were ball-milled for 48 h and 7 d, respectively, at 75 RPM to obtain finer materials. The FFA without milling was defined as coarse FFA (FFA-Co), while the milled FFA was defined as fine FFA (FFA-Fi). The non-milled and milled IF were mixed in different proportions to obtain coarse IF (IF-Co) and fine IF (IF-Fi), with the same specific surface area as FFA-Co and FFA-Fi, respectively.

Two cements with different chemical composition but similar particle size distribution (PSD) were used in order to characterize the effect of C_R on A_{thix}.

Class C fly ash (CFA), metakaolin (MK), and rice husk ash (RHA) were used in the Series II mixtures. These SCMs were chosen because, like the FFA and IF, they had similar range of PSDs as cement. The effects from very fine powders, such as silica fume or nanomaterials, on A_{thix} are out of the scope of this research.

The rheological properties of a colloidal suspension, such as cementitious paste, are controlled by the volume proportions of its constituents (Bingham 1922) rather than the mass proportions. Therefore, the replacement of cement by SCM were calculated by volume, resulting in different w/c ratios based on mass.

Analysis of variance (ANOVA) and backward elimination algorithm (Montgomery and Runger 2014) were conducted with the 29 runs of Series I to establish the significant factors on A_{thix} and develop SOPR models. These models were then validated based on the predicted residual error sum of squares (PRESS) statistic (Allen 1971) calculated using the SOPR prediction residuals for the values of A_{thix} from Series II.

Table 2.2: Fractional Face Centered Central Composite Design

Row	Mix code	A	w/c	R	D	C_r=A(w/c)RD
1	IF- Fi -1.24-20-OPC	-	-	-	-	+
2	IF-Co-1.24-20-IPC	+	-	-	-	-
3	IF- Fi -1.55-20-IPC	-	+	-	-	-
4	IF-Co-1.55-20-OPC	+	+	-	-	+
5	IF- Fi -1.24-40-IPC	-	-	+	-	-
6	IF-Co-1.24-40-OPC	+	-	+	-	+
7	IF- Fi -1.55-40-OPC	-	+	+	-	+
8	IF-Co-1.55-40-IPC	+	+	+	-	-
9	FFA- Fi -1.24-20-IPC	-	-	-	+	-
10	FFA-Co-1.24-20-OPC	+	-	-	+	+
11	FFA- Fi -1.55-20-OPC	-	+	-	+	-
12	FFA-Co-1.55-20-IPC	+	+	-	+	+
13	FFA- Fi -1.24-40-OPC	-	-	+	+	+
14	FFA-Co-1.24-40-IPC	+	-	+	+	-
15	FFA- Fi -1.55-40-IPC	-	+	+	+	-
16	FFA-Co-1.55-40-OPC	+	+	+	+	+
17	AP-Fi	-	0	0	0	0
18	AP-Co	+	0	0	0	0
19	AP-1.24	0	-	0	0	0
20	AP-1.55	0	+	0	0	0
21	AP-20	0	0	-	0	0
22	AP-40	0	0	+	0	0
23	AP-IF	0	0	0	-	0
24	AP-FFA	0	0	0	+	0
25	AP-IPC	0	0	0	0	-
26	AP-OPC	0	0	0	0	+
27 - 29	CP	0	0	0	0	0

In addition, the heat of hydration was measured for the mixtures corresponding to the FFD runs, which are the first 16 rows of the FFCCD shown in Table 2.2. Using these results and the boundary nucleation and growth (BNG) model, the effect of the factors on

the formation and growth of C-S-H bridges between the cementitious particles was analyzed.

2.3.2 Materials characterization

A Type I ordinary Portland cement (OPC) and a Type IP blended cement (IPC) conforming to ASTM C150 (ASTM Standard C150/C150M 2016) and ASTM C595 (ASTM International 2019), respectively, were used. The IPC was composed of 80% OPC and 20% IF. Oxide composition [determined by X-ray fluorescence (XRF)] and specific gravity of the cements and SCMs are shown in Table 2.3.

Table 2.3: Chemical characterization and specific gravity of cements and SCMs used in this study.

	Cements		Series I		Series II		
	OPC	IPC	IF	FFA	CFA	RHA	MK
CaO (%)	65.8	52.6	0.21	1.52	17.5	0.71	0.07
SiO_2 (%)	19.3	35.2	98.7	52.7	33.3	70.3	47.2
Al_2O_3 (%)	4.50	3.60	0.01	17.7	19.1	0.06	42.3
SO_3 (%)	2.31	1.84	-	0.46	7.34	-	-
Fe_2O_3 (%)	3.04	2.52	0.61	6.10	3.26	4.14	5.52
MgO (%)	1.07	0.89	0.05	1.30	0.81	-	-
Other minor oxides (%)	1.28	1.17	0.21	4.32	4.69	9.09	2.31
Loss on ignition (%)	2.70	2.16	0.21	15.9	14.0	15.7	2.60
Specific gravity	3.14	3.05	2.69	2.39	2.37	2.14	2.72

A scanning electron microscope (SEM) was used to observe the micro-structure of the SCMs and obtain surface information. The samples were oven dried and coated with gold, and images were taken using a Quanta FEG 250 device with magnifications between 300x and 1,000,000x and an accelerating voltage of 15 kV. Figure 2.1 shows SEM images for the different SCMs with a magnification of 5000x.

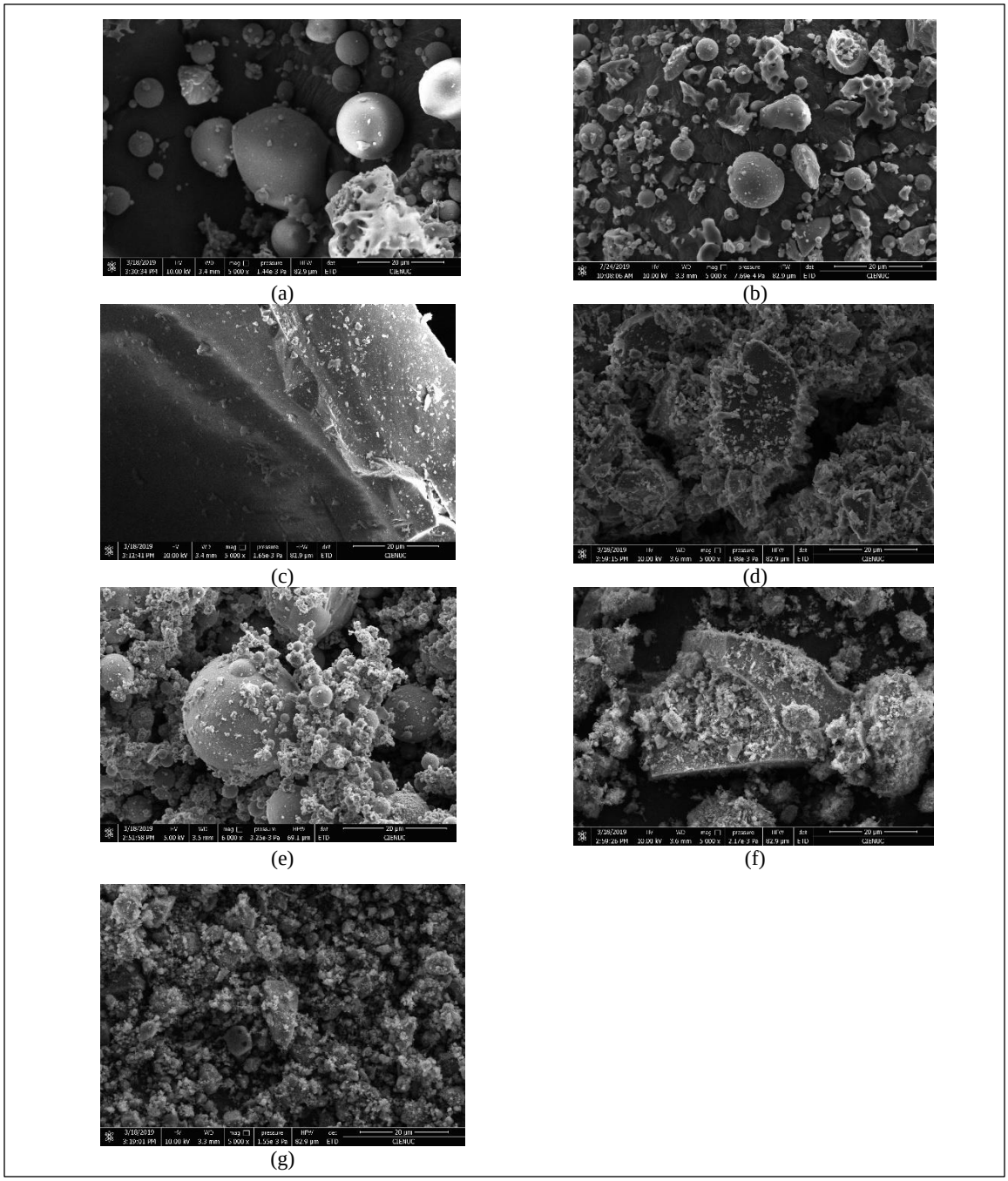

Figure 2.1: 5000x SEM images of FFA-Co (a), FFA-Fi (b), non-milled IF (c), 7-day milled IF (d), CFA (e), MK (f) and RHA (g).

2.3.2.1 Particle size

Figure 2.2 shows the PSDs of the cements and SCMs, measured using a laser diffractometer (Malvern Mastersizer, 2000). The materials were dispersed in isopropanol with a refractive index of 1.378 and each measurement was carried out six times for 10 s at 2000 RPM. For the analysis of PSD in all the samples, a refractive index of 1.458 was used. The D10, D50 and D90 parameters for each PSD are shown in Table 2.4. Figure 2.2.a shows that both OPC and IPC present similar PSDs. In addition, FFA-Fi and IF-Fi are finer than both cements while FFA-Co and IF-Co are coarser than both cements.

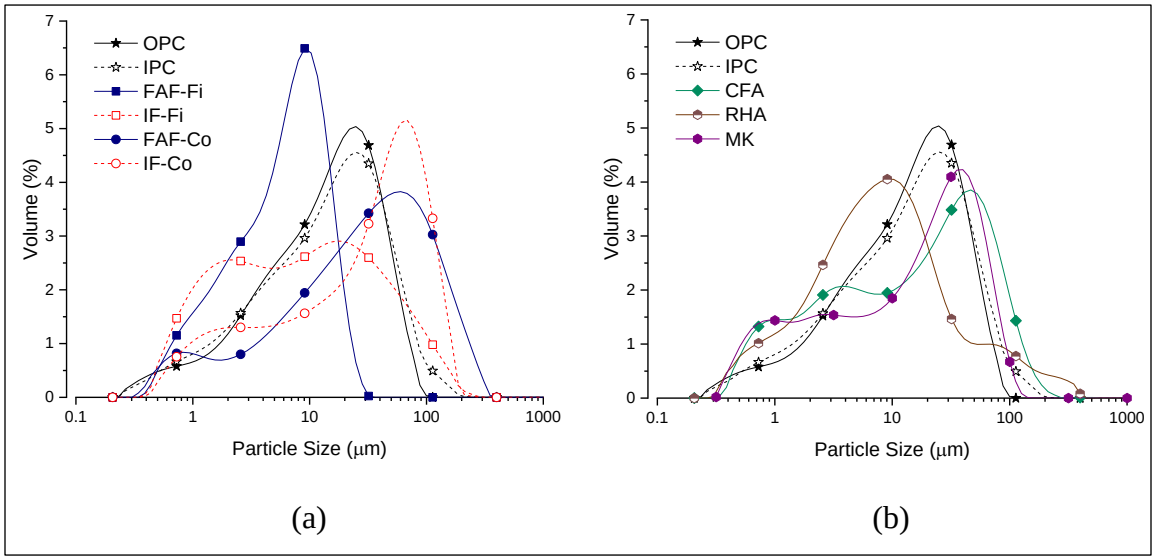

Figure 2.2: Particle size distribution of cements and SCMs in Series I (a) and Series II (b) mixtures.

Based on the PSD of each material and assuming a spherical shape for the particles, the specific surface area per unit volume (SSA_{PSD}) and the particle density (N_{PSD}) can be estimated with the following equations:

$$SSA_{PSD} = \sum_{i=1}^{j} 6V_i/D_i \ [1/\mu m] \quad (2\text{-}1)$$

$$N_{PSD} = \sum_{i=1}^{j} 600V_i/\pi D_i^3 \ [1/100\mu m^3] \quad (2\text{-}2)$$

where, D_i is the average particle diameter between two successive particle sizes (μm), V_i is the volume fraction passing between two successive particle sizes, and j is the number of fractions for a given PSD.

In addition, the BET specific surface area (SSA_{BET}) per unit volume of each material was calculated from the adsorption branch of the isotherms in the range 0.05 to 0.20 of relative pressure, using a 3-FLEX Micrometrics instrument. The estimated SSA_{PSD}, N_{PSD}, and measured SSA_{BET} of all the materials are shown in Table 2.4.

For the experimental runs where both SCM were used (i.e., 50%IF + 50% FFA), the mixtures were produced with different volumetric proportions of FFA-Fi, IF-Fi, FFA-Co, and IF-Co. In these cases, the particle size parameters were calculated as the weighted mean of the SCMs used in each mixture.

The experimental specific surface area (SSA_{BET}) ranges between 3 and 10 times that of the spherically assumed specific surface area (SSA_{PSD}) as shown in Table 2.4. The

SSA_{BET} considered both internal and external surfaces, and no significant differences were found between the SSA_{BET} values of the coarse and fine particles for both FFA and IF. It is important to note that FFA presented a considerable amount of inner pores as seen in the SEM images (Figures 2.1.a and 2.1.b), while no inner pores are visible in the SEM images for IF (Figures 2.1.c and 2.1.d). This may explain the fact that the difference between SSA_{BET} and SSA_{PSD} is smaller for IF than for FFA.

Table 2.4: Particle size parameters of cements and supplementary cementitious materials.

		SSA (m^2/m^3)		D10 (μm)	D50 (μm)	D90 (μm)	N_{PSD} (#/100 μm^3)
		BET	PSD				
Cements	OPC	12	1.30	1.947	13.67	40.69	99.96
	IPC	10	1.30	2.285	16.40	46.27	88.51
Series I	FFA-Fi	10	1.83	1.216	5.943	13.86	56.30
	IF-Fi	4	1.83	1.847	12.94	44.68	62.64
	FFA-Co	10	1.00	2.173	29.48	122.5	52.93
	IF-Co	4	1.00	4.671	35.65	82.34	31.20
Series II	CFA	8	1.56	5.466	41.54	95.34	73.45
	RHA	158	1.71	1.205	7.503	52.90	90.02
	MK	26	1.77	0.959	15.71	54.56	105.2

Since some of the rough regions and inner pores, detected by BET, are too small to function as nucleation points for the hydration products, the parameter SSA_{PSD} is preferred over SSA_{BET}. IF-Fi and IF-Co were produced to match the SSA_{PSD} of FFA-Fi and FFA-Co, respectively, with the aim to decouple the particle size and the physicochemical effects. As such, IF-Fi was produced by combining 15.9% unmilled IF with 84.1% 7-day milled

IF, while IF-Co was produced by combining 67.3% unmilled IF and 32.7% 7-day milled IF.

2.3.2.2 Physicochemical behavior

According to Felekoglu et al. (Felekoğlu et al. 2006), the physicochemical behavior of cements and SCMs is mainly determined by their time-dependent hydration reactions (i.e., cement chemical reactivity (C_R) and SCM chemical reactivity (SCM_R)) and surface potential. Therefore, both properties were selected to characterize the physicochemical behavior of these materials.

2.3.2.2.1 Chemical reactivity at early age

To assess the chemical reactivity of cements and SCMs, isothermal calorimetry tests were carried out using a TAM air isothermal calorimeter at 23 °C for the first three hours after contact of the materials with water. The tests were conducted on samples of cement pastes and SCM pastes, using a w/c ratio by volume of 1.55. The average heat flow of the dormant period of the cement pastes (i.e., C_R) and the average heat flow of the first two hours of the SCM pastes (i.e., SCM_R) were computed, as shown in Table 2.5.

2.3.2.2.2 Surface potential

When colloid particles, such as cementitious materials, contact with an aqueous solution, a firmly attached layer of counter-ions (i.e., ions with an opposite charge than that of the particle surface) is formed around the particle surface. This layer of counter-ions is known as the Stern layer. Around the Stern layer, a diffuse layer of counter-ions is produced, which has a gradually decreasing concentration with distance until reaching equilibrium with the normal counter-ion concentration in the solution (Stern 1924). A schematic representation of the stern and diffuse layers of a negatively charged particle is showed in Figure 2.3.

The surface potential cannot be measured in a simple manner; however, the potential at the junction of the Stern layer and the diffuse layer, which is known as the zeta potential, can be measured in a fairly simple manner (Ravina 1998).

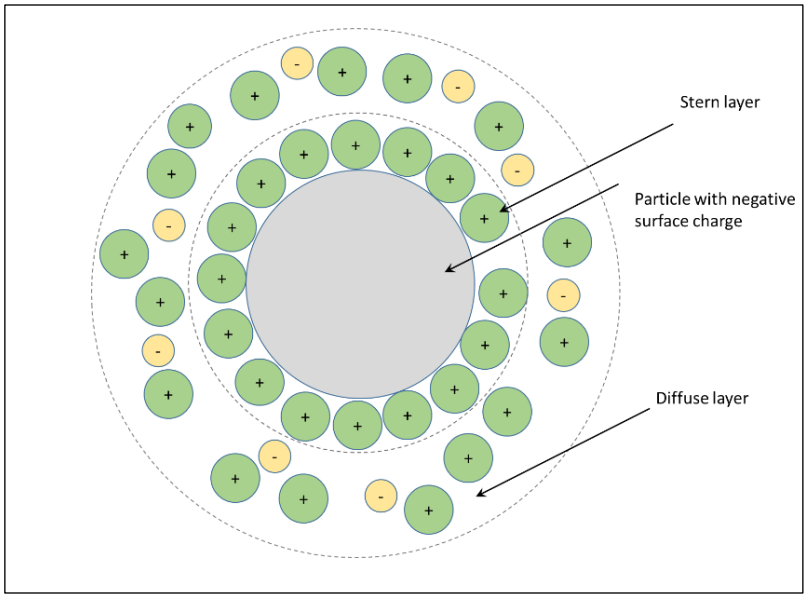

Figure 2.3: Schematic of the Stern layer and diffuse layer of a negatively charged particle.

The ratio between the zeta potential and the surface potential depends on the thickness of the diffuse layer. Solutions with low solids content (i.e., low level of ions) result in a relatively thick diffuse layer. In these cases, the zeta potential is a good approximation of the surface potential. In contrast, solutions with a high concentration of solids have a high level of ions, which compresses the diffuse layer and results in a zeta potential that is only a fraction of the surface potential (Ravina 1998). The valency of the ions also influences the diffuse layer thickness. Specifically, ions with higher valency compress the diffuse layer to a greater extent than monovalent ions. (Zeta-Meter Inc. 1997).

An important focus of this study was the effect of the SCM surface potential on the A_{thix} of cementitious pastes. For this purpose, the zeta potential of each SCM was

determined on the basis of the electrophoresis principle, which is measured in suspensions with low solids concentration, instead of the electroacoustic principle, which enables measurements at high solid concentrations (Lowke and Gehlen 2017).

The electrophoresis results for the zeta potential measured using a Zeta-Meter 3.0 equipment at different pH values are shown in Figure 2.4. An amount of 20 mg for each material was dispersed into 200 mL of background electrolyte solution of $1*10^{-3}$ Mol/L KCl. Most of the previous research studies on the zeta potential of cementitious pastes (Elakneswaran et al. 2009; Ferrari et al. 2010; Lowke and Gehlen 2017; Srinivasan et al. 2010) have used solutions with Ca^{+2} ions to represent the aqueous phase of cementitious pastes and the change in zeta potential due to the reaction of this ion with cementitious materials. However, due to the high ionic valence of Ca^{+2} ions, the zeta potential measured with this method does not represent the surface potential of the powders. Therefore, KOH and HCL electrolytes, which produce monovalent ions, were used in this study to modify the pH values.

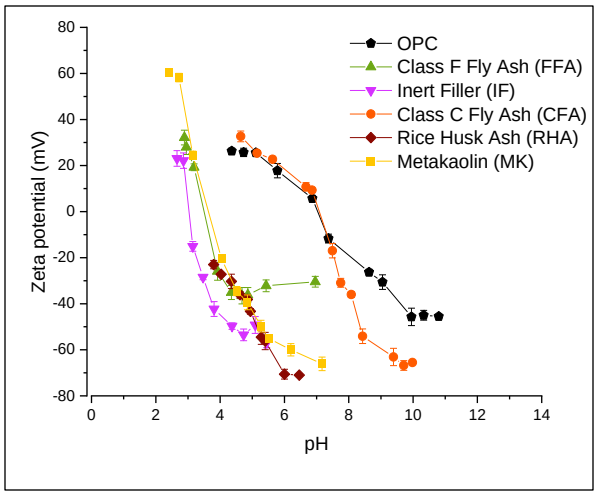

Figure 2.4: pH dependence of the zeta potential of studied powders.

Table 2.5: Chemical reactivity at early age and zeta potential at Ph values larger than 10

		Chemical reactivity (μW/g)	Zeta Potential (mV)
Cements	OPC	300	45.5
	IPC	270	47.1
	50%OPC + 50%IPC*	287	46.3
Series I	IF	0	53.5
	FFA	21	36.2
	50%FFA + 50% IF*	11	44.9
Series II	CFA	23	66.2
	RHA	19	71.0
	MK	8	66.1

Note: * the zeta potential was calculated as the arithmetic mean of the zeta potential of each component.

Fresh cementitious pastes commonly present pH values higher than 12, which is higher than the pH values at which the zeta potential was measured (Figure 2.4). Nägale

(Nägele 1986) measured the zeta potential of cementitious suspensions at different pH values, which were obtained by adding KOH. It was found that when the zeta potential values reach a plateau, further increases in pH result in relatively small changes in the zeta potential. These results are similar to those for non-cementitious colloidal particles (Zhao et al. 2005); therefore, it can be expected that the zeta potential at higher pH values than those experimentally measured would be similar to the plateau values reached for each material, presented in Table 2.5.

2.3.3 Mixture proportions and mixing sequence

Cementitious pastes were mixed and characterized with respect to the evolution of τ_0^S and some of them were also characterized using isothermal calorimetry. The designs of the Series I mixtures were determined according to the FFCCD described in Tables 2.1 and 2.2. For these mixtures, the w/c ratio by volume ranged between 1.24 and 1.55, which is equivalent to a w/c ratio by mass between 0.40 and 0.50. In addition, between 20 and 40% of the cement volume was replaced by SCMs, which is equivalent to mass replacements between 16 and 37%.

The Series II mixture designs are presented in Table 2.6. Six mixtures were produced with different SCMs, w/c ratios, and SCM replacements than those used for the

Series I mixtures. For all the Series II mixtures, the cement was composed of 50% of OPC and 50% of IPC.

The cementitious pastes were all prepared using the same procedure with an electric stirrer. The dry powders were first blended for 5 minutes to homogenize and eliminate any clumps, and then stirred for two minutes after the water was added. The cementitious pastes were mixed at a constant blade speed of 1100 rpm, at laboratory room temperature (i.e., 20 to 23 °C).

Table 2.6: Series II mixture designs.

Mixture	OPC (kg/m^3)	IPC (kg/m^3)	SCM (kg/m^3)	w/c (by vol.)	w/c (by mass)	SCM (% vol. of solids)	SCM (% mass of solids)
CFA-1.33-25	504	490	254	1.33	0.46	25	20
CFA-1.49-25	473	459	238	1.49	0.51	25	20
RHA-1.44-8	591	574	69	1.44	0.48	8	6
RHA-1.44-12	565	549	103	1.44	0.49	12	8
MK-1.33-25	504	490	289	1.33	0.45	25	23
MK-1.49-25	473	459	271	1.49	0.50	25	23

2.3.4 Testing procedures

2.3.4.1 Structural build up test

A parallel plate rheometer (TA Discovery Hybrid Rheometer 2) equipped with a superior 25 mm-serrated plate was used. The gap between the plates was fixed at 1000 μm,

as shown to be adequate by Ferraris (Ferraris et al. 2001b; a) to compare the rheological behavior of different cementitious pastes. As seen in the experiments carried out by Sant et al. (Sant et al. 2008), each specimen was protected from excess evaporation using a chamber with an absorbent sponge soaked with water around it.

The test protocol included the following steps, consistent with procedures used by previous researchers (Sant et al. 2008; Yuan et al. 2017, 2018). At 13 min after the addition of water, the cementitious paste was pre-sheared at 100 s^{-1} for 60 s to attain a reference state. At 15 min, the static yield stress test was performed and repeated every 15 min until 120 min. Each static yield stress test consisted of applying a constant shear rate of 0.015 s^{-1} for 60 s. The peak stress from each test was recorded as the respective τ_0^S. Note that this methodology involving repeated measurements using the same sample may distress the structure of the sample. Thus, A_{thix} could have been underestimated when using a single sample for all the measurements of τ_0^S. This methodology, instead of multiple samples tested at different ages, was chosen because the variability between multiple samples could be large and overshadow the results. Furthermore, according to the results of Yuan et al. (Yuan et al. 2017), the effect of each τ_0^S measurement on the following measurement using the same sample is small.

2.3.4.2 Calorimetric test and boundary nucleation and growth (BNG) model

Isothermal calorimetry tests were conducted to assess the effects of the studied properties on the formation and growth of C-S-H bridges between cementitious particles. The measurements were made using a TAM Air isothermal calorimeter. Heat of hydration was recorded per gram of cement over a period of 12 h at 23°C, beginning approximately 45 minutes after the addition of water.

The heat flow resulting from cement hydration involves several parallel and/or series processes, such as dissolution, growth, nucleation, and complexation (Bullard et al. 2011). The BNG model has been used to describe of hydration kinetics of cement (Honorio et al. 2016; Huang et al. 2019; Oey et al. 2013; Scherer et al. 2012; Thomas 2007; Zhang et al. 2010). This model assumes that: 1) the nucleation and growth rates are constant during the hydration process, 2) the nucleation of C-S-H bridges happens randomly on the surfaces of the cement particles, and 3) the nucleation and growth start at the time of addition of water and continue during the induction period.

According to the BNG model, the volume fraction of hydrates, (X(t)) can be obtained from Eq. (2-3) (Huang et al. 2019; Scherer et al. 2012).

$$X(t) = 1 - \exp\left\{-2K_G t \int_0^1 [1 - \exp(-K_N t^3 (1-\mu)^2 (1+2\mu)]\, d\mu\right\} \quad (2\text{-}3)$$

where, t is the age of cement paste in hours, K_N and K_G are two independent rate constants that describe the kinetics of a boundary-nucleated process, and μ is a dummy variable.

The BNG model fits the calorimetric data well, and the heat flow can be defined as A(dx/dt), where A is a scaling parameter (Honorio et al. 2016; Huang et al. 2019; Oey et al. 2013; Scherer et al. 2012; Thomas 2007; Zhang et al. 2010). In this study, the measured heat flow, mainly the data between the minimum point in the induction period and the peak of the acceleration period, were used to determine K_N and K_G.

2.4 Results and discussions

2.4.1 Growth of static yield stress in time

Figure 2.5 shows the τ_0^S measurements up to a maximum value of 1000 Pa. Even though some of the mixtures reached τ_0^S values above 1000 Pa, those results are not included in Figure 2.5 so as to show the earlier measurements in better detail. All of the mixtures presented two stages: first a stage showing a linear increase in τ_0^S and then a stage showing an accelerated increase in τ_0^S. This trend follows the behavior reported by previous

researchers (Bentz et al. 2017; Lecompte and Perrot 2017; Yuan et al. 2017, 2018). The difference between the linear and accelerated evolutions in τ_0^S was attributed to the increase in the solid volume fraction and the decrease in the packing fraction due to cement hydration (Lecompte and Perrot 2017) and to the increase of specific surface area during the acceleration period of hydration (Mantellato et al. 2019).

The plots in Figure 2.5 show linear fits for both stages, whose slopes were used to calculate A_{thix} for the initial linear stage of τ_0^S (i.e., A_{thix}^1) and for the subsequent accelerated stage of τ_0^S (i.e., A_{thix}^2). These results are summarized in Table 2.7 for each mixture.

The intersection between the two linear fits can be associated with the end of the linear stage of τ_s. For the majority of the Series I mixtures, the range of linear stage in τ_0^S extended between 50 and 65 minutes of rest. Meanwhile, the Series II mixtures presented a linear stage in τ_0^S extending between 15 and 70 minutes of rest. Similar results were obtained by Lecompte and Perrot (Lecompte and Perrot 2017).

Table 2.7 shows that by changing the main mixture design parameters and the SCM properties, it was possible to obtain a wide range of A_{thix}; that is, A_{thix}^1, ranging between 0.34 and 4.21 Pa/min, and A_{thix}^2, ranging between 0.89 and 38.9 Pa/min.

In addition, the results in Table 2.7 indicate a strong correlation between A^1_{thix} and A^2_{thix}. An ANOVA showed that 82% of the observed variability in A^2_{thix} can be explained with A^1_{thix}. Both A^2_{thix} and A^1_{thix} are governed by cement nucleation, but A^2_{thix} is also affected by the solid volume fraction (Lecompte and Perrot 2017), which is out of the scope of this research. In addition, for the concrete technologies of interest in this chapter, such as 3D printing and SCC, the increase of τ_0^S within the first hour is more relevant than the changes produced in later times. Thus, the analysis of the following sections is focused on the A^1_{thix} results.

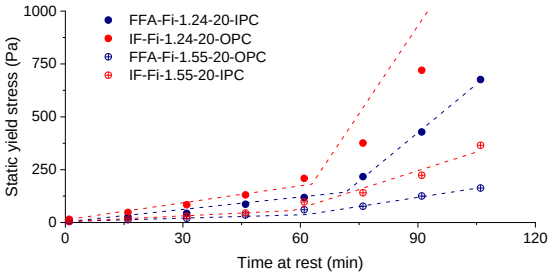

(a) Series I 20% replacement of fine SCM

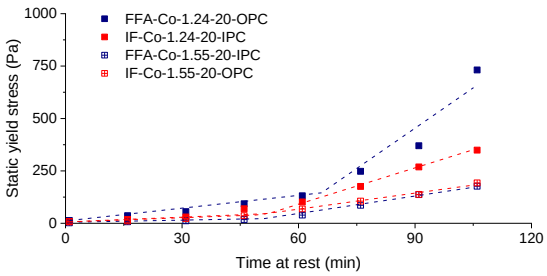

(b) Series I 20% replacement of coarse SCM

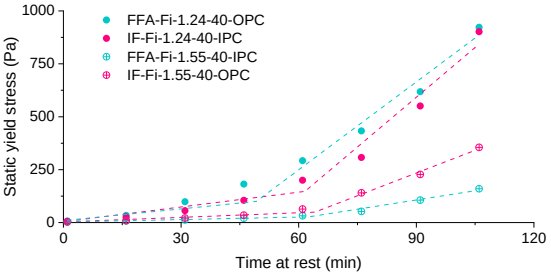

(c) Series I 40% replacement of fine SCM

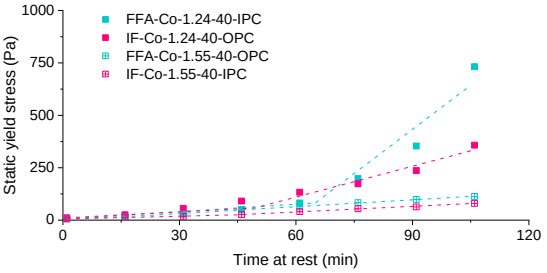

(d) Series I 40% replacement of coarse SCM

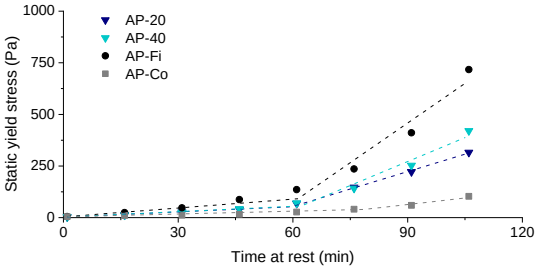

(e) Series I AP SCM size and replacement

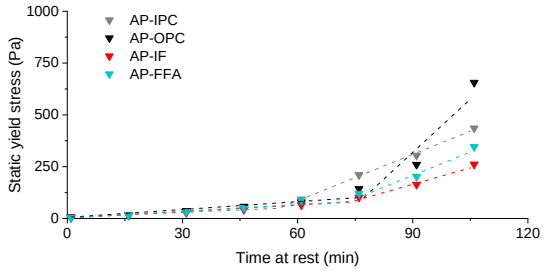

(f) Series I AP SCM physicochemical behavior and cement reactivity

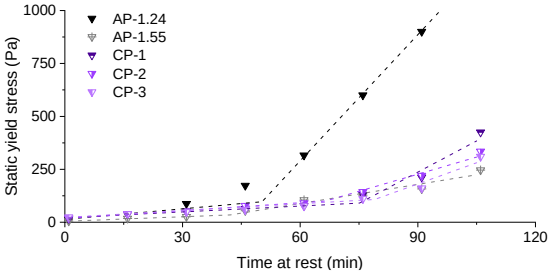

(g) Series I AP w/c and CP

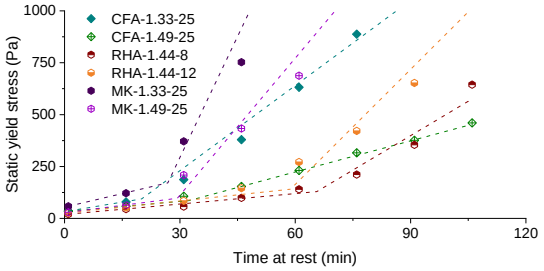

(h) Series II

Figure 2.5: Growth of static yield stress with time.

Table 2.7: A^1_{thix} and A^2_{thix} results

	Mix code	A^1_{thix} (Pa/min)	A^2_{thix} (Pa/min)
Series I	IF- Fi -1.24-20-OPC	2.65	27.6
	IF-Co-1.24-20-IPC	0.78	5.77
	IF- Fi -1.55-20-IPC	0.89	5.91
	IF-Co-1.55-20-OPC	0.67	2.55
	IF- Fi -1.24-40-IPC	2.46	15.7
	IF-Co-1.24-40-OPC	0.71	4.90
	IF- Fi -1.55-40-OPC	0.71	7.15
	IF-Co-1.55-40-IPC	0.42	0.89
	FFA- Fi -1.24-20-IPC	1.93	15.3
	FFA-Co-1.24-20-OPC	2.00	12.8
	FFA- Fi -1.55-20-OPC	0.53	2.88
	FFA-Co-1.55-20-IPC	0.34	2.77
	FFA- Fi -1.24-40-OPC	1.81	13.8
	FFA-Co-1.24-40-IPC	1.15	14.0
	FFA- Fi -1.55-40-IPC	0.38	2.91
	FFA-Co-1.55-40-OPC	0.73	1.09
	AP-Fi	1.40	12.8
	AP-Co	0.44	2.09
	AP-1.24	1.62	19.9
	AP-1.55	0.69	3.02
	AP-20	0.82	5.63
	AP-40	0.85	7.73
	AP-IF	1.03	5.28
	AP-FFA	1.06	7.54
	AP-IPC	0.78	7.48
	AP-OPC	1.25	17.1
	CP-1	0.91	9.82
	CP-2	1.22	5.39
	CP-3	1.06	6.65
Series II	CFA-1.3-25	2.59	13.7
	CFA-1.5-25	1.57	4.99
	RHA-1.4-8	1.65	11.0
	RHA-1.4-12	1.93	18.5
	MK-1.3-25	4.21	38.9
	MK-1.5-25	2.31	22.2

2.4.2 Structural build-up assessment

SOPR models were investigated to correlate the A_{thix}^{1} results with the SCM properties and main mixture designs parameters. The backward elimination algorithm was used to establish factors with a significance level of 95% in explaining the A_{thix}^{1} results.

Previous studies (Assaad and Khayat 2004; Bentz et al. 2012, 2017, 2019; Mostafa and Yahia 2017) have shown that SSA_{PSD} and SCM_R significantly affect the early age properties of cementitious materials. Therefore, SSA_{PSD} and SCM_R were used to represent the particle size and the physicochemical properties of SCM in the development of the first SOPR model, which is represented in Eq. (2-4). Table 2.8 presents a summary of this model and the coefficients (i.e., $\alpha_1 .. \alpha_{11}$) for the significant variables.

$$A_{thix}^{1} = \alpha_1 SSA_{PSD} + \alpha_2 (W/C) + \alpha_3 R + \alpha_4 C_R + \alpha_5 (W/C)^2 + \alpha_6 SSA_{PSD}(W/C) + \alpha_7 SSA_{PSD} SCM_R + \alpha_8 (W/C) R + \alpha_9 (W/C) SCM_R + \alpha_{10} R C_R + \alpha_{11} SCM_R C_R \quad (2\text{-}4)$$

Comparisons between the experimental and predicted results is shown in Figure 2.6. This model was able to explain most of the variability in A_{thix} for the Series I mixtures; however, it was not a good predictor of the results for the validation set of data (Series II mixtures). In fact, the Series II mixtures resulted in a PRESS value of -1.57. Therefore, the

individual effect and the interaction of the selected parameters did not provide a good representation for A_{thix}^{1}.

Table 2.8: First proposed SOPR model summary and coefficients results.

	Coefficient	Standardized Coefficient	Standard error	T-statistic	P-value	95% C.I (±)
α_1	+ 1.03 x10^{1}	+ 12.1	1.35 x10^{0}	+ 7.66	0.000	2.87 x10^{0}
α_2	- 2.23 x10^{1}	- 25.1	3.14 x10^{0}	- 7.09	0.000	6.70 x10^{0}
α_3	+ 2.07 x10^{-1}	+ 5.18	5.72 x10^{-2}	+ 3.61	0.003	1.22 x10^{-1}
α_4	+ 5.01 x10^{-2}	+ 11.5	7.74 x10^{-3}	+ 6.48	0.000	1.65 x10^{-2}
α_5	+ 8.30 x10^{0}	+ 13.3	1.20 x10^{0}	+ 6.94	0.000	2.55 x10^{0}
α_6	- 3.75 x10^{0}	- 6.15	4.51 x10^{-1}	- 8.31	0.000	9.61 x10^{-1}
α_7	- 5.30 x10^{-2}	- 0.84	6.67 x10^{-3}	- 7.95	0.000	1.42 x10^{-2}
α_8	- 1.33 x10^{-2}	- 4.44	4.35 x10^{-3}	- 3.06	0.008	9.27 x10^{-3}
α_9	+ 4.28 x10^{-2}	+ 1.50	1.88 x10^{-2}	+ 2.28	0.038	4.01 x10^{-2}
α_{10}	- 3.80 x10^{-2}	- 0.58	1.64 x10^{-2}	- 2.31	0.035	3.50 x10^{-2}
α_{11}	- 9.63 x10^{-4}	- 6.88	1.84 x10^{-4}	- 5.23	0.000	3.90 x10^{-4}
α_{12}	+ 4.42 x10^{-4}	+ 1.38	8.50 x10^{-5}	+ 5.20	0.000	1.81 x10^{-4}

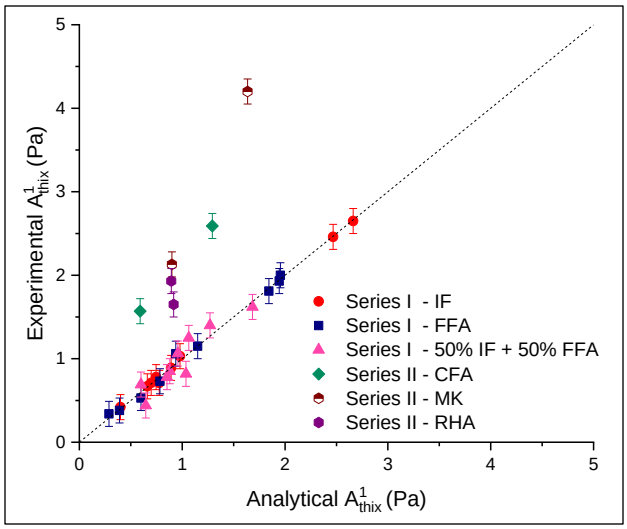

Figure 2.6: Comparisons between experimental A_{thix}^1 and analytical A_{thix}^1 determined with the first SOPR model. R^2 of the Series II attained -1.57 using Equation (2-4).

Figure 2.7 shows three scenarios of cementitious mixtures composed by the same solid volume fraction and replacement of cement by SCM. The scenarios in Figures 2.7.a and 2.7.b present the same N_{PSD} and different SSA_{PSD} of the SCM. It can be appreciated that the number of contact points, which is related to the amount of C-S-H bridges, is similar in both cases. On the other hand, Figure 2.7.b and 2.7.c show scenarios with the same SSA_{PSD} and different N_{PSD} of the SCM. In this comparison, the number of contact points and, therefore, the amount of C-S-H bridges is higher in Figure 2.7.c, which presents a higher N_{PSD}.

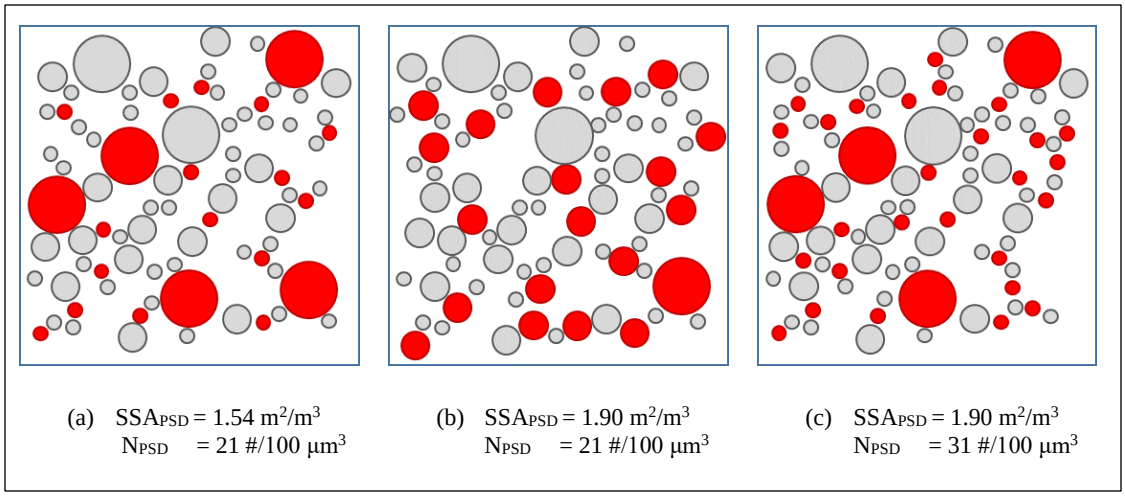

Figure 2.7: Comparison between SCM with the same SSA_{PSD} and different N_{PSD}. Red and gray circles represent SCM and cement particles, respectively.

A higher amount of C-S-H bridges per unit volume of paste increases the rigidification rate of the particles network and; thus, it can be related to a higher A^1_{thix}. Therefore, for the development of the second SORP, SSA_{PSD} was replaced with N_{PSD} to represent the SCM particle size. The resulting model is presented in Eq. (2-5), with summary and coefficients (i.e., $\beta_1 .. \beta_{10}$) of the significant variables given in Table 2.9.

$$A^1_{thix} = \beta_1 N_{PSD} + \beta_2 (W/C) + \beta_3 R + \beta_4 SCM_R + \beta_5 C_R + \beta_6 (W/C)^2 + \beta_7 N_{PSD} (W/C) + \beta_8 N_{PSD} C_R + \beta_9 (W/C) R + \beta_{10} SCM_R C_R \quad (2\text{-}5)$$

Table 2.9: Second proposed SOPR model summary and coefficients results

	Coefficient	Standardized Coefficient	Standard error	T-statistic	P-value	95% C.I (±)
β_1	+ 4.61×10^{-1}	+ 19.2	5.92×10^{-2}	+ 7.78	0.000	1.25×10^{-1}
β_2	- 1.74×10^{1}	- 19.6	3.54×10^{0}	- 4.92	0.000	7.47×10^{0}
β_3	- 1.32×10^{-1}	- 3.31	3.48×10^{-2}	- 3.79	0.001	7.36×10^{-2}
β_4	- 2.08×10^{-1}	- 2.27	6.00×10^{-2}	- 3.47	0.003	1.27×10^{-1}
β_5	+ 3.71×10^{-2}	+ 8.42	9.68×10^{-3}	+ 3.79	0.001	2.04×10^{-2}
β_6	+ 6.91×10^{0}	+ 11.1	1.23×10^{0}	+ 5.59	0.000	2.60×10^{0}
β_7	- 1.59×10^{-1}	- 9.25	1.62×10^{-2}	- 9.80	0.000	3.42×10^{-2}
β_8	- 7.19×10^{-4}	- 8.53	2.03×10^{-4}	- 3.54	0.003	4.29×10^{-4}
β_9	+ 8.91×10^{-2}	+ 3.13	2.49×10^{-2}	+ 3.58	0.002	5.25×10^{-2}
β_{10}	+ 6.80×10^{-4}	+ 2.12	2.10×10^{-4}	+ 3.23	0.005	4.44×10^{-4}

Comparisons between the experimental measurements and the results predicted with the second SOPR model are shown in Figure 2.8. In this case, the SOPR model was able to achieve better predictions of the Series II A^1_{thix} than the first SOPR model, explaining 77% of the variability in these results. Therefore, it is concluded that N_{PSD} is a better predictor for the observed variability in A^1_{thix} than SSA_{PSD}.

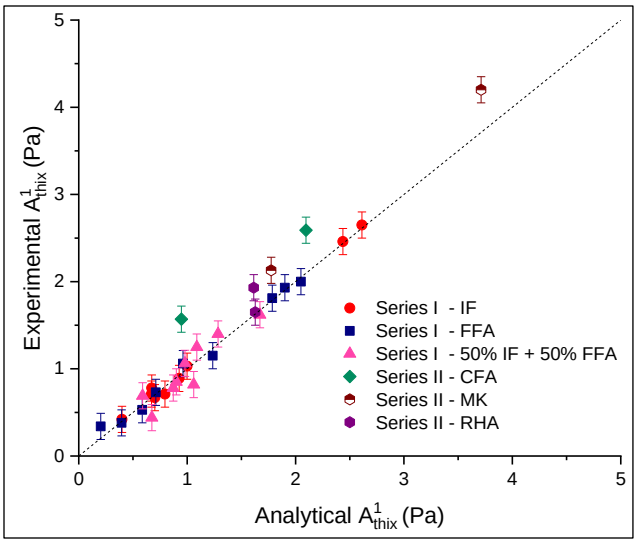

Figure 2.8: Relationship between experimental A^1_{thix} and analytical A^1_{thix} determined with the second SOPR model. R^2 of the Series II attained 0.77 using Equation (2-5).

The negative value for β_4 in the SOPR model implies a decrease in A^1_{thix} with an increase in SCM_R which is counterintuitive. In addition, Figure 2.9 shows that the replacement of FFA using an IF with the same N_{PSD} produces an increase in A^1_{thix}. Therefore, the physicochemical effect of the SCM on A^1_{thix} is not fully explained by its SCM_R.

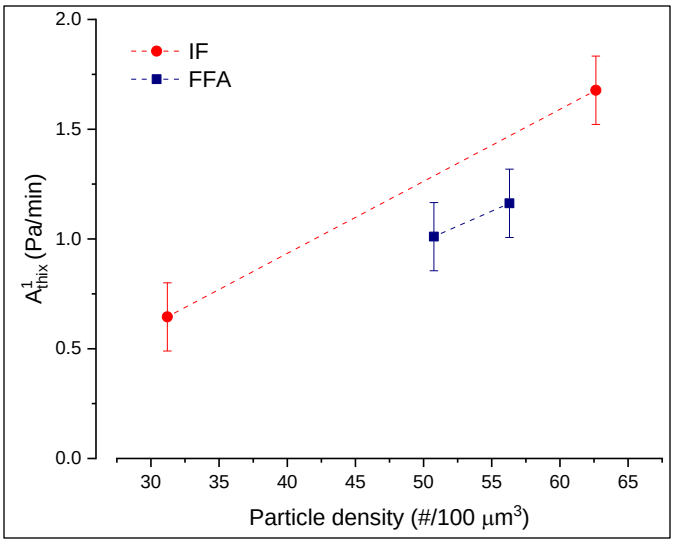

Figure 2.9: Comparison between experimental A^1_{thix} obtained with IF and FFA replacements. Each point represents the average of the A^1_{thix} of the mixtures produced with the corresponding N_{PSD} and type of SCM (i.e., IF or FFA).

In previous studies of colloidal suspensions, it has been stablished that particles with lower surface potential attract less ions, reducing the electrostatic repulsion energy. This produces particle flocculation and, therefore, higher τ_0^S (Larson 1999). However, in the case of cementitious pastes, the particles hydrate in time and this process is affected by the ions diluted in the pore solution. One of the main ions of the pore solution is Ca^{+2} (Lowke and Gehlen 2017). Thus, it is expected that particles with higher surface potential attract larger amounts of Ca^{+2}, which increases the concentration of this ion in the pseudo-contact points (i.e., zone where the C-S-H bridges are formed). In addition, Chen et al. (Chen et al. 2004) showed that slight increases of the Ca^{+2} concentration in the pore solution produces considerable increases in the cement hydration. Therefore, it can be

predicted that cementitious pastes produced using SCM with higher surface potential present higher A^1_{thix} values.

The IF presents a higher zeta potential (ζ), which is as an estimator of the surface potential, than the FFA (see Table 2.5). This difference can explain the results in Figure 2.9. Therefore, in the development of the third SOPR model, ζ was used instead of SCM_R to explain the physicochemical effect of SCM in A^1_{thix}. This model is as follows:

$$A^1_{thix} = \gamma_1 N_{PSD} + \gamma_2 (W/C) + \gamma_3 \zeta + \gamma_4 C_r + \gamma_5 (W/C)^2 + \gamma_6 R^2 + \gamma_7 N_{PSD} (W/C) + \gamma_8 N_{PSD} C_r + \gamma_9 (W/C) R + \gamma_{10} \zeta C_r \quad (6)$$

Table 2.10: Third proposed SOPR model summary and coefficient results.

	Coefficient	Standardized Coefficient	Standard error	T-statistic	P-value	95% C.I (±)
γ_1	+ 4.07×10^{-1}	+ 17.1	7.95×10^{-2}	+ 5.12	0.000	1.68×10^{-1}
γ_2	- 3.78×10^{1}	- 43.1	8.02×10^{0}	- 4.71	0.000	1.69×10^{1}
γ_3	+ 2.70×10^{-1}	+ 9.96	8.06×10^{-2}	+ 3.35	0.004	1.70×10^{-1}
γ_4	+ 7.66×10^{-2}	+ 17.8	1.20×10^{-2}	+ 3.86	0.001	4.18×10^{-2}
γ_5	+ 1.41×10^{1}	+ 22.9	2.73×10^{0}	+ 5.19	0.000	5.76×10^{0}
γ_6	- 2.16×10^{-3}	- 1.90	6.15×10^{-4}	- 3.51	0.003	1.30×10^{-3}
γ_7	- 1.51×10^{-1}	- 8.86	2.29×10^{-2}	- 6.58	0.000	4.82×10^{-2}
γ_8	- 5.68×10^{-4}	- 6.80	2.66×10^{-4}	- 2.14	0.048	5.61×10^{-4}
γ_9	+ 8.55×10^{-2}	+ 3.03	2.64×10^{-2}	+ 3.24	0.005	5.57×10^{-2}
γ_{10}	- 8.73×10^{-4}	- 9.20	2.83×10^{-4}	- 3.09	0.007	5.96×10^{-4}

The fact that γ_1 and γ_3 are positive means that the use of SCMs with higher N_{PSD} and higher ζ produces cementitious pastes with higher A^1_{thix}.

The coefficients (i.e., $\gamma_1 \ldots \gamma_{10}$) for Eq. (2-6) are shown in Table 2.10. Comparisons between the experimental measurements and the results predicted with the third SOPR model are shown in Figure 2.10. This model can explain 98% of the variability in A^1_{thix} for the series II mixtures, which is significantly better than the second SOPR model. Comparing the results of both models, it can be stated that ζ is more significant than SCM_R in the explanation of the A^1_{thix} results.

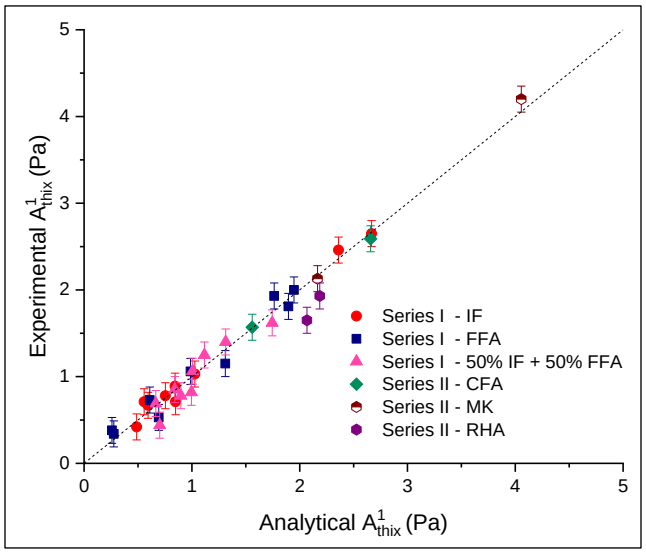

Figure 2.10: Relationship between experimental A^1_{thix} and analytical A^1_{thix} determined with the third SOPR model. R^2 of the Series II attained 0.98 using Equation (2-6).

The fact that γ_2 is negative and γ_5 is positive means that an increase in w/c produces a reduction in A^1_{thix}, and that this effect is more significant for lower w/c values, as shown in Figure 2.11. In addition, the fact that γ_7 is negative indicates that the A^1_{thix} of cementitious pastes produced with a larger w/c is less affected by the N_{PSD} of the SCM. Moreover, the positive sign of γ_9 contrasts the negative effect in A^1_{thix} of a higher SCM replacement (i.e., negative γ_6), which means that cementitious pastes with larger w/c are less affected by the type of particles used (i.e., SCM or cement). These results can be expected because larger w/c increases the distance between the particles and, therefore, reduces their interactions.

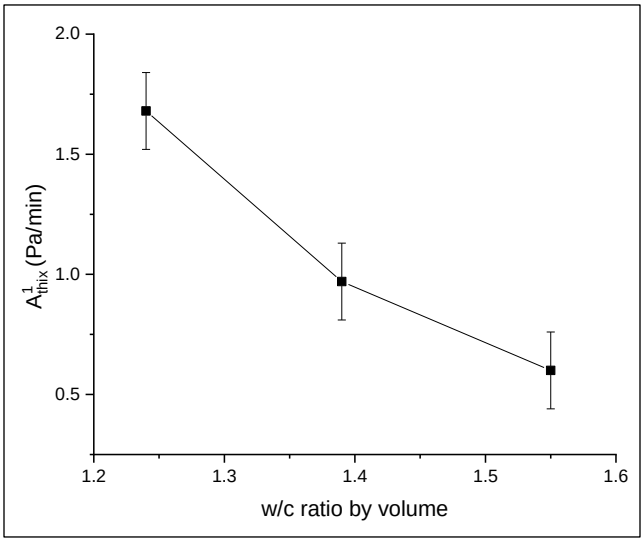

Figure 2.11: Effect of w/c on A^1_{thix}. Each point represents the average A^1_{thix} of the Series I mixtures produced with each w/c.

The interaction between w/c and R (i.e., γ_9) has a positive effect on A_{thix}^1. In contrast, the square of R (i.e., γ_6) has a negative effect on A_{thix}^1. The interaction between these two effects means that an increase in R increases A_{thix}^1 until a threshold amount of replacement, which, according to the SOPR model, is near 30%. Further increases of R produce reductions in A_{thix}^1. The replacement of cement by SCM produces a dilution of the cement particles, increasing w/c, and improving its hydration (De la Varga et al. 2018). In addition, the SCM provides new nucleation sites, which increase the number of C-S-H bridges. As a result of these effects, the replacement of SCM by cement increases A_{thix}^1. However, C-S-H bridges are not produced between the SCM particles. Thus, beyond a certain threshold (i.e., R larger than 30%), further increases in SCM replacement reduce the pseudo-contact points between the cement particles or between the cement and the SCM particles, which reduces A_{thix}^1.

The fact that γ_4 is positive implies that cements with higher reactivity during the dormant period (i.e., higher C_R) produce cementitious pastes with higher A_{thix}^1. In contrast, γ_8 and γ_{10} are negative, which means that the A_{thix}^1 of mixtures produced with cements with higher reactivity is less affected by the N_{PSD} or ζ of the SCM.

A_{thix}^1 values estimated with the SOPR model for different combinations of SCM properties (i.e., zeta potential and particle density) are analyzed. Specifically, Figure 2.12.a shows the results for w/c and R of 1.55 and 40%, respectively, while Figure 2.12.b shows

the results for w/c and R of 1.24 and 20%, respectively. In both cases, C_r was taken equal to 300 μW/g. The results suggest that the effect of SCM properties is more significant for lower w/c and R. In addition, the effect of zeta potential relative to the effect of particle density on A^1_{thix} is more significant for higher w/c and R.

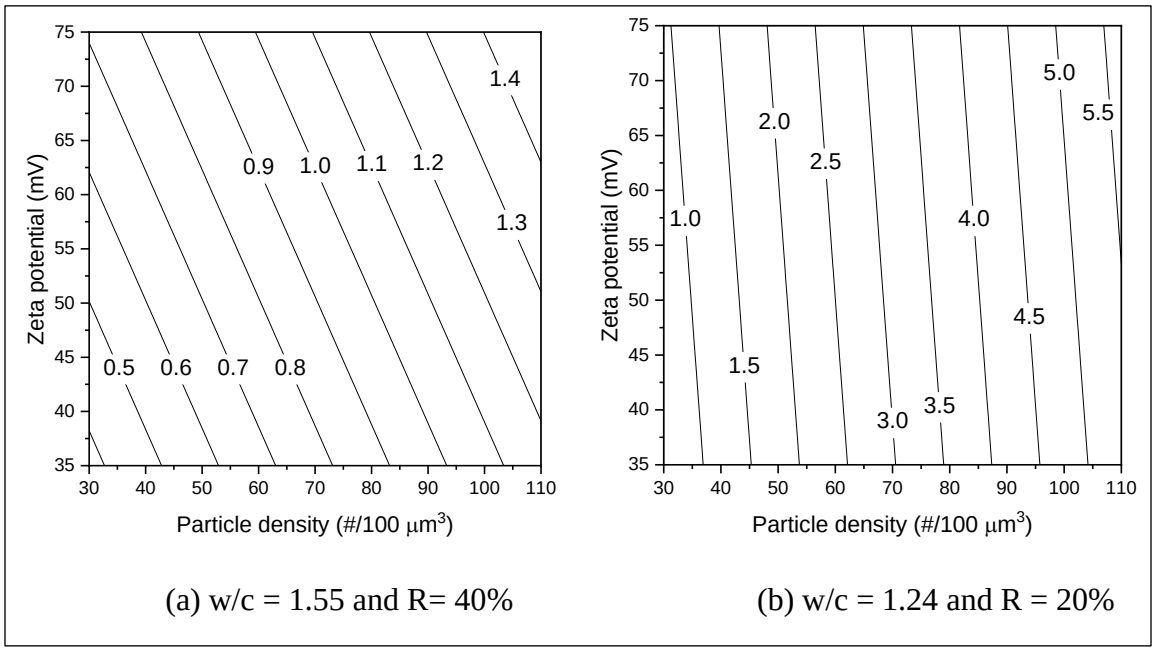

(a) w/c = 1.55 and R= 40% (b) w/c = 1.24 and R = 20%

Figure 2.12: Effect of SCM properties on A^1_{thix}, estimated with the SOPR model, for two different w/c and R combinations. In both cases, C_r was taken equal to 300 μW/g.

A^1_{thix} values estimated with the SOPR model for different combinations of mixture design parameters (i.e., SCM replacement and w/c) are analyzed next. Specifically, Figure 2.13.a shows the results for IF-Fi, while Figure 2.13.b shows the results for FFA-Co. In both cases, C_r is taken equal to 300 μW/g. The results suggest that the effects of mixture

design parameters are more relevant when IF-Fi, with a higher zeta potential and particle density, is used. In addition, there is an amount of SCM replacement that maximizes A_{thix}^{1} for each w/c, and this amount of replacement increases as w/c increases.

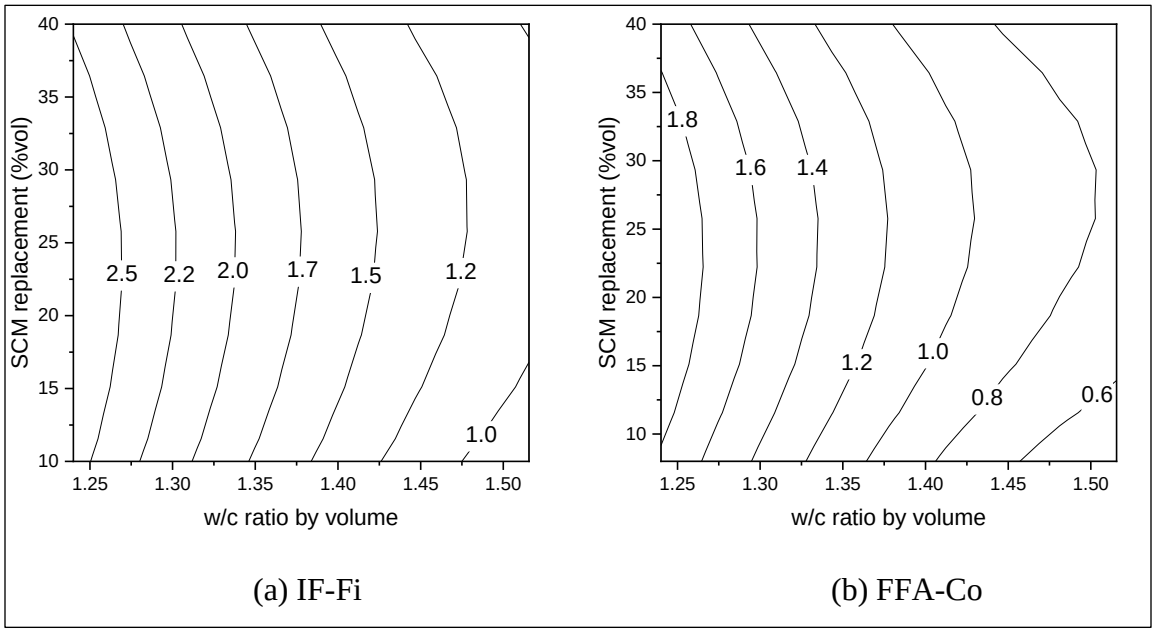

Figure 2.13: Effect of mixture design parameters on A_{thix}^{1}, estimated with the SOPR model, for different SCMs. In both cases, C_r was taken equal to 300 μW/g.

The standardized coefficients in Table 2.10 indicate the number of standard deviations the dependent variable (i.e., A_{thix}^{1}) will change per standard deviation increase in the independent variables (Verdugo et al. 2005). Therefore, the standardized coefficients can be used to assess the relative effect of the independent variables on the dependent

variable when the variables are measured in different units. Table 2.10 shows that the w/c has the largest effect on A_{thix}^{1}. In contrast, changes of the SCM replacement in the range of 20 to 40% have lower effect on A_{thix}^{1}. Among the properties of the SCM, N_{PSD} has a greater effect than ζ on A_{thix}^{1}. In addition, cement reactivity has a similar effect as the N_{PSD} of the SCM on A_{thix}^{1}.

2.4.3 Nucleation and growth rate assessment

The heat flow measurements from the first 12 h of the Series I FFD mixtures are presented in Figure 2.14. The BNG model [see Eq. (2-3)] together with the data between the minimum in the induction period and the end of the acceleration period were used to determine the best fitting A, K_N, and K_G values for each mixture. K_N describes the rate with which the surfaces of the cement particles in a unit volume of paste are covered with hydration products, while K_G indicates the rate with which the pore spaces between the particles in a unit volume of paste are filled (Mostafa and Yahia 2017).

The values of K_N and K_G for each mixture are shown in Table 2.11. In order to evaluate the effect of the SCM properties and the mixture design, the values of K_N and K_G were normalized with respect to their average values.

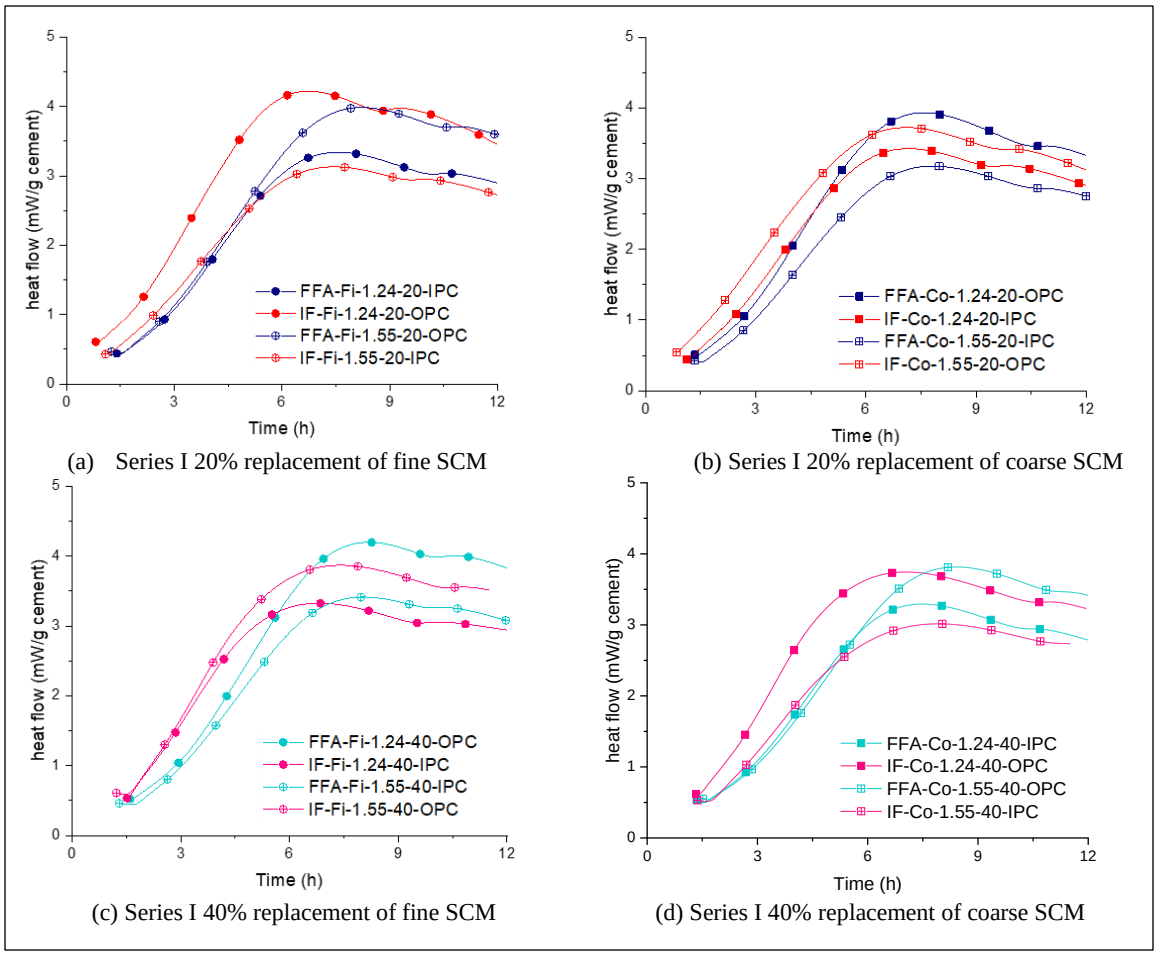

(a) Series I 20% replacement of fine SCM

(b) Series I 20% replacement of coarse SCM

(c) Series I 40% replacement of fine SCM

(d) Series I 40% replacement of coarse SCM

Figure 2.14: Heat flow during the first 12 hours of the Series I FFD mixtures.

Table 2.11: K_N and K_G values of the series I FFD mixtures.

	Mix code	K_N $x10^{-3}$ (h^{-3})	Normalized K_N	K_G $x10^{-1}$ (h^{-1})	Normalized K_G
series I	IF- Fi -1.24-20-OPC	3.20	1.22	1.95	1.12
	IF-Co-1.24-20-IPC	2.84	1.08	1.88	1.08
	IF- Fi -1.55-20-IPC	2.97	1.13	1.90	1.09
	IF-Co-1.55-20-OPC	3.49	1.33	2.11	1.21
	IF- Fi -1.24-40-IPC	3.15	1.20	2.05	1.18
	IF-Co-1.24-40-OPC	2.89	1.10	2.02	1.16
	IF- Fi -1.55-40-OPC	3.04	1.16	1.97	1.13
	IF-Co-1.55-40-IPC	2.54	0.97	1.85	1.06
	FFA- Fi -1.24-20-IPC	2.09	0.80	1.66	0.95
	FFA-Co-1.24-20-OPC	2.18	0.83	1.63	0.93
	FFA- Fi -1.55-20-OPC	2.43	0.93	1.48	0.85
	FFA-Co-1.55-20-IPC	2.43	0.93	1.63	0.93
	FFA- Fi -1.24-40-OPC	2.05	0.78	1.37	0.78
	FFA-Co-1.24-40-IPC	2.29	0.87	1.64	0.94
	FFA- Fi -1.55-40-IPC	1.96	0.75	1.42	0.81
	FFA-Co-1.55-40-OPC	2.41	0.92	1.40	0.80

The average normalized K_N and K_G for the low and high levels of each experimental factor are presented in Figure 2.15. The grey area in this figure represents changes of K_N and K_G within $\pm 2.5\%$, which are considered non-significant effects.

As can be seen in Figure 2.15, the change of w/c and particle size from low to high level resulted in almost no effect on the rate of cement hydration and the rate of growth of C-S-H bridges. Therefore, it can be concluded that the effects of these factors in A^1_{thix} is related with the number of contact points between the particles.

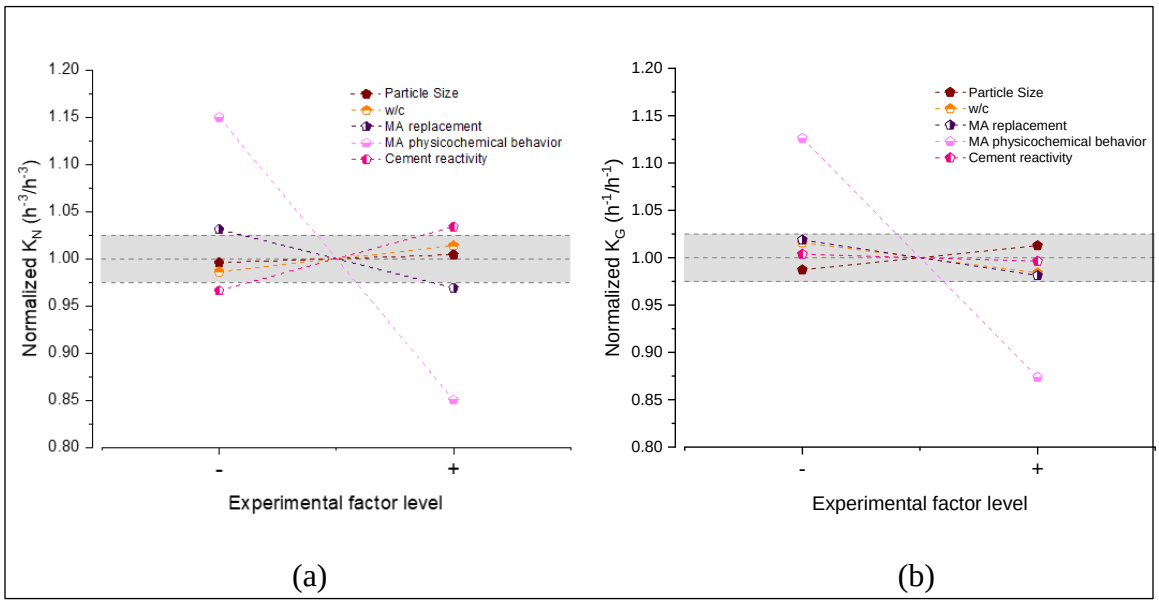

Figure 2.15: Average normalized K_N (a) and K_G (b) for low (-) and high (+) levels of each experimental factor.

The increase of SCM replacement from 20% to 40% resulted in decreased nucleation rate of the cement (i.e., K_N) and non-significant variations in the growth rate (i.e., K_G). This finding suggests that the growth rate of C-S-H bridges is not affected by the amount of cement replaced by SCM, and a 20% replacement promotes better hydration of the cement particles than a 40% replacement.

Figure 2.15 shows that major changes in both K_N and K_G are related with the type of SCM used. The fact that the mixtures produced with IF present higher K_N and K_G than the mixtures produced with FFA supports the hypothesis that the physicochemical effect of the SCMs is governed by their surface potential rather than their chemical reactivity at early ages.

Specifically, SCMs with higher surface potential (i.e., IF) produce less flocculation of the cement particles than SCMs with lower surface potential (i.e., FFA), as represented in Figure 2.16. Thus, the cement particles in mixtures produced with IF present higher amounts of surface exposed to water, which improves the rate at which they are covered by hydration products (i.e., higher K_N).

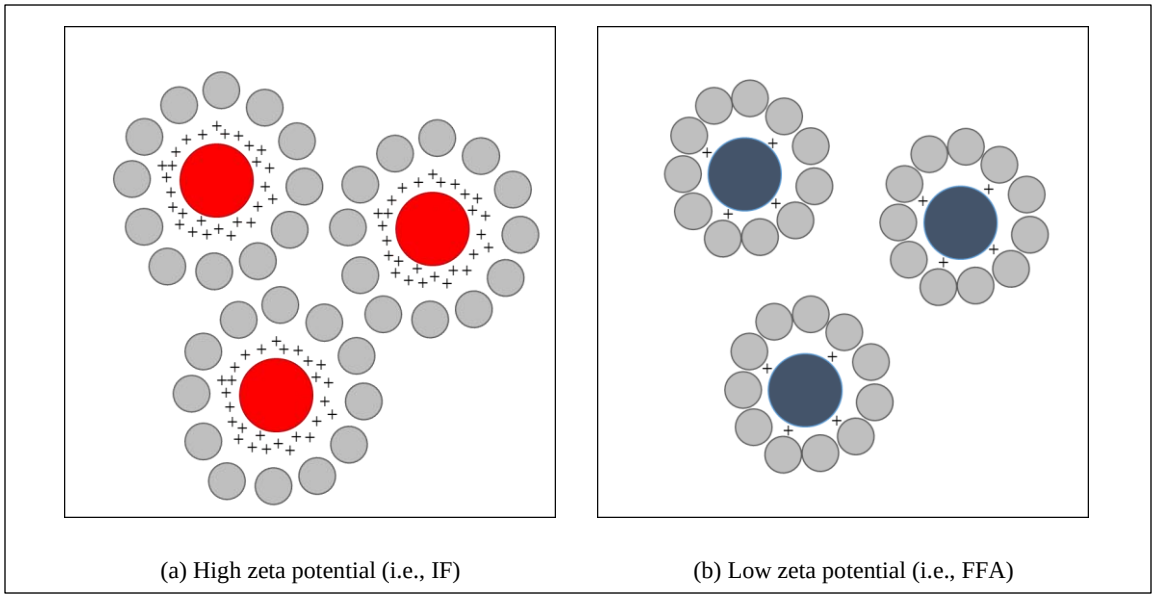

(a) High zeta potential (i.e., IF) (b) Low zeta potential (i.e., FFA)

Figure 2.16: Comparison of SCMs with low (i.e., blue dots) and high (i.e., red dots) surface potential. Calcium ions are represented by + sign and cement particles by grey dots.

In addition, the mixtures produced with IF presented higher growth rate of the C-S-H bridges (i.e., higher K_G). This result supports the conclusion obtained with the SORP model that SCMs with higher surface potential enhance the hydration of cement particles

at the pseudo-contact points, due to a higher presence of Ca^{+2} ions (represented in Figure 2-16), which increases A_{thix}^{1}.

As expected, the use of a more reactive cement (i.e., OPC) instead of a less reactive cement (i.e., IPC) resulted in larger K_N. However, the use of a more reactive cement does not have a significant effect on K_G.

2.5 Conclusions

This study investigated the effects of particle size and physicochemical properties of supplementary cementitious materials (SCMs) and their interactions with primary mixture parameters on the structural build up of cementitious paste. Five different SCMs were used in the study: two of them were used to develop the model and the other three to validate it. The study focused on SCMs with similar particle size distribution to cement and in the earlier structural build up of cementitious pastes (below 60 minutes after water addition). Based on the results, the main conclusions are as follows:

1. A second order polynomial regression model to predict the structural build up of cementitious paste as a function of SCM properties and primary mixture parameters was developed and validated. The model shows good accuracy to predict the structural build up of mixtures prepared with various SCMs, SCM replacement amounts, water to cement ratios, and cement with different reactivities.

2. The effect of particle size of SCM on the structural build up of cementitious paste is governed by the particle density which determines the number of contact points instead of the specific surface area.
3. The effect of physicochemical properties of SCM on the structural build up of cementitious paste is governed by the surface potential instead of the chemical reactivity at early age.
4. The structural build up of cementitious paste is affected mostly by the water to cementitious ratio. In contrast, the replacement level of SCM is the least significant parameter affecting structural build up. Among the SCM properties, the particle density has a greater effect than the surface potential. In addition, reactivity of cement has a similar effect as the particle density of SCM.
5. The structural build up of mixtures with more reactive cement is less affected by the SCM properties. In addition, the structural build up of mixtures with a higher water to cement ratio is less affected by the particle density of SCM and by the level of replacement of SCM.
6. Changes in the particle density of SCM and water to cement ratio result in slight variations in the nucleation and growth rates of the cement particles. This means that the effects of these parameters on the structural build up of cementitious paste are produced by a reduction in the distance between the particles rather than improved cement hydration.

CHAPTER 3:
EFFECT OF SUPPLEMENTARY CEMENTITIOUS MATERIALS ON VISCOSITY OF CEMENT-BASED PASTES

The aim of this chapter is to analyze the effect of particle size and type of supplementary cementitious materials (SCMs) and their interactions with the main mixture parameters on the viscosity of cementitious paste, addressing the second specific objective of this research. To this end, a fractional face centered central composite experimental design, composed by 29 mixtures with two SCMs, was used to develop second order polynomial regression (SOPR) models. These models were then validated using the results from 6 additional mixtures with three different SCMs. The equilibrium flow curve was used to quantify the viscosity of each mixture.

This chapter includes a detailed characterization of the SCM properties and an assessment of the effect of those properties on the viscosity of cementitious paste at different shear rate ranges. In addition, an analysis of the dynamic yield stress is performed to estimate the bonding strength between cementitious particles. The results show that the effect of particle size on viscosity is better explained by the particle number density than

by the specific surface area of the cementitious particles. In addition, the viscosity of cementitious paste can be raised by increasing the number of contact points and/or the bonding strength between the particles.

3.1 Introduction

The use of supplementary cementitious materials (SCMs), also known as mineral admixtures (e.g., fly ash, blast furnace slag), in the cement industry has increased significantly over the last three decades. In 1995, only 44% of the cements produced in the United States were blended cements. By 2009, this figure had increased to over 80% (Schneider et al. 2011).

Most of the previous research on SCMs has focused on the effects of these materials on the mechanical properties and durability of concrete. Many studies have found that most SCMs increase the concrete strength at later ages (Bendapudi and Saha 2011; Dhanya et al. 2018). In addition, SCMs reduce the permeability of concrete and, therefore, improve its durability (He and Shi 2008; Juenger and Siddique 2015; Mo et al. 2017; Narasimha Reddy and Kavyateja 2020). On the other hand, fewer studies have focused on the effects of SCMs on concrete workability.

The workability of fresh concrete controls how well the material can be mixed, placed, consolidated, finished and, therefore, the quality of the built element. Poor

workability of fresh concrete may have a detrimental effect on the mechanical properties and durability of the structure. Previous researchers (Ferraris et al. 2001a; Rubio-Hernández 2018) have found that the rheological behavior of the cementitious paste is one of the most important factors that govern the workability of a concrete mixture.

Fresh cement-based materials (CBMs) behave as yield stress fluids (Tattersall and Banfill 1983). This means that the material flow is initiated when the applied stress exceeds a critical shear stress value, called the yield stress (τ_0) (Feys et al. 2017). Once the material begins to flow, the viscosity (μ_p) dominates its behavior (Choi et al. 2019). The most common method to measure the rheology of CBMs is the equilibrium flow curve, plotted as the equilibrium shear stress (τ) versus the shear rate ($\dot{\gamma}$) (Qian and Kawashima 2018). Roussel *et al.* (Roussel 2006) showed that the yield stress of fresh CBMs increases significantly in the first hour after mixing. In contrast, the viscosity of fresh CBMs remains almost constant in the same period of time.

Although many constitutive equations have been proposed in the literature to characterize the rheological behavior of CBMs, three models have received the most attention (Feys and Asghari 2019; Mahmoodzadeh and Chidiac 2013; Qian and Kawashima 2018). These models are the Bingham model (Bingham 1922), the Herschel – Bulkley model (de Larrard et al. 1998), and the modified Bingham model (Yahia and Khayat 2001), which are presented in Eq. (3-1), (3-2), and (3-3), respectively.

$$\tau = \tau_0 + \mu_p \dot{\gamma} \quad (3\text{-}1)$$

$$\tau = \tau_0 + k\dot{\gamma}^n \quad (3\text{-}2)$$

$$\tau = \tau_0 + \mu\dot{\gamma} + c\dot{\gamma}^2 \quad (3\text{-}3)$$

In the case of Bingham model, the rheological behavior is described as a linear function given by two parameters: the yield stress, τ_0 and viscosity, μ_p. However, several authors (Choi et al. 2019; Ouyang et al. 2018; Wallevik et al. 2015) have reported non-linear rheological behavior of CBMs. In these cases, the viscosity depends on the applied $\dot{\gamma}$ and the use of the Bingham model may lead to inaccurate results, requiring the incorporation of an additional parameter. This parameter can be a power function (i.e., n) for the $\dot{\gamma}$ term, leading to the Herschel – Bulkley model [Eq. (3-2)], or a second order term in $\dot{\gamma}$ (i.e., c), creating the modified Bingham model [Eq. 3-3)]. In the case of shear – thickening behavior, n is larger than 1, while c is larger than 0. In contrast, for shear – thinning behavior, n is smaller than 1, while c is smaller than 0.

Many studies (Ferraris 1999; Matos et al. 2018; Park et al. 2005; Qian and Kawashima 2018) have focused on the yield stress and its relation with the measurements from common field tests, such as the slump flow (Bouvet et al. 2010b; Lu et al. 2015). In contrast, few studies have investigated the viscosity of CBMs, with most of the available studies being for self – consolidating concrete (SCC) (Megid and Khayat 2017; Shen et al. 2009, 2014) and shotcrete (Secrieru et al. 2020; Yun et al. 2015). In recent years, new

construction technologies that require better rheological control (Buswell et al. 2018; García-Alvarado et al. 2020; Navarrete et al. 2017b), such as 3D-printed concrete, have led to increased attention to plastic viscosity, which is one of the main parameters that control the constructability and quality of concrete structures.

Specifically, the homogeneity of concrete during transportation (Esmaeilkhanian et al. 2014; Kim et al. 2020) and consolidation (Navarrete and Lopez 2016; Petrou et al. 2000; Tattersall and Baker 1988) is highly influenced by its viscosity, which is more relevant in the case of lightweight as well as heavyweight aggregate concretes (Navarrete and Lopez 2017; Solak et al. 2018). For pumpable concrete technologies, such as SCC, shotcrete and 3D-printed concrete, one of the main parameters that govern the ease of pumping is viscosity (Secrieru et al. 2020; Sonebi and Amziane 2017; Yun et al. 2015). It is also important to control viscosity in order to assure adequate extrudability (Chen et al. 2019) in 3D printing concrete, passing ability in SCC (Matos et al. 2018), and shootability (Shen et al. 2019) in shotcrete.

Previous authors (Chong et al. 2018; Krieger and Dougherty 1959; Liu 2000; Maron and Pierce 1956) have proposed different models to predict the viscosity of colloidal suspensions, such as CBMs, based on the viscosity of the continuous phase (i.e., water), solid volume fraction (ϕ_T), maximum packing density (ϕ_m), and intrinsic viscosity. Struble and Sun (Struble and Sun 1995) found that the Krieger – Dougherty model accurately predicts the viscosity of cement pastes and that an increase in ϕ_T results in

increased viscosity. On the other hand, Bentz *et al.* (Bentz et al. 2012) showed that the Krieger – Dougherty model and other Bingham viscosity models tend to underestimate the viscosity of blended cement pastes. A possible explanation of this discrepancy could be the differences in the interparticle forces between cements and SCMs (Flatt and Bowen 2006; Zhu et al. 2020).

A number of studies (Adjoudj et al. 2014; Bentz et al. 2012; Felekoğlu et al. 2006; Grzeszczyk and Lipowski 1997; Jalal et al. 2013; Jiao et al. 2017; Laskar and Talukdar 2008; Park et al. 2005; Saleh Ahari et al. 2015; Vance et al. 2013) have also shown that SCMs considerably affect the viscosity of CBMs. However, contradictory results have been found between different studies on this topic. For example, some researchers (Felekoğlu et al. 2006) have found that the use of fly ash increases the viscosity of CBMs, while others (Bentz et al. 2012) have found the opposite. These differences have been attributed to differences in the geometry and surface roughness of the particles (Jalal et al. 2013).

Previous researchers have found that the particle size distribution (PSD) of SCMs affect the viscosity of cementitious pastes (Bentz et al. 2012; Grzeszczyk and Lipowski 1997; Lee et al. 2003; Vance et al. 2013). Lee et al. (Lee et al. 2003) found that the viscosity of cementitious pastes decreases for wider PSD. In addition, it has been found that the use of finer blended cement increases the viscosity (Bentz et al. 2012; Grzeszczyk and Lipowski 1997; Vance et al. 2013). However, it is not yet clear whether this effect is

produced by the larger specific surface area or by the larger particle number density of finer blended cement.

It has been shown (Ohshima and Makino 2014) that the particles of colloidal suspensions flocculate and form three dimensional networks. The development of larger interparticle forces in these networks results in higher viscosity of colloidal suspensions (i.e., cementitious pastes) (Franks et al. 2000; Lionberger 2002). In addition, the use of different SCMs and cements produces considerable differences in the interparticle force of cementitious pastes (Flatt and Bowen 2007; Lowke and Gehlen 2017; Zhu et al. 2020). Despite these findings, to the best of the authors' knowledge, relationships for the particle size and interparticle force with the viscosity of cementitious paste have not been investigated.

3.2 Research significance

In line with the research gap recognized above, this chapter discusses the effects of the particle size and type of SCMs and their interactions with the primary mixture parameters (i.e., solid volume fraction, SCM replacement, and cement type) on the viscosity of cementitious paste. Ultimately, this research can lead to better use of SCMs for the control of viscosity in CBM for applications such as SCC, shotcrete and 3D – printed concrete.

3.3 Materials and methods

3.3.1 Experimental design

The effects of SCM particle size and type and their interactions with the primary mixture design parameters on the viscosity of cementitious paste were experimentally measured using a fractional face centered central composite design (FFCCCD), similar to the experimental procedure followed in a previous study by the authors (Navarrete et al. 2020). This design consists of an embedded fractional factorial design (FFD) with center points (CP) and axial points (AP). The FFCCCD permits the measured response to be modeled by a second order polynomial regression (SOPR) equation, which allows the main, quadratic, and interactive effects of the experimental parameters on the property under study to be quantified (Montgomery and Runger 2014).

The five experimental parameters that were studied are: (1) SCM particle size (PS); (2) ϕ_T; (3) SCM replacement (R); (4) SCM type (SCM_t); and (5) cement type (C_t). Table 3.1 shows the three levels of each experimental parameter. As presented in Table 3.2, a 2^{5-1} FFD with 3 CP and 2*5 AP was used, resulting in 29 experimental runs (i.e., Series I). Six additional runs (i.e., Series II) were also developed to validate the SOPR models developed with the Series I mixtures.

Table 3.1: Experimental factors and levels.

	Levels		
Experimental Factors	-	0	+
SCM particle size, PS	100% Fine	50% Fine + 50% Coarse	100% Coarse
Solid volume fraction, ϕ_T	0.39	0.42	0.45
SCM replacement, R (%vol)	20	30	40
SCM type, SCM_t	100% IF	50% IF + 50% FFA	100% FFA
Cement type, C_t	100% IPC	50%IPC + 50%OPC	100% OPC

The Series I mixtures were made using Class F fly ash (FFA) and inert filler (quartz) (IF). The use of these SCMs permitted decoupling the effects from the SCM particle size and type. To assess the particle size effect, parts of the FFA and IF were ball-milled for 48 h and 7 d, respectively, at 75 RPM to obtain finer materials. The non-milled FFA was defined as coarse FFA (FFA-Co), while the milled FFA was defined as fine FFA (FFA-Fi). Coarse IF (IF-Co) and fine IF (IF-Fi) with the same specific surface area (SSA) as FFA-Co and FFA-Fi, respectively, were obtained by mixing different proportions of the non-milled and milled IF. In addition, two cements with similar PSD and different chemical composition were used to characterize the effect of the cement type on the viscosity.

Rice husk ash (RHA), metakaolin (MK), and Class C fly ash (CFA) were used to produce the Series II mixtures. These SCMs were chosen because, like the FFA and IF, their PSDs are in the same range as that of cement. The effects from finer SCMs, such as silica fume or nanomaterials, on viscosity are out of the scope of this research.

The ϕ_T of the Series I and Series II mixtures ranged between 0.39 and 0.45, which is equivalent to a water-to-cementitious (w/c) ratio by volume between 1.24 and 1.55 and by mass between 0.40 and 0.50. In addition, between 8 and 40% of the cement volume was replaced by SCMs, which is equivalent to mass replacements between 6 and 37%. Previous authors (Chong et al. 2018; Krieger and Dougherty 1959; Liu 2000; Maron and Pierce 1956) have shown that the ϕ_T/ϕ_M ratio is one of the most important parameters that govern the viscosity of colloidal suspensions. A recent study by Mehdipour and Khayat (Mehdipour and Khayat 2017) has shown very small variability (less than 4%) in ϕ_M among cementitious pastes with similar characteristics (i.e., particle size, ϕ_T, R, and cement and SCMs types) as the Series I and Series II mixtures. Therefore, it was assumed that ϕ_M was the same for all the Series I and Series II mixtures.

Analysis of variance (ANOVA) and backward elimination algorithm (Montgomery and Runger 2014) were realized with the 29 experimental runs of Series I to assess the significant parameters on viscosity and develop SOPR models. Then, model prediction residuals for the Series II results were used to validate the SOPR models based on the predicted residual error of squares (PRESS) statistic (Allen 1971).

Table 3.2: Series I mixes and factorial levels.

Row	Mix code	PS	ϕ_T	R	SCM_t	C_t= -(PS)(ϕ_T)R(SCM_t)
1	IF- Fi -1.24-20-OPC	-	+	-	-	+
2	IF-Co-1.24-20-IPC	+	+	-	-	-
3	IF- Fi -1.55-20-IPC	-	-	-	-	-
4	IF-Co-1.55-20-OPC	+	-	-	-	+
5	IF- Fi -1.24-40-IPC	-	+	+	-	-
6	IF-Co-1.24-40-OPC	+	+	+	-	+
7	IF- Fi -1.55-40-OPC	-	-	+	-	+
8	IF-Co-1.55-40-IPC	+	-	+	-	-
9	FFA- Fi -1.24-20-IPC	-	+	-	+	-
10	FFA-Co-1.24-20-OPC	+	+	-	+	+
11	FFA- Fi -1.55-20-OPC	-	-	-	+	-
12	FFA-Co-1.55-20-IPC	+	-	-	+	+
13	FFA- Fi -1.24-40-OPC	-	+	+	+	+
14	FFA-Co-1.24-40-IPC	+	+	+	+	-
15	FFA- Fi -1.55-40-IPC	-	-	+	+	-
16	FFA-Co-1.55-40-OPC	+	-	+	+	+
17	AP-Fi	-	0	0	0	0
18	AP-Co	+	0	0	0	0
19	AP-1.24	0	+	0	0	0
20	AP-1.55	0	-	0	0	0
21	AP-20	0	0	-	0	0
22	AP-40	0	0	+	0	0
23	AP-IF	0	0	0	-	0
24	AP-FFA	0	0	0	+	0
25	AP-IPC	0	0	0	0	-
26	AP-OPC	0	0	0	0	+
27 -29	CP	0	0	0	0	0

3.3.2 Materials characterization

Type I ordinary Portland cement (OPC) and type IP blended cement (IPC) in compliance with ASTM C150 (ASTM Standard C150/C150M 2016) and ASTM C595

(ASTM International 2019), respectively, were used. The IPC contained 80% OPC and 20% IF. Table 3.3 shows the specific gravity and oxide composition, determined by X-ray fluorescence (XRF), of the cements and SCMs.

Table 3.3: Chemical composition and specific gravity of cements and SCMs.

	Cements		Series I		Series II		
	OPC	IPC	FFA	IP	CFA	RHA	MK
CaO (%)	65.80	52.64	1.52	0.21	17.50	0.71	0.07
SiO_2 (%)	19.30	35.18	52.70	98.70	33.30	70.30	47.20
Al_2O_3 (%)	4.50	3.60	17.70	0.01	19.10	0.06	42.30
SO_3 (%)	2.31	1.84	0.46	-	7.34	-	-
Fe_2O_3 (%)	3.04	2.52	6.10	0.61	3.26	4.14	5.52
MgO (%)	1.07	0.89	1.30	0.05	0.81	-	-
Other minor oxides (%)	1.28	1.17	4.32	0.21	4.69	9.09	2.31
Loss on ignition (%)	2.70	2.16	15.90	0.21	14.00	15.70	2.60
Specific gravity	3.14	3.05	2.39	2.69	2.37	2.14	2.72

The microstructure of the SCMs were observed using a scanning electron microscope (SEM), which provided surface information of these materials. A Quanta 250 microscope with an accelerating voltage of 10kV and magnifications between 300x and 1000000x was used to take the images. Each sample was oven dried, coated with 4 nm of gold, and later mounted on a holder. SEM images for the different SCMs at a magnification of 1500x are shown in Figure 3.1.

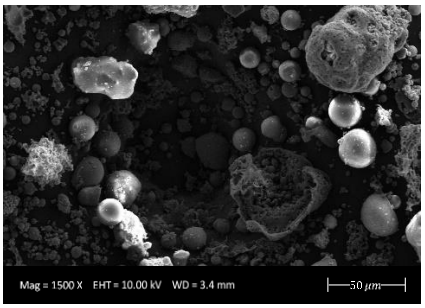

(a) FFA-Co

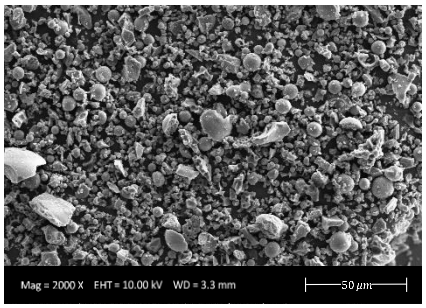

(b) FFA-Fi

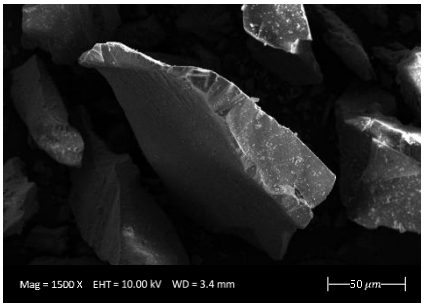

(c) non-milled IF

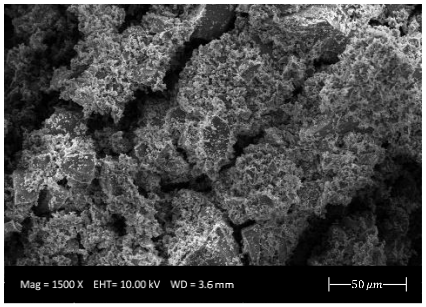

(d) 7-day milled IF

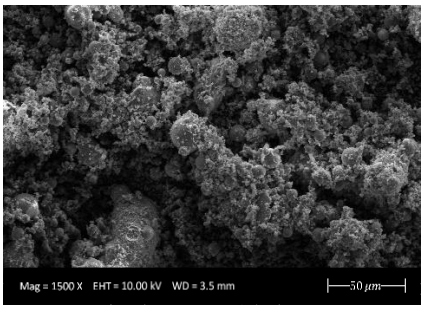

(e) CFA

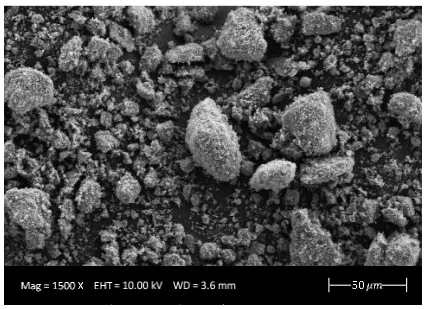

(f) MK

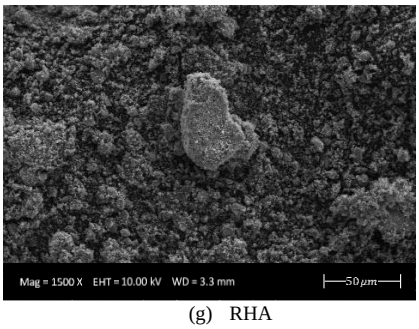

(g) RHA

Figure 3.1: 1500x SEM images of supplementary cementitious materials.

3.3.2.1 Particle size distribution

A Malvern Mastersizer 2000 laser diffractometer was used to measure the PSDs of the cements and SCMs, which are shown in Figure 3.2. The experimental procedure was described in a previous chapter by the authors (Navarrete et al. 2020). The D10, D50 and D90 parameters for each cement and SCM are presented in Table 3.4. Figure 3.2.a shows that the PSDs of both cements (i.e., OPC and IPC) were similar. Furthermore, IF-Fi and FFA-Fi were finer than OPC and IPC, while IF-Co and FFA-Co were coarser than OPC and IPC.

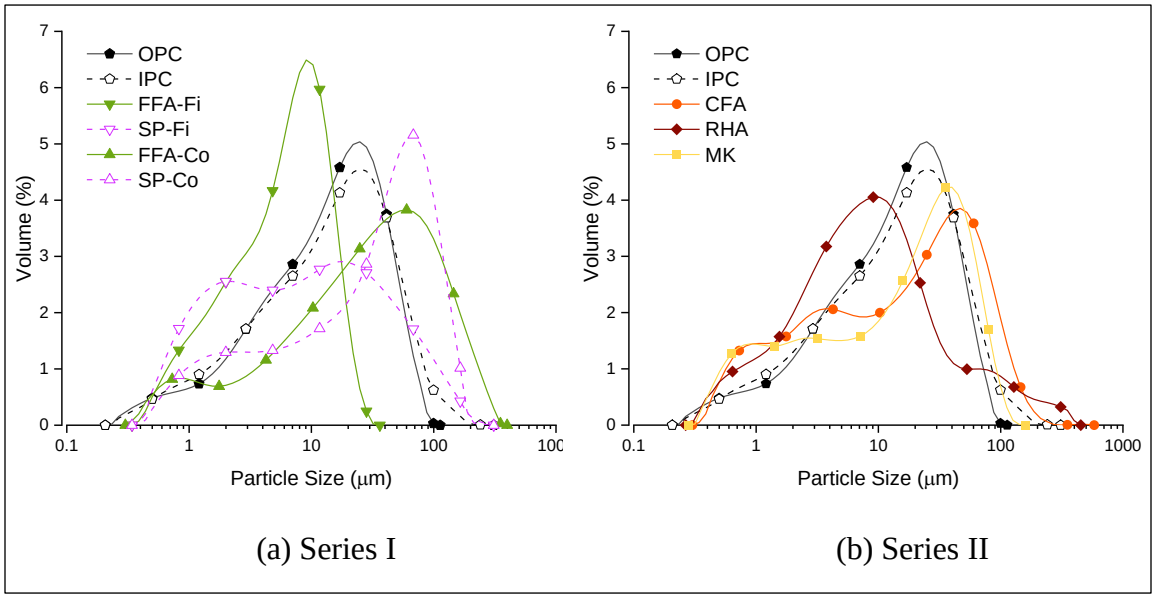

Figure 3.2: Particle size distributions of cements and SCMs.

Table 3.4: Particle size parameters of cements and SCMs.

		D10 (μm)	D50 (μm)	D90 (μm)	SSA (m^2/cm^3)		N_{PSD} (#/100 μm^3)
					BET	PSD	
Cements	OPC	1.95	13.67	40.69	12	1.30	99.96
	IPC	2.29	16.40	46.27	10	1.30	88.51
Series I	FFA-Fi	1.22	5.94	13.86	10	1.83	56.30
	IF - Fi	1.85	12.94	44.68	4	1.83	62.64
	FFA-Co	2.17	29.48	122.54	10	1.00	52.93
	IF - Co	4.67	35.65	82.34	4	1.00	31.20
Series II	CFA	5.47	41.54	95.34	8	1.56	73.45
	RHA	1.21	7.50	52.90	158	1.71	90.02
	MK	0.96	15.71	54.56	26	1.77	105.17

Assuming spherical particles, these PSDs were used to compute the specific surface area (SSA_{PSD}) and particle number density (N_{PSD}) per unit volume based on the following equations:

$$SSA_{PSD} = \sum_{i=1}^{j} 6V_i/D_i \ [m^2/cm^3] \quad (3\text{-}4)$$

$$N_{PSD} = \sum_{i=1}^{j} 600V_i/\pi D_i^3 \ [\#/100\mu m^3] \quad (3\text{-}5)$$

where, V_i is the volume fraction passing between two successive particle sizes, D_i is the average particle diameter between two successive particle sizes (μm), and j is the number of fractions for a given PSD.

In addition, using a 3-FLEX Micrometrics instrument, the BET specific surface area per unit volume (SSA_{BET}) of each cement and SCM was calculated from the adsorption branch of the isotherms in the range 0.05 to 0.20 of relative pressure. Table 3.4 shows the estimated SSA_{PSD} and N_{PSD}, and the measured SSA_{BET}. Normally these parameters are normalized by weight of material, however in this research they were normalized by volume, because the rheology of colloidal solutions (cementitious pastes) is governed by the volumetric proportions of their constituents (Flatt and Bowen 2006; Krieger and Dougherty 1959).

For the experimental runs with 50% of IP and 50% of FFA, the cementitious pastes were produced with different volumetric proportions of IP-Fi, IP-Co, FFA-Fi, and FFA-Co. In these cases, the particle size parameters were computed as the weighted mean of the SCMs in each experimental run.

The experimental SSA_{BET} ranged between 3 and 10 times that of the estimated SSA_{PSD} (see Table 3.4). This difference is mainly because the SSA_{BET} considers both the external and internal surfaces and surface roughness, but the internal surfaces measured by BET do not contribute to the number of contact points used in the calculation of the SSA_{PSD}. For this reason, previous researchers (Bentz et al. 2012) have found that viscosity is more strongly correlated with the SSA_{PSD} than with the SSA_{BET} of cementitious materials.

IF-Fi and IF-Co were produced to match the SSA_{PSD} of FFA-Fi and FFA-Co, respectively, with the objective to decouple the particle size and SCM type effects. IF-Fi was obtained by mixing 15.9% unmilled IF with 84.1% 7-day milled IF, while IF-Co was obtained by mixing 67.3% unmilled IF with 32.7% 7-day milled IF.

3.3.3 Mixture proportions and mixing sequence

Cementitious pastes were mixed and characterized with respect to the viscosity. The FFCCCDs described in Tables 3.1 and 3.2 were used to determine the designs of the Series I mixtures. Table 3.5 shows the six mixture designs of Series II, which were produced with different SCMs, w/c, and SCM replacements than those of the Series I mixtures. All of the Series II mixtures were produced with 50% of OPC and 50% of IPC.

Table 3.5: Series II mixture designs.

Mixture	OPC (kg/m^3)	IPC (kg/m^3)	Water (kg/m^3)	SCM (kg/m^3)	w/c (by mass)	Solid vol. Fraction	SCM (% vol. of solids)
CFA-1.49-25	473	459	599	238	0.51	0.40	25
CFA-1.33-25	504	490	572	254	0.46	0.43	25
RHA-1.44-8	591	574	591	69	0.48	0.41	8
RHA-1.44-12	565	549	591	103	0.49	0.41	12
MK-1.49-25	473	459	599	271	0.50	0.40	25
MK-1.33-25	504	490	572	289	0.45	0.43	25

The cementitious pastes were prepared with an electric stirrer. The same procedure was used for all of the mixtures at a constant blade speed (i.e., 1100 rpm) and temperature (i.e., 20 to 23 °C). The dry powders were blended for 5 min to homogenize and eliminate any clumps, and then mixed for 2 min after the water was added.

3.3.4 Equilibrium flow curve measurement

The measurements were conducted with a TA Discovery Hybrid Rheometer 2. A parallel-plate configuration, with a diameter of 25 mm, a smooth stationary base plate and a serrated superior plate was used. The gap between the plates was fixed at 1000 μm, as shown to be adequate by previous researchers (Ferraris et al. 2001b; a; Navarrete et al. 2020), to compare the rheological behavior of the different cementitious pastes.

The equilibrium flow curve measurement was started at 8 min after the contact of cement with water. The test protocol was consistent with the procedures used by previous researchers (Feys and Asghari 2019; Wallevik et al. 2015; Yuan et al. 2018). To achieve a reference state, a pre-sheared period of 60 s at a $\dot{\gamma}$ of 100 s^{-1} was executed. This was followed by a linearly decreasing $\dot{\gamma}$ ramp from 100 to 0 s^{-1} within 120 s, registering data every 0.8 s. During the entire test, the temperature of the sample was maintained at 23 °C.

Particle migration and wall slip are common problems when testing highly concentrated suspensions (i.e., cementitious pastes) on a parallel plate rheometer (Chen 2020; Feys et al. 2017). Either one of these problems can invalidate the measurements. Particularly, low viscosities can lead into particle migration and high viscosities into wall slip. Previous authors (Malvern Instruments Limited 2015) have shown that in the cases where particle migration and/or wall slip is presented, the measurements are affected by the gap size used. Therefore, the equilibrium flow curve of the experimental runs with the smallest (i.e., IF-Co-1.55-40-IPC) and largest viscosity (i.e., FFA-Co-1.24-20-OPC) were measured using three different gap sizes (i.e., 700, 850 and 1000 μm) to make sure that the chosen gap of 1000 μm will not present neither particle migration nor wall slip. For each mixture design and gap size, three repetitions were performed, which allowed the variability of each measurement to be estimated. Figure 3.3 shows the average flow curve and the variability of the results. Since the differences in equilibrium flow measurements of the three gaps are not statistically significant, it can be concluded no particle migration and/or wall slip is present on the measured flow curve of the mixtures of maximum and minimum viscosity. Thus, the chosen experimental setup used in this study will provide valid and valuable results.

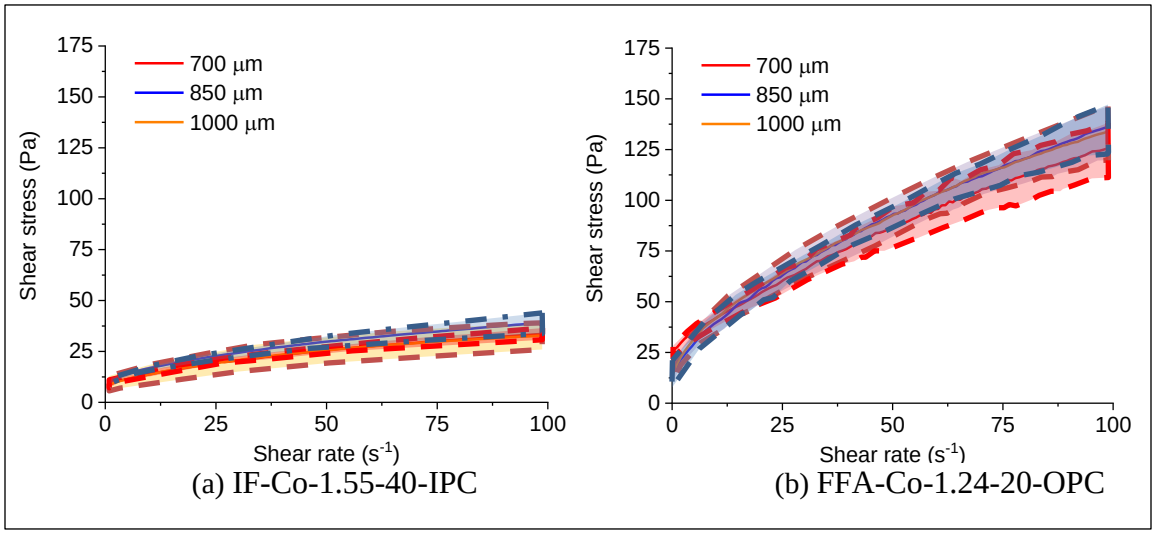

Figure 3.3: Effect of gap size on viscosity of cementitious paste. The shadow areas represent the 95% confidence interval limits for each measurement.

3.4 Results and discussion

3.4.1 Equilibrium flow curves

Figure 3.4 shows the equilibrium flow curves measured on the Series I and Series II mixtures. Romero *et al.* (Romero et al. 2018) have shown that, in colloidal suspensions, the particles form three dimensional networks with resistance to shear forces, and that the resistance of these networks is increasingly weakened as the shear rate increases. This factor explains the shear – thinning (i.e., viscosity decrease under increased $\dot{\gamma}$) behavior observed in all of the tested samples, which is similar to the results in previous studies (Choi et al. 2019; Feys and Asghari 2019; Struble and Sun 1995; Vance et al. 2013; Yahia and Khayat 2001; Yim et al. 2013).

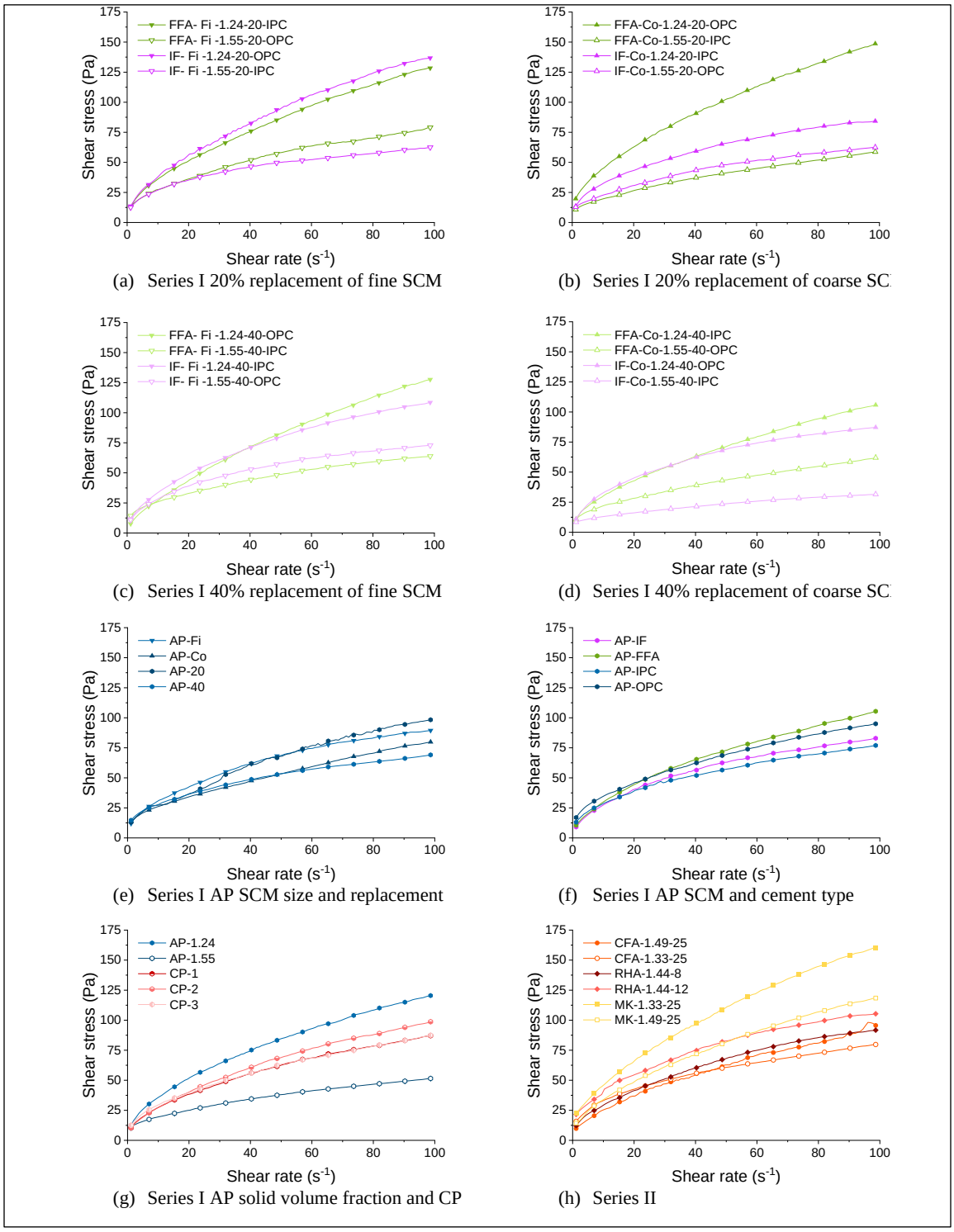

Figure 3.4: Equilibrium flow curves of cementitious pastes.

Non-linear rheological models, such as Herschel – Bulkley and modified Bingham models, fit well to the measured rheological behavior of all the mixtures. However, the added (third) term in these models increases the sensitivity of all parameters to small measurement errors (Wallevik et al. 2015), producing unstable values of the yield stress and viscosity predictions and making the analysis of the results more complicated.

Feys and Asghari (Feys and Asghari 2019) have shown that yield stress values extrapolated from flow curves are dependent on the shear rate range and the number of data points in the curve and, therefore, may not be sufficiently accurate to provide a good analysis. These authors proposed to use the shear stress at 5 s^{-1} as a value that can represent the yield stress ($\tau_{5/s}$). Even though an overestimation of the yield stress results from this approach, this error should be similar for all the mixtures. Therefore, the $\tau_{5/s}$ parameter can be used to compare the τ_0 of different mixtures. Table 3.6 shows the $\tau_{5/s}$ values calculated for each mixture.

Since different concrete applications result in different $\dot{\gamma}$ (Choi et al. 2019; Feys et al. 2013, 2016; Feys and Asghari 2019; Kim et al. 2015), it is important to analyze the viscosity of the cementitious pastes in different $\dot{\gamma}$ ranges. As a representative example, Figure 3.5 shows the measured equilibrium flow curve of IF-Fi-1.24-20-OPC. It can be seen that the slopes of the curve in the shear rate ranges of 10 to 40 s^{-1}, which is critical for gravity induced flow (Kim et al. 2015), and 60 to 90 s^{-1}, which is critical for SCC during

pumping (Feys et al. 2013, 2016), are almost constant but considerably different from each other. Therefore, linear fits to the data within both $\dot{\gamma}$ ranges were determined, and the slopes of these lines were taken as high and low $\dot{\gamma}$ viscosity values (i.e., μ^H and μ^L, respectively) of each sample. Table 3.6 shows the μ^H and μ^L calculated for each mixture. This simple procedure allows for more stable determination of viscosity, and analysis of the effects of the studied parameters on viscosity at different $\dot{\gamma}$.

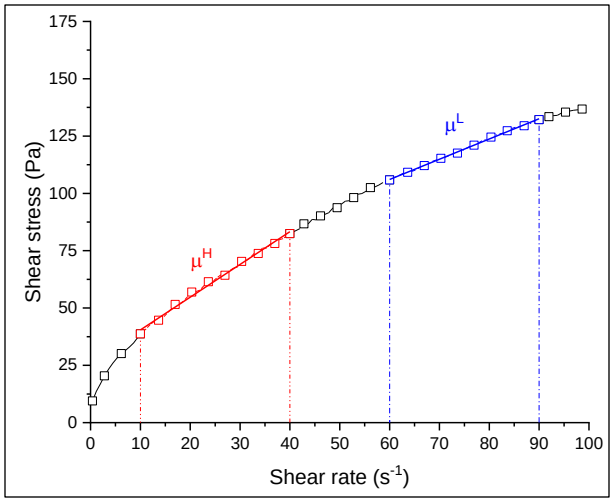

Figure 3.5: Linear fittings used to calculate μ^H and μ^L from the measured equilibrium flow curve of IF-Fi-1.24-20-OPC mix.

Table 3.7 shows that by changing the SCM properties and their interactions with the primary mixture parameters, it was possible to get an extensive range of viscosities. Specifically, μ^H ranged between 0.27 and 1.52 Pa · s and μ^L was between 0.15 and 1.02 Pa · s. The μ^L/μ^H ratio of each sample ranged between 0.37 and 0.82, with an average value of 0.53.

Table 3.6: μ_H and μ_L results.

	Mix ID	$\tau_{5/s}$	μ^H	μ^L
Series I	IF- Fi -1.24-20-OPC	27.1	1.43	0.88
	IF-Co-1.24-20-IPC	22.4	0.86	0.41
	IF- Fi -1.55-20-IPC	20.9	0.62	0.26
	IF-Co-1.55-20-OPC	17.7	0.68	0.31
	IF- Fi -1.24-40-IPC	26.3	1.07	0.56
	IF-Co-1.24-40-OPC	20.5	0.94	0.35
	IF- Fi -1.55-40-OPC	20.5	0.66	0.28
	IF-Co-1.55-40-IPC	10.9	0.27	0.15
	FFA- Fi -1.24-20-IPC	25.7	1.28	0.83
	FFA-Co-1.24-20-OPC	33.0	1.50	0.94
	FFA- Fi -1.55-20-OPC	20.8	0.82	0.36
	FFA-Co-1.55-20-IPC	12.4	0.59	0.35
	FFA- Fi -1.24-40-OPC	24.1	1.47	0.94
	FFA-Co-1.24-40-IPC	19.8	1.06	0.71
	FFA- Fi -1.55-40-IPC	21.2	0.60	0.29
	FFA-Co-1.55-40-OPC	17.2	0.57	0.37
	AP-Fi	24.4	1.03	0.39
	AP-Co	20.7	0.69	0.56
	AP-1.24	25.6	1.26	0.75
	AP-1.55	15.7	0.50	0.26
	AP-20	26.0	1.04	0.62
	AP-40	22.4	0.68	0.28
	AP-IF	19.1	0.95	0.38
	AP-FFA	20.1	1.15	0.66
	AP-IPC	21.8	0.78	0.36
	AP-OPC	27.1	0.91	0.52
	CP-1	19.5	0.92	0.46
	CP-2	19.0	1.08	0.55
	CP-3	22.1	0.86	0.49
Series II	CFA-1.49-25	17.1	0.73	0.39
	CFA-1.33-25	22.3	0.96	0.55
	RHA-1.44-8	23.9	1.01	0.47
	RHA-1.44-12	19.7	1.04	0.46
	MK-1.49-25	22.0	1.24	0.76
	MK-1.33-25	30.3	1.52	1.02

3.4.2 Effect of number of contact points on viscosity

The number of contact points of the particles in a colloidal suspension is mainly determined by the PSD and solid volume fraction. The measurement of the equilibrium flow curve was performed within a couple of minutes after the initial contact of the cementitious materials with water. Since significant chemical reactions could not develop in such as short period of time (Scherer et al. 2012), the chemical reactivity of the materials was not a significant parameter in the rheological behavior. As such, the properties derived by the combined PSD of the cementitious materials for each mixture, which are the specific surface area and the particle number density, denoted as SSA_T^{PSD} and N_T^{PSD}, respectively, were calculated with the following equations:

$$SSA_T^{PSD} = \frac{V_c(SSA_c^{PSD}) + V_{SCM}(SSA_{SCM}^{PSD})}{V_c + V_{SCM}} \quad (3\text{-}6)$$

$$N_T^{PSD} = \frac{V_c(N_c^{PSD}) + V_{SCM}(N_{SCM}^{PSD})}{V_c + V_{SCM}} \quad (3\text{-}7)$$

where, V_c and V_{SCM} are the volume fractions of the cement and SCM, SSA_{SCM}^{PSD} and N_{SCM}^{PSD} are the SSA_{PSD} and N_{PSD} of the SCM, and SSA_c^{PSD} and N_c^{PSD} are the SSA_{PSD} and N_{PSD} of the cement, respectively.

Table 3.7: Particle size properties calculated for blended power of each mixture.

	Mix ID	SSA_T^{PSD}	N_T^{PSD}
Series I	IF- Fi -1.24-20-OPC	1.42	91.6
	IF-Co-1.24-20-IPC	1.25	80.8
	IF- Fi -1.55-20-IPC	1.42	83.5
	IF-Co-1.55-20-OPC	1.25	88.9
	IF- Fi -1.24-40-IPC	1.54	77.1
	IF-Co-1.24-40-OPC	1.19	77.8
	IF- Fi -1.55-40-OPC	1.54	83.2
	IF-Co-1.55-40-IPC	1.20	71.7
	FFA- Fi -1.24-20-IPC	1.41	83.1
	FFA-Co-1.24-20-OPC	1.24	90.6
	FFA- Fi -1.55-20-OPC	1.41	91.2
	FFA-Co-1.55-20-IPC	1.25	82.5
	FFA- Fi -1.24-40-OPC	1.51	82.5
	FFA-Co-1.24-40-IPC	1.19	75.1
	FFA- Fi -1.55-40-IPC	1.52	76.4
	FFA-Co-1.55-40-OPC	1.18	81.1
	AP-Fi	1.47	83.5
	AP-Co	1.21	81.0
	AP-1.24	1.34	82.3
	AP-1.55	1.34	82.3
	AP-20	1.33	86.5
	AP-40	1.35	78.1
	AP-IF	1.35	81.8
	AP-FFA	1.33	82.8
	AP-IPC	1.34	78.7
	AP-OPC	1.34	85.9
	CP	1.34	82.3
Series II	CFA-1.49-25	1.37	89.5
	CFA-1.33-25	1.37	89.5
	RHA-1.44-8	1.33	94.5
	RHA-1.44-12	1.35	94.3
	MK-1.49-25	1.42	98.0
	MK-1.33-25	1.42	98.0

Table 3.7 provides the calculated properties for the cementitious particles of each mixture. Note that it is unknown if the particle size effect is more accurately represented

by SSA_T^{PSD} or N_T^{PSD}. Therefore, two different sets of SOPR models were developed using SSA_T^{PSD} or N_T^{PSD} separately, in order to determine which one has the greater effect on viscosity. In addition to the particle size parameter, the ϕ_T of each mixture was included to develop these models.

The first set of SOPR models for μ^H and μ^L was developed using SSA_T^{PSD} and ϕ_T as the model parameters. The resulting models are represented in Eq. (3-8) and (3-9), respectively, with summary and coefficients (i.e., $\alpha_1^h..\alpha_3^h, \alpha_1^l..\alpha_3^l$) of the terms in each equation given in Table 3.8.

$$\mu^H = \alpha_1^h SSA_T^{PSD} + \alpha_2^h \phi_T + \alpha_3^h \phi_T^2 \quad (3\text{-}8)$$

$$\mu^L = \alpha_1^l \phi_T + \alpha_2^l (SSA_T^{PSD})^2 + \alpha_3^l SSA_T^{PSD} \phi_T \quad (3\text{-}9)$$

Table 3.8: Coefficients of SOPR models developed using SSA_T^{PSD} [i.e., eq. (3-8) and (3-9)]

		Coefficient	Standard error	T-statistic	P-value	95% C.I. ($\pm$)
μ^H	α_1^h	+ 6.49 x 10^{-1}	2.98 x 10^{-1}	+2.18	0.039	6.15 x 10^{-1}
	α_2^h	- 1.13 x 10^{1}	2.41 x 10^{0}	- 4.67	0.000	4.97 x 10^{0}
	α_3^h	+ 2.70 x 10^{1}	4.16 x 10^{0}	+6.48	0.000	8.59 x 10^{0}
μ^L	α_1^l	- 5.98 x 10^{0}	1.47 x 10^{0}	- 4.08	0.000	3.03 x 10^{0}
	α_2^l	- 1.51 x 10^{-1}	2.82 x 10^{-1}	- 5.36	0.000	5.81 x 10^{-1}
	α_3^l	+ 1.02 x 10^{0}	1.91 x 10^{0}	+5.34	0.000	3.94 x 10^{0}

The second set of SOPR models for μ^H and μ^L were developed using N_T^{PSD} and ϕ_T as parameters. The resulting models are represented in Eq. (3-10) and (3-11), respectively,

with summary and coefficients (i.e., $\beta_1^h..\beta_4^h, \beta_0^l..\beta_4^l$) of the terms in each equation given in Table 3.9.

$$\mu^H = \beta_1^h N_T^{PSD} + \beta_2^h \phi_T + \beta_3^h \phi_T^2 \quad (3\text{-}10)$$

$$\mu^L = \beta_1^l \phi_T + \beta_2^l (N_T^{PSD})^2 + \beta_3^l N_T^{PSD} \phi_T \quad (3\text{-}11)$$

Table 3.9: Coefficients of SOPR models developed using N_T^{PSD} [i.e., Eq. (3-10) and (3-11)]

		Coefficient	Standard error	T-statistic	P-value	95% C.I. (±)
μ^H	β_1^h	+ 2.71 x 10^{-2}	5.19 x 10^{-3}	+5.21	0.000	1.07 x 10^{-2}
	β_2^h	- 1.77 x 10^{1}	2.31 x 10^{0}	- 7.65	0.000	4.76 x 10^{0}
	β_3^h	+ 3.45 x 10^{1}	3.55 x 10^{0}	+9.72	0.000	7.32 x 10^{0}
μ^L	β_1^l	- 8.78 x 10^{0}	1.39 x 10^{0}	- 6.30	0.000	2.88 x 10^{0}
	β_2^l	- 4.01 x 10^{-4}	6.30 x 10^{-5}	- 6.37	0.000	1.30 x 10^{-4}
	β_3^l	+ 2.00 x 10^{-1}	2.73 x 10^{-2}	+7.34	0.000	5.63 x 10^{-2}

Figure 3.6 presents comparisons between the experimental measurements and the results predicted with the first and second set of SOPR models. The second set of SOPR models was able to achieve better predictions of the Series I and II μ^H and μ^L data. Thus, it is concluded that N_T^{PSD} is a better predictor of the observed variability in μ^H and μ^L than SSA_T^{PSD}. Navarrete *et al.* (Navarrete et al. 2020) showed that N_T^{PSD} has a more significant effect on the number of contact points than SSA_T^{PSD}. A higher number of contact points increases the strength of the network produced between the particles and, therefore, the μ^H and μ^L of the cementitious paste. It is important to note that the number of contact points,

which is determined by the combined effect of N_T^{PSD} and ϕ_T, is able to explain over the 75% and 60% of the experimental variability of μ^H and μ^L, respectively.

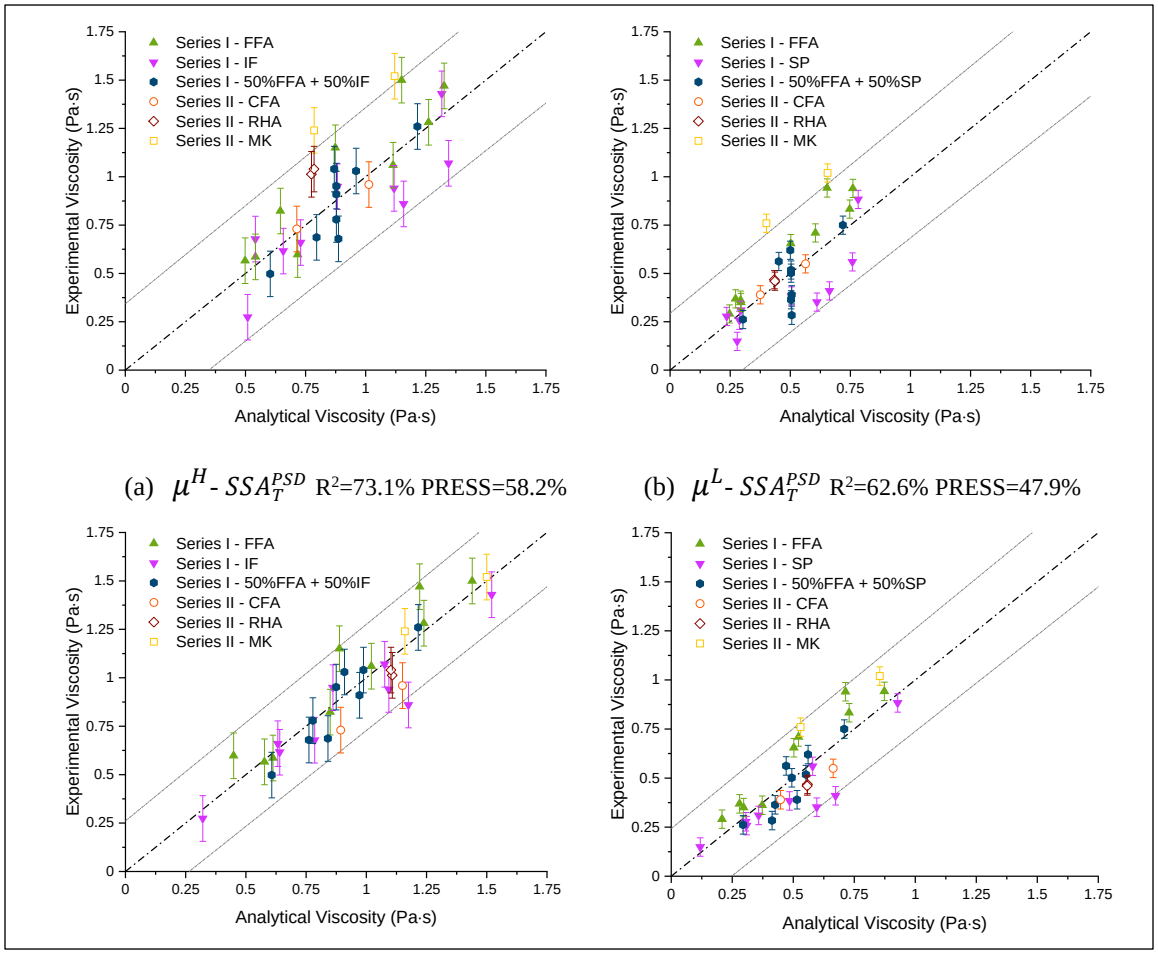

(a) μ^H - SSA_T^{PSD} R^2=73.1% PRESS=58.2%

(b) μ^L - SSA_T^{PSD} R^2=62.6% PRESS=47.9%

(c) μ^H - N_T^{PSD} R^2=84.9% PRESS=77.2%

(d) μ^L - N_T^{PSD} R^2=74.5% PRESS=60.0%

Figure 3.6: Relationship between experimental and analytical viscosity (i.e., μ^H and μ^L). (a) Prediction of μ^H using Eq. (3-8); (b) Prediction of μ^L using Eq. (3-9); (c) Prediction of μ^H using Eq. (3-10); (d) Prediction of μ^L using Eq. (3-11). Gray continuous lines represent the 95% confidence interval limits for each model. Black discontinuous lines represent perfect correlation between the experimental and analytical results.

3.4.3 Effect of interparticle force on viscosity

Previous researchers (Ohshima and Makino 2014) have shown that the particles of colloidal suspensions flocculate and form three dimensional networks. Since the mixtures were tested within a few minutes after mixing, they did not have significant cementitious reactions. Therefore, the main forces were those common in colloidal suspensions, namely the Van der Waals attractive force (F_{VDW}) and the electrostatic repulsive force (F_{ES}) (Derjaguin and Landau 1941; Verwey 1947; Zhou et al. 1999).

For non-spherical particles (i.e., cementitious particles), F_{VDW} can be calculated with Eq. (3-12).

$$F_{VDW} = \frac{A_0 a^*}{12h^2} \tag{3-12}$$

where, A_0 is the Hamaker constant (Flatt 2004), h is the surface-to-surface separation, and a^* is the radius of curvature at the pseudo-contact points. Previous researches have shown that a^* is determined by the shape of the particles and not by their radius (Flatt and Bowen 2006).

When two particles with double layers of the same sign, which is the case for cementitious particles, approach a value of h that is smaller than twice the Debye length (κ^{-1}), double layer repulsion occurs, because the two double layers cannot be fully

extended in the confined space (Ohshima and Makino 2014). This leads to the electrostatic repulsive force, $F_{ES,}$ which can be calculated with the following equation:

$$F_{ES} = -\frac{2\pi\epsilon_r\epsilon_0 a^* \zeta_T^2 \left(\kappa e^{-\kappa(h-2L_e)}\right)}{1+e^{-\kappa(h-2L_e)}} \tag{3-13}$$

where, ϵ_r is the permittivity constant of the medium, ϵ_0 is the permittivity constant of free space, ζ_T is the zeta potential, and L_e is the distance from the particle surface used as the plane of origin for the electrostatic repulsion.

The total interaction force can be obtained by taking the sum of F_{VDW} and F_{ES}. As both forces depend linearly on a^*, Flatt and Bowen (Flatt and Bowen 2006) defined an interparticle force parameter, $G_{(h)}$, which is independent of the particle size and is given by:

$$G_{(h)} = \frac{F_{VDW}+F_{ES}}{a^*} \tag{3-14}$$

The aim of this section is evaluate if the effect of $G_{(h)}$, which is related to the bonding strength of cementitious particles, and the combined effect of N_T^{PSD} and ϕ_T, which are related to the amount of contact points, can better explain the variability observed in μ^H and μ^L.

Flatt and Bowen (Flatt and Bowen 2006, 2007) developed the Yield Stress Model (YODEL) for colloidal suspensions, which incorporates $G_{(h)}$ and the number of interacting particles through the volume fraction, packing, and size distribution of solid particles. In

the case of suspensions with a high volume fraction of solids (i.e., $\phi_T > 0.25$) and non-spherical particles, which is the case for cementitious pastes, the following expression has been validated by previous studies (Hot et al. 2014; Roussel et al. 2010; Zhu et al. 2020):

$$\tau_0 \cong \left(\frac{F_{\sigma,\Delta}}{(R^{50})^2}\right)\left(\frac{\phi_T^3}{\phi_m(\phi_m-\phi_T)}\right) G_{(h)} \quad (3\text{-}15)$$

where, R^{50} is the median radius in μm, $F_{\sigma,\Delta}$ is the volumetric size distribution function (unitless), and ϕ_m is the maximum packing density.

Using Eq. (3-15), the PSD of the cementitious particles, and the measured τ_0 of the cementitious mixtures, the average $G_{(h)}$ of cementitious pastes can be estimated. Specifically, d was estimated as the average radius of the cementitious particles R^{50} using Eq. (3-16), $F_{\sigma,\Delta}$ was calculated following the procedure from Flatt and Bowen (Flatt and Bowen 2006), ϕ_{max} took a value for randomly closed packing (Choi et al. 2019) (i.e., ϕ_m= 0.63), and τ_0 was defined as $\tau_{5/s}$.

$$R^{50} = \frac{1}{2}\left(\frac{600}{\pi N_{PSD}}\right)^{\frac{1}{3}} \quad (3\text{-}16)$$

Table 3.10 shows the R^{50}, $F_{\sigma,\Delta}$ and $G_{(h)}$ values calculated for each mixture. The R^{50} values were between 0.6 and 0.7 μm, similar to the estimations by Roussel et al. (Roussel et al. 2010). In the case of $F_{\sigma,\Delta}$, the estimated values ranged between 300 and 500, similar to the values reported in the literature (Flatt and Bowen 2006; Zhu et al. 2020).

Table 3.10: R^{50}, $F_{\sigma,\Delta}$ and $G_{(H)}$ values estimated for the Series I and Series II mixtures.

	Mix ID	R^{50} (μm)	$F_{\sigma,\Delta}$	$G_{(h)}$ (10^{-14} N)
Series I	IF- Fi -1.24-20-OPC	0.64	418.6	3.05
	IF-Co-1.24-20-IPC	0.67	461.9	2.62
	IF- Fi -1.55-20-IPC	0.66	436.5	4.89
	IF-Co-1.55-20-OPC	0.65	435.6	3.98
	IF- Fi -1.24-40-IPC	0.68	434.6	3.37
	IF-Co-1.24-40-OPC	0.67	477.3	2.38
	IF- Fi -1.55-40-OPC	0.66	422.1	4.96
	IF-Co-1.55-40-IPC	0.69	505.8	2.42
	FFA- Fi -1.24-20-IPC	0.66	365.3	3.73
	FFA-Co-1.24-20-OPC	0.64	436.6	3.78
	FFA- Fi -1.55-20-OPC	0.64	355.3	5.63
	FFA-Co-1.55-20-IPC	0.66	461.9	2.77
	FFA- Fi -1.24-40-OPC	0.66	318.9	4.03
	FFA-Co-1.24-40-IPC	0.68	500.8	2.24
	FFA- Fi -1.55-40-IPC	0.68	322.6	7.09
	FFA-Co-1.55-40-OPC	0.67	474.8	3.75
	AP-Fi	0.66	375.6	4.84
	AP-Co	0.67	466.9	3.37
	AP-1.24	0.66	417.8	3.26
	AP-1.55	0.66	417.8	3.85
	AP-20	0.65	418.4	4.53
	AP-40	0.67	417.2	4.19
	AP-IF	0.66	449.8	3.20
	AP-FFA	0.66	391.1	3.84
	AP-IPC	0.67	426.8	3.96
	AP-OPC	0.65	409.8	4.84
	CP	0.66	417.8	3.63
Series II	CFA-1.49-25	0.64	455.9	2.45
	CFA-1.33-25	0.64	455.9	4.26
	RHA-1.44-8	0.63	470.1	3.84
	RHA-1.44-12	0.63	470.1	3.17
	MK-1.49-25	0.62	408.2	4.20
	MK-1.33-25	0.62	408.2	4.05

To analyze the effect of $G_{(h)}$ on μ^H and μ^L, two additional SOPR models were developed, which also included N_T^{PSD} and ϕ_T as parameters. The resulting models are presented in Eq. (3-17) and (3-18), respectively, with summary and coefficients (i.e., $\gamma_1^h..\gamma_4^h, \gamma_1^l..\gamma_5^l$) of the terms given in Table 3.11.

$$\mu^H = \gamma_1^h N_T^{PSD} + \gamma_2^h \phi_T + \gamma_3^h \phi_T^2 + \gamma_4^h G_{(h)} \phi_T \quad (3\text{-}17)$$

$$\mu^L = \gamma_1^l G_{(h)} + \gamma_2^l \phi_T + \gamma_3^l N_T^{PSD} \phi_T + \gamma_4^l G_{(h)} \phi_T \quad (3\text{-}18)$$

Table 3.11: Coefficients of SOPR models developed using N_T^{PSD} (i.e., eq. (3-17) and (3-18)]

		Coefficient	Standard error	T-statistic	P-value	95% C.I. (±)
μ^H	γ_1^h	+ 2.56 x 10^{-2}	3.16 x 10^{-3}	+8.11	0.000	6.46 x 10^{-3}
	γ_2^h	- 1.90 x 10^{1}	1.78 x 10^{0}	- 10.71	0.000	3.64 x 10^{0}
	γ_3^h	+ 3.73 x 10^{1}	3.05 x 10^{0}	+12.21	0.000	6.24 x 10^{0}
	γ_4^h	+ 1.35 x 10^{-1}	5.42 x 10^{-2}	+2.49	0.019	1.11 x 10^{-1}
μ^L	γ_1^l	- 8.92 x 10^{-1}	1.26 x 10^{-1}	- 7.08	0.000	2.58 x 10^{-1}
	γ_2^l	- 2.19 x 10^{0}	6.50 x 10^{-1}	- 3.37	0.002	1.33 x 10^{0}
	γ_3^l	+ 3.47 x 10^{-2}	7.74 x 10^{-3}	+4.48	0.000	1.58 x 10^{-2}
	γ_4^l	+ 2.28 x 10^{0}	3.39 x 10^{-1}	+6.71	0.000	6.94 x 10^{-1}

Comparisons between the experimental measurements and the results estimated using these SOPR models are shown in Figure 3.7. The model for μ^H was better in explaining the observed variability (86.7%) than the model for μ^L (75.4%). This is likely because, as the shear rate increases, the bond strength of the three dimensional network

formed by the particles is increasingly weakened (Romero et al. 2018), which resulted in reduced effect of $G_{(h)}$ at higher shear rates.

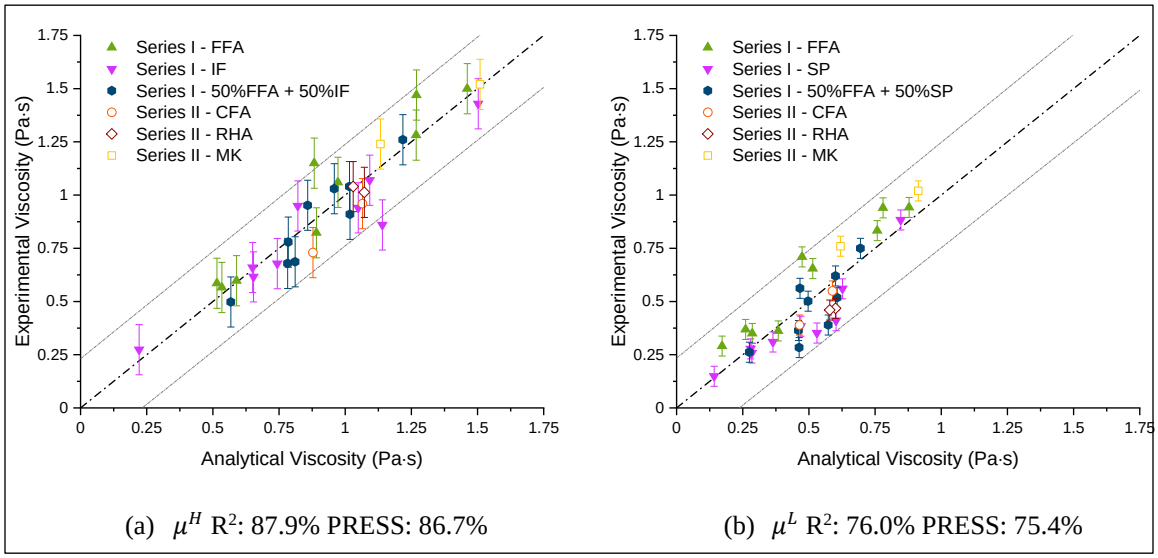

(a) μ^H R^2: 87.9% PRESS: 86.7%

(b) μ^L R^2: 76.0% PRESS: 75.4%

Figure 3.7: Relationship between experimental and analytical viscosity (i.e., μ^H and μ^L). (a) Prediction of μ^H using Eq. (3-17); (b) Prediction of μ^L using Eq. (3-18). Gray continuous lines represent the 95% confidence interval limits for each model. Black discontinuous lines represent perfect correlation between the experimental and analytical results.

Figure 3.8 shows that out of the 3 model parameters, ϕ_T has the largest effect on both viscosities (i.e., μ^H and μ^L), followed by N_T^{PSD} and $G_{(h)}$. This means that the w/c, which governs the ϕ_T of the mixture, has a greater effect on viscosity than the properties of the cementitious particles. In addition, among the cementitious material properties, the particle size has a greater effect on μ^H and μ^L than the interparticle force parameter. The

combined effect of N_T^{PSD} and ϕ_T is a good estimator of the number of contact points of this network, explaining most of the observed variability in μ^H and μ^L.

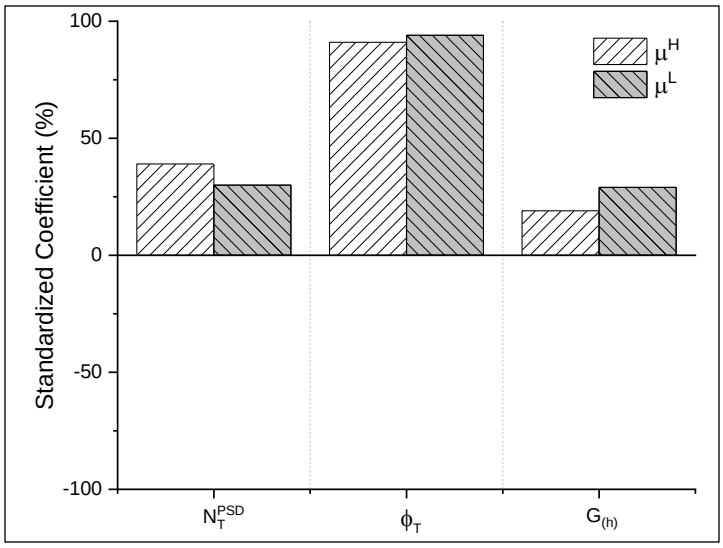

Figure 3.8: Standardized coefficients for N_T^{PSD}, ϕ_T, and $G_{(h)}$ of the SOPR model.

Increases in N_T^{PSD} and ϕ_T produce increases in both viscosities, as shown by the standardized coefficients in Figure 3.8. This is expected, because an increase in either parameter increases the number of contact points between particles and, therefore, increases the shear stress at different shear rates. In addition, the fact that the $\left(N_T^{PSD}\right)^2$ term has a positive effect in Eq. (3-17) means that a variation of N_T^{PSD} is more significant on μ^H for larger N_T^{PSD} values.

Increases in $G_{(h)}$ result in increases in μ^H and μ^L (see Figure 3.8). This effect is produced because an increase in $G_{(h)}$ increases the interparticle force and, therefore, increases the shear stress at different shear rates.

Eq. (3-17) and (3-18) show that the interaction between $G_{(h)}$ and ϕ_T has a positive effect on μ^H and μ^L, which means that cementitious pastes with larger ϕ_T are more affected by $G_{(h)}$. In addition, Eq. (3-18) shows that the interaction between N_T^{PSD} and ϕ_T produces a positive effect on μ^L, which means that μ^L is more affected by N_T^{PSD} in cementitious pastes with larger ϕ_T. These results can be expected because larger ϕ_T means that there are more solid particles in the mixture and, therefore, the interaction among those particles increases.

The validated SOPR models [i.e., Eq. (3-17) and (3-18)] were used to map the combined effects of the cementitious particle properties (i.e., $G_{(h)}$ and N_T^{PSD}) on μ^H and μ^L, for selected values of ϕ_T. These response surfaces allow for a better understanding of the interactions of the cementitious particle properties. The selected values of ϕ_T were 0.42, which is the ϕ_T value of the CP in Series I mixtures (see Table 3.1), and 0.45, which is the maximum ϕ_T value of the Series I mixtures. Figures 3.9.a and 3.9.b present the results for μ^H and μ^L, respectively, for ϕ_T of 0.42, while Figures 3.9.c and 3.9.d present the results of μ^H and μ^L, respectively, for ϕ_T of 0.45. The experimental values for Series I are included in Figure 3.9 to show the combinations of ϕ_T, N_T^{PSD}, and $G_{(h)}$ that were tested.

The results suggest that in the case of μ^H, the combined effect of $G_{(h)}$ and N_T^{PSD} is not dependent of ϕ_T since the relative distances between the iso-response curves in Figures 3.9.a and 3.9.c are similar. In the case of μ^L, the combined effect of $G_{(h)}$ and N_T^{PSD} increases for increased ϕ_T since the relative distances between the iso-response curves in Figure 3.9.b are greater than those in Figure 3.9.d. In addition, the effect of $G_{(h)}$ relative to the effect of N_T^{PSD} is more significant on μ^L than on μ^H, since the slopes of the iso-response curves are higher in Figure 3.9.b and Figure 3.9.d than those in Figure 3.9.a and Figure 3.9.c. Furthermore, in the case of μ^H, N_T^{PSD} has a larger effect than $G_{(h)}$ for all the combinations studied and both ϕ_T values, since the slopes of all of the iso-response curves are below 45 degrees to the horizontal axis. In the case of μ^L, N_T^{PSD} has a larger effect than $G_{(h)}$ for the lower ϕ_T (i.e., 0.42), but the opposite trend is observed for the larger ϕ_T (i.e., 0.45).

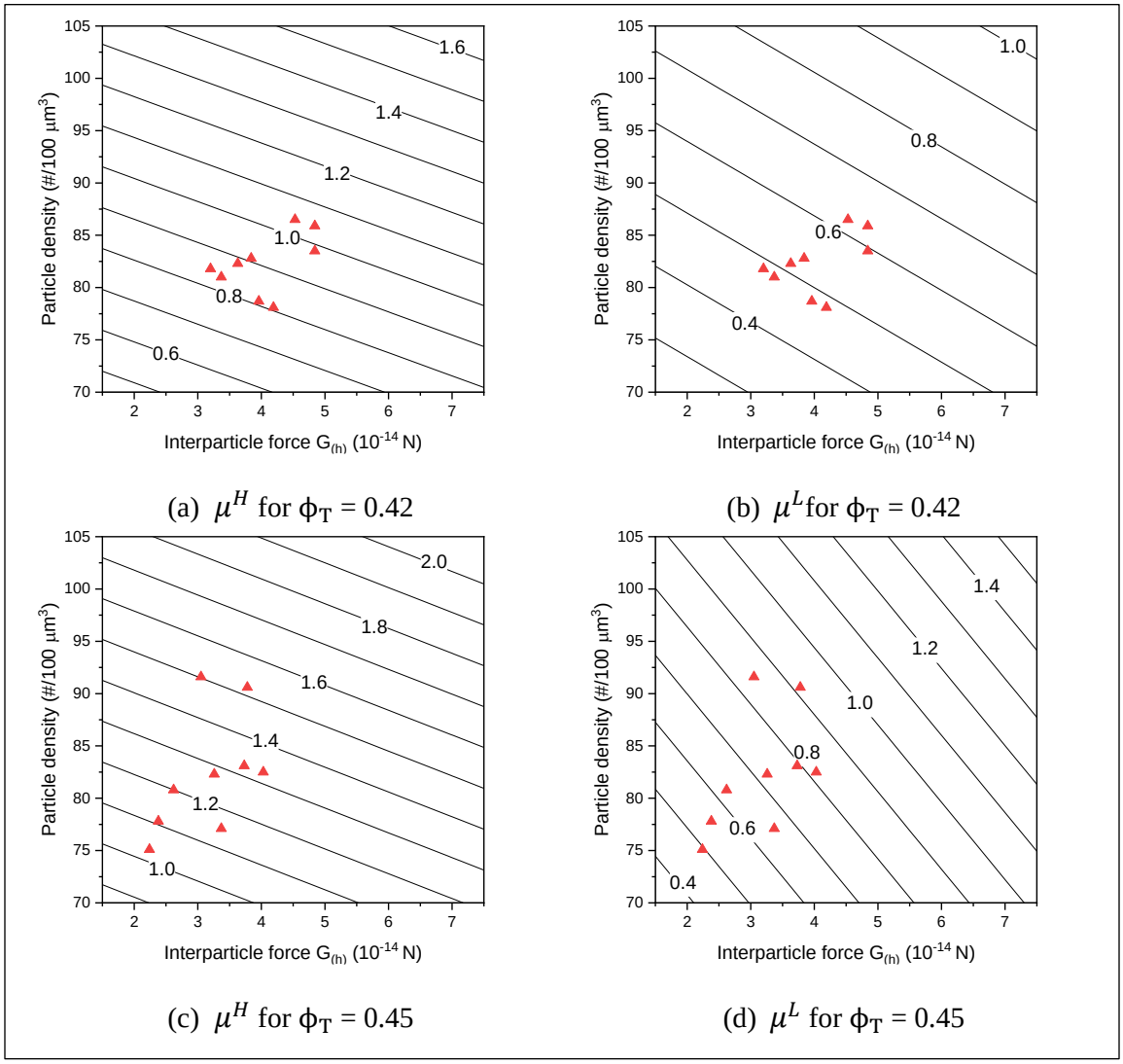

Figure 3.9: Effect of interparticle force and particle number density on μ^H and μ^L estimated with the SOPR models [i.e., Eq. (3-17) and (3-18)] for two different solid volume fractions. Red triangles represent the experimental data of Series I.

3.4.4 Effect of cementitious particles properties on interparticle force

In the previous section, the effect of $G_{(h)}$ on the viscosity of cementitious pastes was analyzed. The aim of the current section is to evaluate the effects of the experimental factors on $G_{(h)}$, and use that information to determine the cementitious material properties that govern the interparticle force of the paste.

In order to evaluate the effects of the SCM properties and the mixture design, the values of $G_{(h)}$ were normalized with respect to the average $G_{(h)}$ of the FFD runs, which is 3.79×10^{-14} N. The average normalized $G_{(h)}$ for the low and high levels of each experimental factor, calculated with the results from the FFD runs, are presented in Figure 3.10.

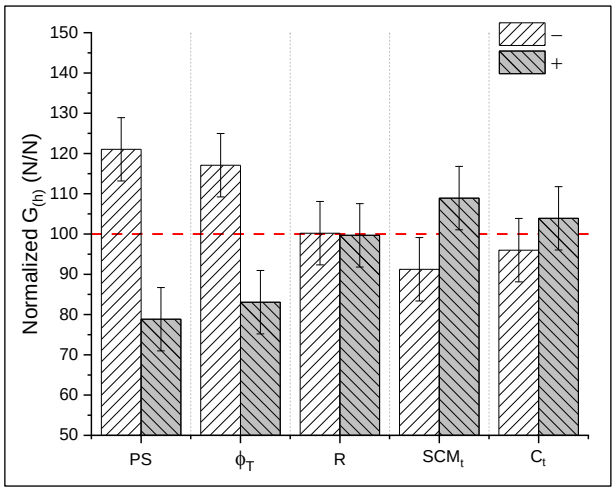

Figure 3.10: Average normalized $G_{(h)}$ for low (-) and high (+) levels of each experimental factor

Figure 3.10 shows that the SCM particle size has a significant effect on $G_{(h)}$, disputing previous studies (Flatt and Bowen 2006, 2007), which have shown that $G_{(h)}$ is independent of the particle size. Importantly, the surface roughness of the materials in the previous studies was not affected by the particle size. However, in the current research, the fine SCMs were obtained through a milling process, which increased the surface roughness of the SCMs, as can be seen in Figure 3.11. Particles with a small surface roughness present a larger average minimum separation distance (Flatt and Bowen 2006), which results a reduction in the interparticle force, as has been shown by Jallo *et al.* (Jallo et al. 2011). Therefore, the observed effect of particle size on the interparticle force can be explained by the change of the surface roughness.

The increase of ϕ_T from 0.39 to 0.45 resulted in decreased $G_{(h)}$. This finding can be explained because increased ϕ_T indicates increased OPC/water ratio, which produces a reduction of the Ca^{+2}/SO_4^{-2} ratio of the pore solution (Lowke and Gehlen 2017). Lowke and Gehlen (Lowke and Gehlen 2017) have shown that the zeta potential, ζ_T of the cementitious particles is governed by the Ca^{+2}/SO_4^{-2} ratio and that a change in ϕ_T from 0.39 to 0.45 results in a reduction of the absolute value of ζ_T. As shown in Eq. (3-13), an increase of the absolute value of ζ_T^2 produces an increase of the repulsive electrostatic force between the particles and, therefore, a reduction in $G_{(h)}$. Thus, the effect of ϕ_T on the interparticle force can be explained by the change of ζ_T.

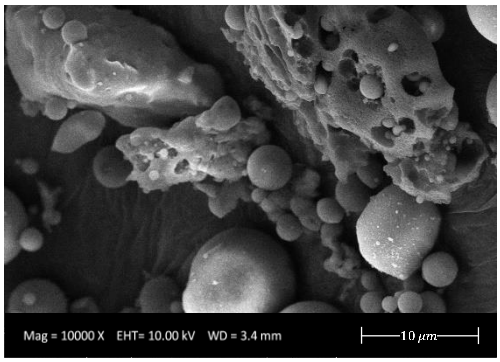

(a) FFA-Co

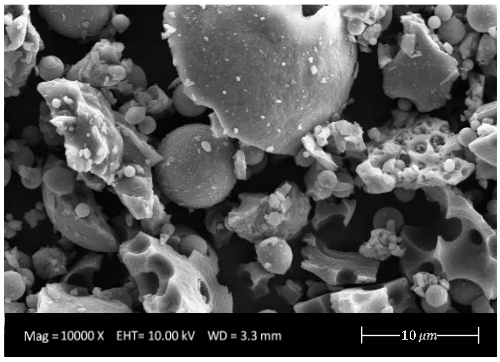

(b) FFA-Fi

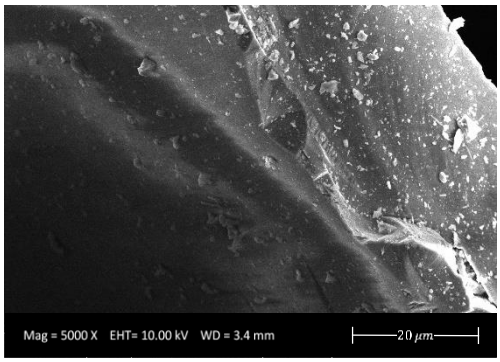

(c) non-milled IF

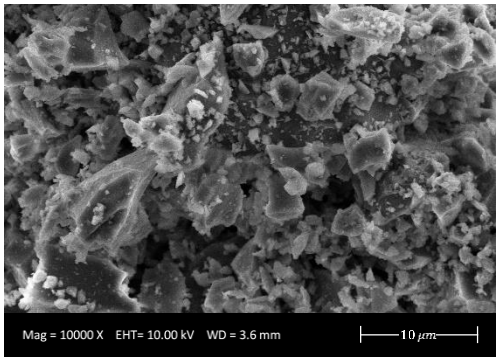

(d) 7-day milled IF

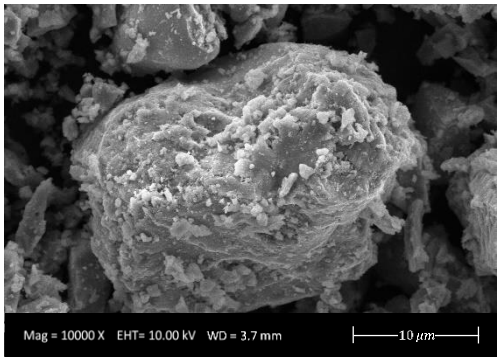

(e) OPC

Figure 3.11: SEM images of Series I SCM and OPC.

The use of FFA instead of IF produces an increase on the average $G_{(h)}$. As can be seen in Figure 3.11, the coarse IF and FFA had generally smooth surfaces and homogeneous shapes. On the other hand, the fine IF had more irregular shapes with smooth surfaces while the fine FFA had irregular shapes and surfaces. Figure 3.12 shows the average normalized $G_{(h)}$ for the different SCMs and sizes. It can be seen that the coarse IF and FFA had similar interparticle forces, while in contrast, the average interparticle force of the fine FFA was considerably larger than that of the fine IF. Therefore, the effect of the SCM type on the interparticle force can be explained by the surface roughness.

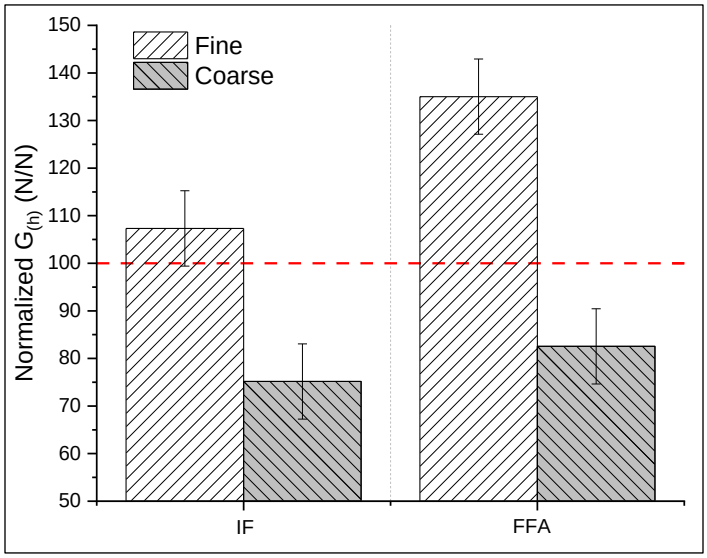

Figure 3.12: Effect of fine and coarse IF and FFA on normalized $G_{(h)}$.

Figure 3.10 shows that neither the amount of replacement nor the type of cement used in this research had a significant effect on $G_{(h)}$. This can be explained because in both cases, OPC was replaced by an SCM (i.e., FFA or IF) with a lower surface roughness (see Figure 3.11), which resulted in two opposing effects that canceled each other out. Specifically, on the one hand, the use of materials with lower surface roughness produced a negative effect on $G_{(h)}$. While on the other hand, a higher replacement or the use of IPC (i.e., 80% OPC + 20% IF) produced a reduction in the water/OPC ratio, which resulted in a reduction of ζ_T, and thus, a positive effect on $G_{(h)}$.

In summary, based on the results presented in this study, it can be concluded that the interparticle force of cementitious paste is governed by the surface roughness of the cementitious materials and their w/c, which affects the zeta potential in the cementitious paste.

3.5 Conclusions

This research investigated the effects of particle size and type of supplementary cementitious materials (SCMs) and their interactions with the main mixture parameters on the viscosity of cementitious paste. A fractional face centered central composite experimental design, composed by 29 mixtures and developed with two SCMs, was used to develop second order polynomial regression (SOPR) equation models, which were validated with an additional 6 mixtures using three different SCMs. The study focused on

SCMs with similar particle size as cement. Important conclusions from the research are listed below:

1. The effect of the particle size on the viscosity of cementitious paste is better explained by the particle number density than by the specific surface area.
2. The SOPR models were able to predict the viscosity of cementitious pastes at different shear rate ranges. The parameters that governed these models are the solid volume fraction, the interparticle force, and particle number density of the cementitious particles. The models showed good accuracy to estimate the viscosity of mixtures produced with different SCMs, SCM-cement proportions, solid volume fractions, and different cement types.
3. The viscosity of the cementitious paste is more affected by the solid volume fraction, which is determined by the water-to-cementitious materials ratio, than by the properties of the cementitious particles.
4. The interparticle force is a good predictor of the bonding strength of cementitious particles, and the combined effect of particle number density and solid volume fraction is a good estimator of the amount of contact points of this network, which explains most of the observed variability in the viscosity of cementitious paste.
5. The viscosity of cementitious paste is more affected by the number of contact points between the cementitious particles than the interparticle force between them.
6. The interparticle force is governed by the surface roughness of the cementitious materials and the w/c, which affects the zeta potential of the cementitious paste.

CHAPTER 4:

MULTI-LAYER CASTING OF SELF-CONSOLIDATING CONCRETE: INFLUENCE OF CEMENTITIOUS PASTE RHEOLOGY AND CASTING PARAMETERS ON THE INTER-LAYER BOND STRENGTH

This chapter focuses on the effect of cementitious paste volume, structural build-up of mortar, and their interactions with casting parameters (i.e., free fall height and delay time) on the inter-layer bond strength of multi-layer self-consolidating concrete (SCC), which is the third specific objective of this research. To this end, a face centered central composite experimental design, composed of 15 experimental runs was conducted. The measurements from these mixtures were then used to develop second order polynomial regression (SOPR) models, which were validated based on the results from 3 additional mixtures. The residual bond shear strength and the residual bond flexural strength were used to characterize the inter-layer bond strength of SCC.

4.1 Introduction

According to a report by the Mckinsey Global Institute (McKinsey Global Institute 2017), the global labor-productivity growth in construction lags far behind that of other manufacturing fields or the total economy. The main reason of the relatively low productivity in the construction industry is the continued dependency on traditional construction systems, which are highly labor demanding (Finger et al. 2015; Proverbs et al. 1999). In the last several decades, new technologies that can improve the productivity of concrete construction through better workability (i.e., rheology) control (Khayat and Feys 2010; Navarrete et al. 2017a; Wangler et al. 2016), such as self-consolidating concrete (SCC) and 3D concrete printing, have been developed.

The rheological behavior of yield stress fluids, such as cement-based materials (CBMs) (Jiao et al. 2017), can be defined by two parameters: yield stress and viscosity (Balmforth et al. 2013). CBMs show static (τ_0^s) and dynamic (τ_0^d) yield stress (Malvern Instruments 2012), which are the shear stress required to initiate flow and the minimum shear stress required for maintaining the flow once initiated, respectively.

Within a few minutes at rest after mixing with water, the cementitious particles form a three-dimensional network due to Van der Walls attractive forces and dielectric repulsive forces (Ferron et al. 2013; Yim et al. 2013). In addition, C-S-H bridges form and

grow at the pseudo-contact points between cement and other particles during the dormant period (Mostafa and Yahia 2017; Navarrete et al. 2020; Roussel et al. 2012). The combination of these two processes produces a time-dependent increase in τ_0^s of CBMs at rest, which is defined as the structural build-up (A_{thix}) (Yuan et al. 2017).

Among the new concrete technologies requiring better workability control, SCC is currently the most widely used (Pacheco-Torgal et al. 2013). Usually, SCC is classified by its filling ability, passing ability, and static and dynamic stability (Roussel and Cussigh 2008). From a rheological point of view, a lower τ_0^d increases the filling ability (Roussel et al. 2007), a higher viscosity improves the passing ability (Youness et al. 2020) and dynamic stability (Shen et al. 2009, 2015), and a higher τ_0^s increases the static stability (Shen et al. 2014) of the mixture.

Previous researchers (Assaad and Khayat 2006a, 2004, 2006b; Barnes and Johnston 2003; Ferraris et al. 2017; Khayat and Assaad 2007; Pierre and Picandet 2015; Roussel 2006, 2012) have recommended mixtures with high A_{thix} to reduce the formwork pressure. However, in the last decade, some studies (Assaad and Issa 2016; Megid and Khayat 2017, 2019; Roussel and Cussigh 2008; Shirzadi Javid et al. 2019) have shown that concrete with high A_{thix} may induce detrimental effects in multi-layer casting, which may occur in the case of on-site concrete delivery delays (Petit et al. 2007). After a certain period of rest, the τ_0^s of concrete increases and can reach a critical value that can produce poor intermixing

of successive layers. As vibration is not commonly used for casting SCC and may not be feasible in the case of extended delays, a distinctly weak bond can result between the successive layers, which is known as a cold joint. Losses in layer-to-layer (i.e., inter-layer) bond strength of more than 40% have been reported, and can exceed 50% when the SCC has a high A_{thix} and when the elapsed time (i.e., delay time) between the casting of two layers exceeds 30 minutes (Megid and Khayat 2017, 2019; Roussel and Cussigh 2008).

The critical delay time (DT_c) between the casting of successive SCC layers has been defined as the maximum time that allows 90% residual bond strength (Megid and Khayat 2017, 2019; Shirzadi Javid et al. 2019) as compared with the strength for continuous SCC casting. The DT_c depends on A_{thix} (Megid and Khayat 2019), aggregate interlock, and surface roughness (Shirzadi Javid et al. 2019) of the concrete mixture.

Fresh concrete can be considered as a two-phase composite material with coarse aggregate particles in a mortar fluid matrix (Tattersall and Banfill 1983; Vargas and Sciaraffia 2006). Therefore, to achieve good intermixing between successive casting layers, it is important for the mortar matrix to exhibit low τ_0^s. The interparticle force and hydration of cementitious particles are responsible for the growth of τ_0^s in CBMs at rest (Roussel et al. 2012). Therefore, the A_{thix} of a mortar mixture is governed by the amount and properties of the cementitious paste. According to Roussel and Cussigh (Roussel and Cussigh 2008), A_{thix} increases with the total amount of cementitious paste, and decreases

with the water-to-cementitious materials ratio. It has also been shown that the A_{thix} of cementitious paste increases with the fineness (Bentz et al. 2012; Mostafa and Yahia 2017) and the zeta potential (Navarrete et al. 2020) of the cementitious particles. Furthermore, the use of chemical admixtures (Ojeda-Farías et al. 2019; Roussel and Cussigh 2008), such as viscosity agents and superplasticizers, can increase A_{thix}. Other previous studies (Huang et al. 2019; Petit et al. 2007) have shown that the ambient temperature is an important factor as well, where a nonlinear increase in A_{thix} was observed in the range of 10 to 40 °C (Huang et al. 2019).

The bond strength between two successive SCC layers is highly affected by the aggregate interlock and the surface roughness of the first layer (Megid and Khayat 2017), which are mainly governed by the size, shape, and texture of the coarse aggregate, and the coarse aggregate-to-mortar ratio. Surface roughness can be improved by applying external mechanical vibration to the existing concrete layer, which would reduce its τ_0^s (Chia et al. 2005) and, therefore, increase the bond strength. Another alternative is to increase the free-fall height (H_{FF}) of the new concrete onto the existing material, which increases the interlock resulting from the penetration of the top concrete layer into the lower layer (Megid and Khayat 2019). However, these methods involving mechanical vibration and increased free-fall height can also cause segregation or bleeding, which can lead to weakened bond between the successive layers.

Increased amount of cementitious paste produces contradictory effects on the layer-to-layer bond strength. On the one hand, an increase in the amount of cementitious paste reduces the initial τ_0^s of the mortar (Ojeda-Farías et al. 2019), which increases the intermixing of successive layers. On the other hand, increased amounts of cementitious paste result in increased A_{thix} of the mortar (Roussel and Cussigh 2008), reducing DT_c, and reducing the amount of coarse aggregate, which reduces the aggregate interlock and surface roughness of the first layer (Shirzadi Javid et al. 2019). To the best of the authors' knowledge, there has been no study to establish if the amount of cementitious paste produces a positive (i.e., increasing) or negative (i.e., decreasing) effect as a result of these conflicting trends on the inter-layer bond strength of SCC.

Overall, even though previous studies have assessed the individual effects of A_{thix} and the casting process on the layer-to-layer bond strength of multi-layer SCC, the interactions between these parameters and the amount of cement paste require further investigation.

4.2 Research significance

In accordance with the research gaps identified above, this chapter discusses the effects of the cementitious paste volume, structural build-up of mortar, and their

interactions with the casting process (i.e., free fall height and delay time) on the residual bond strength of multi-layer SCC under shear and flexural stresses. In addition, the effect of cementitious paste volume, structural build-up of mortar, and their interaction with the free fall height on the critical delay time is analyzed. The results presented in the chapter can contribute to enhance the mix design and construction of SCC.

4.3 Materials and methods

4.3.1 Experimental design

The effects of cementitious paste volume, structural build-up of mortar, and their interactions with the main casting process parameters on the residual inter-layer bond strength of SCC were experimentally determined using a face-centered central composite design (FCCCD). The FCCCD is based on an embedded factorial design for the controlled variation of the experimental factors; with a center point augmented by a group of axial points, which allow quantification of curvature in the measured trends (NIST/SEMATECH 2012). The axial points are at the center of each face of the factorial space and, therefore, three levels (i.e., -, 0, +) are required in selecting the values for each experimental factor (parameter), as shown in Figure 4.1. The FCCCD permits modeling of the measured response by a second order polynomial regression (SOPR) equation, and therefore,

estimation of the main, quadratic, and interactive effects of the experimental factors on the property under study (Montgomery and Runger 2014).

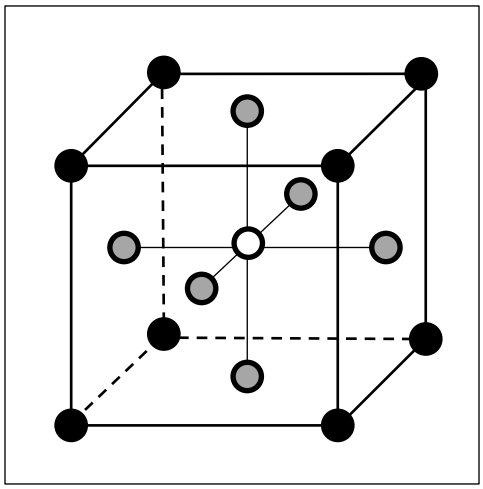

Figure 4.1: Face-centered central composite design. The experimental runs of the factorial design, axial points and center point are represented by black, grey, and white dots, respectively.

Table 4.1 shows the three selected levels for the following experimental factors investigated in this study: (1) structural build-up of mortar (A_{thix}^{m}); (2) cementitious paste volume fraction ($CP_{\%vol}$); and (3) free fall height (H_{FF}). Considering these experimental factors, a FCCCD composed by a 23 factorial design with a center point, and 2*3 axial points was developed, resulting in 15 experimental runs (i.e., Series I) as shown in Table 2. Three additional runs (i.e., Series II) were also produced to independently validate the SOPR models developed using the measured data from Series I.

Table 4.1: Selected levels of mixture design parameters and H_{FF}

	Factor Level		
Experimental Factor	-	0	+
A_{thix}^{m}	70%OPC_{ES} + 30%CFA	85% OPC_{ES} + 15%CFA	100% OPCES
$CP_{\%vol}$	33.6%	35.2%	37.0%
H_{FF}	200 mm	300 mm	400 mm

For each experimental run, the delay time (DT) between two successive layers of SCC was varied as 30 and 60 min. Moreover, for each mixture design, monolithic specimens (i.e., DT equal to 0 min) were cast as control samples. The residual bond strength was calculated by dividing the results for each DT by the corresponding values for the monolithic control samples.

Table 4.2: Series I mixtures and factorial levels.

Run	Mixture Design ID	H_{FF} (mm)	A_{thix}^{m}	$CP_{\%vol}$	H_{FF}
1	SCC-70OPC_{ES}/30CFA - 33.6%	200	-	-	-
2	SCC-100OPC_{ES}/0CFA - 33.6%	200	+	-	-
3	SCC-70OPC_{ES}/30CFA - 37.0%	200	-	+	-
4	SCC-100OPC_{ES}/0CFA - 37.0%	200	+	+	-
5	SCC-70OPC_{ES}/30CFA - 33.6%	400	-	-	+
6	SCC-100OPC_{ES}/0CFA - 33.6%	400	+	-	+
7	SCC-70OPC_{ES}/30CFA - 37.0%	400	-	+	+
8	SCC-100OPC_{ES}/0CFA - 37.0%	400	+	+	+
9	SCC-70OPC_{ES}/30CFA - 35.2%	300	-	0	0
10	SCC-100OPC_{ES}/0CFA - 35.2%	300	+	0	0
11	SCC-85OPC_{ES}/15CFA - 33.6%	300	0	-	0
12	SCC-85OPC_{ES}/15CFA - 37.0%	300	0	+	0
13	SCC-85OPC_{ES}/15CFA - 35.2%	200	0	0	-
14	SCC-85OPC_{ES}/15CFA - 35.2%	400	0	0	+
15	SCC-85OPC_{ES}/15CFA - 35.2%	300	0	0	0

A type III high-early-strength Portland cement (OPC_{ES}), with 90% of the particles below 25 μm, was used to develop the Series I and Series II mixtures, because finer cements (i.e., OPC_{ES}) produce mixtures with higher A_{thix}^{m} (Mostafa and Yahia 2017). In addition, class C fly ash (CFA) and blast furnace slag (BFS) were used as supplementary cementitious materials (SCMs) in the development of the Series I and Series II mixtures, respectively. The use of different amounts of CFA and BFS to replace OPC_{ES} allowed the study to vary A_{thix}^{m} and decouple its effect from that of $CP_{\%vol}$.

SOPR models and backward elimination algorithm (Montgomery and Runger 2014) were conducted with the 15 runs of Series I to establish the effects of each experimental parameter on the residual bond strength of multi-layer SCC and develop SOPR models. These models were then validated using the results from the Series II mixtures and the methodology proposed by Snee (Snee 1977), by comparing the deviation between the experimental and predicted results of the Series II runs with the confidence interval of each SOPR model.

4.3.2 Mixture proportions and mixing sequences

Cementitious pastes, mortars, and SCC mixtures were mixed and characterized with respect to their fresh properties, as shown in Figure 4.2. The design of the cementitious

pastes and mortars corresponded to those used for the SCC mixtures. All of the samples were mixed at laboratory room temperature (i.e., 20 to 23 °C).

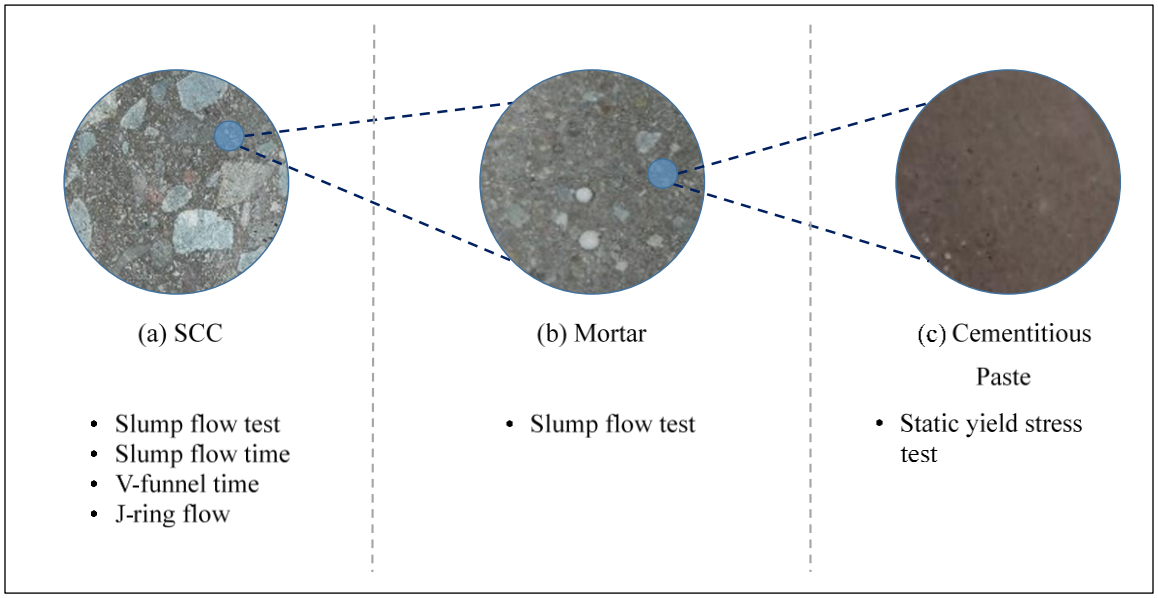

Figure 4.2: Fresh properties measured in SCC (a), mortar (b), and cementitious paste (c).

The Series I mixture designs were determined according to the FCCCD summarized in Tables 4.1 and 4.2. The Series II mixtures were produced with BFS instead of CFA, resulting in different A_{thix}^{m} than the Series I mixtures, and with different $CP_{\%vol}$ and H_{FF} than those used for the Series I mixtures, so as to result in a critical and independent evaluation of the SOPR equations from Series I. Table 4.3 presents the mixture designs of the Series I and Series II mixtures.

TABLE 4.3

SERIES I AND SERIES II MIXTURE DESIGNS

	Mixture Design ID	OPC_{ES} (kg/m^3)	SCM (kg/m^3)	Water (kg/m^3)	Fine Aggregate (kg/m^3)	Coarse Aggregate (kg/m^3)	HRWRA (kg/m^3)	$CP_{\%vol}$	Mortar (%Vol.)
Series I	SCC-100OPC_{ES}/0CFA - 33.6%	450	0	190	990	730	2.72	33.6%	70.9%
	SCC-100OPC_{ES}/0CFA - 35.2%	470	0	200	960	710	2.86	35.2%	71.6%
	SCC-100OPC_{ES}/0CFA - 37.0%	490	0	210	930	690	3.00	37.0%	72.4%
	SCC-85OPC_{ES}/15CFA - 33.6%	382	58	190	990	730	2.62	33.6%	70.9%
	SCC-85OPC_{ES}/15CFA - 35.2%	401	62	200	960	710	2.76	35.2%	71.6%
	SCC-85OPC_{ES}/15CFA - 37.0%	420	64	210	930	690	2.89	37.0%	72.4%
	SCC-70OPC_{ES}/30CFA - 33.6%	315	117	190	990	730	2.52	33.6%	70.9%
	SCC-70OPC_{ES}/30CFA - 35.2%	330	122	200	960	710	2.81	35.2%	71.6%
	SCC-70OPC_{ES}/30CFA - 37.0%	345	128	210	930	690	2.95	37.0%	72.4%
Series II	SCC-85OPC_{ES}/15BFS - 35.2%	400	65	200	960	710	2.59	35.2%	71.6%
	SCC-70OPC_{ES}/30BFS - 35.2%	330	130	200	960	710	2.59	35.2%	71.6%
	SCC-70OPC_{ES}/30BFS - 34.4%	322	127	195	975	720	2.52	34.4%	71.3%

The coarse-to-fine aggregate ratio and the water-to-cementitious materials ratio by mass were kept constant at 0.72 and 0.40, respectively, in all of the SCC mixtures. In addition, between 33% and 38% of cementitious paste was used in all mixtures, which is a common range for SCC (ACI Committee 238 2008; Saleh Ahari et al. 2015).

A high-range water reducer admixture (HRWRA) with a specific gravity of 1.08 was used in a dosage of 0.60% by cement weight for the mixtures without SCMs (i.e., SCC-100OPCES/0CFA-33.0%, SCC-100OPCES/0CFA-35.5%, and SCC-OPCES/0CFA-38.0%). In the mixtures with SCM as partial replacement of OPC_{ES}, the HRWRA dosage was adjusted to obtain the same initial slump flow ($S.\,flow_0$) as the mixtures without SCMs for the different values of $CP_{\%vol}$.

A crushed limestone aggregate with nominal maximum size of 12.7 mm and a natural river sand were used as coarse and fine aggregates, respectively. The particle size distributions (PSD) of both aggregates were within ASTM C33/C33M - 18 recommendations. The coarse and fine aggregates had fineness modulus of 6.0 and 2.5, specific gravities of 2.69 and 2.64 at the saturated surface dry condition, and water absorption of 2.11% and 1.35%, respectively.

The SCC mixtures were all prepared using the same procedure with a pan mixer. The fine and coarse aggregates were first mixed for 2 minutes, then the cementitious

materials were added and mixed for 3 minutes, and finally water and HRWRA were added and mixed for 5 more minutes.

The mortar samples were all prepared using a planetary mixer. The cementitious materials and fine aggregate were first mixed for 3 minutes, and then mixed for 5 more minutes after water and HRWRA were added.

The cementitious pastes were all prepared using an electric stirrer at a constant blade speed of 1100 rpm. The cementitious materials were first blended for 5 minutes to homogenize and eliminate any clumps, and then stirred for 2 more minutes after water was added.

4.3.3 Characterization of cementitious materials

The OPC_{ES} used in all the mixtures was in compliance with ASTM C150/C150M – 19a. Table 4.4 shows the specific gravity and oxide composition, determined by X-ray fluorescence (XRF), of the cementitious materials.

The microstructure of the cementitious materials was detected using a scanning electron microscope (SEM), which provided surface information of the studied materials. The images were taken using a Quanta 250 microscope with an accelerating voltage of 20kV and magnifications between 300x and 1,000,000x. All of the samples were oven

dried, coated with 4 nm of gold, and mounted on a holder. Figure 4.3 shows sample SEM images for the different cementitious materials at a magnification of 5,000x.

Table 4.4: Oxide composition, specific gravity, and particle size parameters of the cementitious materials.

	OPC_{ES}	CFA	BFS
CaO (%)	62.80	18.94	41.27
SiO_2 (%)	19.58	43.99	39.37
Al_2O_3 (%)	4.82	13.47	7.32
SO_3 (%)	3.50	1.50	1.69
Fe_2O_3 (%)	2.56	13.31	0.67
MgO (%)	2.78	3.22	6.64
Other minor oxides (%)	1.92	3.85	2.62
Loss on ignition (%)	2.04	1.72	0.42
Specific gravity	3.14	2.71	2.89
D10 (μm)	2.17	2.55	2.26
D50 (μm)	8.12	14.09	8.63
D90 (μm)	22.06	71.11	24.43
SSA_{PSD} (m^2/cm^3)	2.25	1.33	1.61
N_{PSD} (#/100 μm^3)	739	193	242

Figure 4.4 shows the PSDs of the cementitious materials, which were measured using a Bettersizer S3 Plus laser particle size and shape analyzer. Assuming spherical particles, the measured PSDs were used to compute (Navarrete et al. 2020) the specific surface area (SSA_{PSD}) and particle number density per unit volume (N_{PSD}). These properties, in addition to the D10, D50 and D90 parameters for each cementitious material, are presented in Table 4.4.

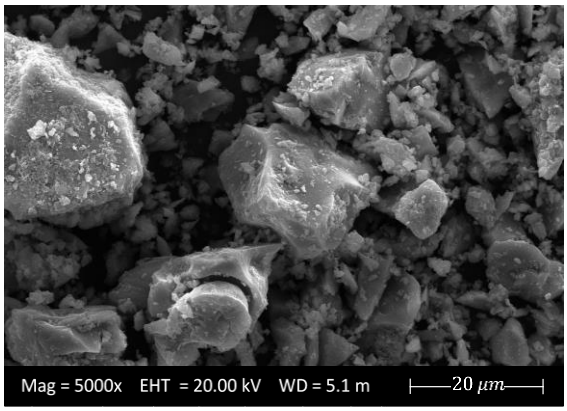

(a) OPC_{ES}

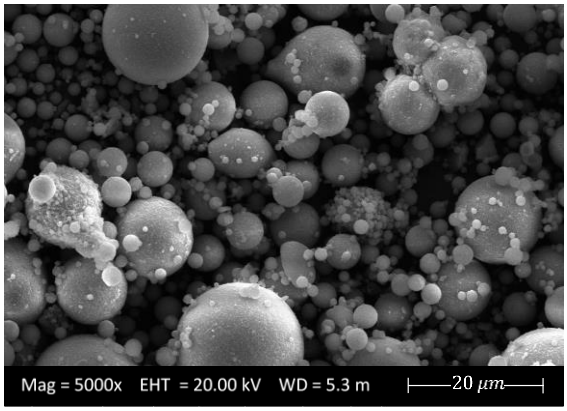

(b) CFA

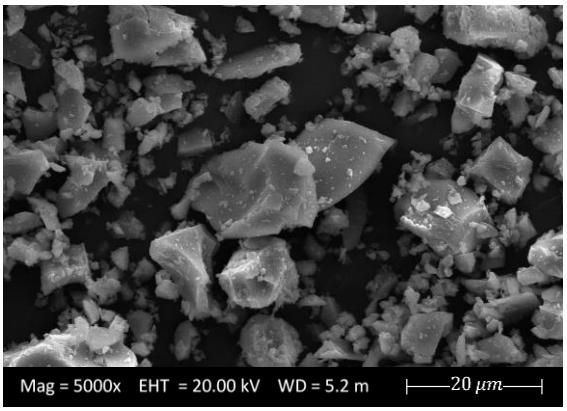

(c) BFS

Figure 4.3: 5,000x SEM images of cementitious materials.

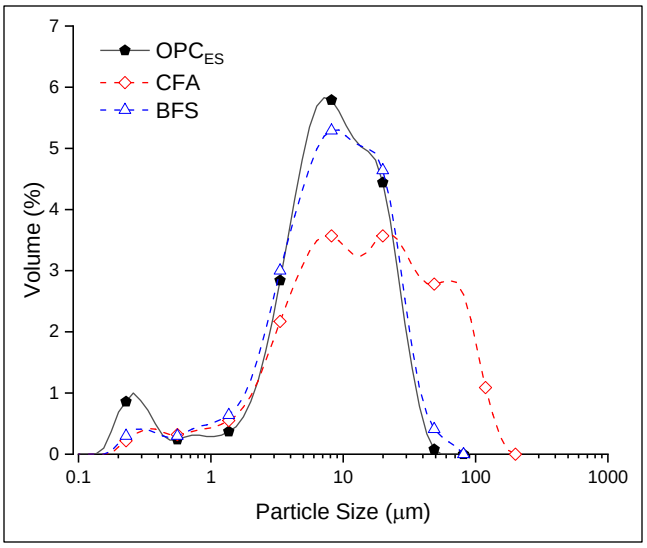

Figure 4.4: Particle size distribution of cementitious materials.

4.3.4 Characterization of cementitious paste, mortar, and concrete workability

The mortar mixture designs were obtained by removing the coarse aggregate from the SCC, while the cementitious pastes were obtained by removing the fine aggregate from the mortars, as shown in Figure 4.4. The measurements for the structural build-up of these materials, as well as the workability of the SCC are described below.

4.3.4.1 Structural build-up measurements of cementitious paste

A_{thix} measurements of the cementitious paste were made with a parallel plate rheometer (TA Discovery Hybrid Rheometer 2). A smooth stationary base plate and a

cross-hatched superior plate with a diameter of 25 mm were used. The gap between the plates was fixed at 1000 μm, as shown to be adequate by previous researchers (Ferraris et al. 2001b; a; Navarrete et al. 2020), to compare the different cementitious pastes. Each sample was protected from excess evaporation using a chamber with an absorbent sponge soaked with water around it (Navarrete et al. 2020; Sant et al. 2008). At 13 min after the addition of water, the cementitious paste was pre-sheared for 60 s. At 15 min, the static yield stress, τ_0^s was measured and the measurements were repeated every 15 min until 75 min to determine the A_{thix} of each cementitious paste. More information on the test protocol can be found in a previous chapter by the authors (Navarrete et al. 2020).

4.3.4.2 Structural build-up measurements of mortar

The growth of τ_0^s for mortar (i.e., A_{thix}^{m}) can be evaluated using rheometric measurements as described above for the cement paste, or by standard workability tests (Bouvet et al. 2010b; Khayat et al. 2012; Megid and Khayat 2019). In this research, the A_{thix}^{m} of mortar was characterized through the change in slump flow of undisturbed samples with time of rest ($R_{s,flow}$). This method was preferred as a workability test commonly used in the field, instead of rheological testing methods.

The mortar slump flow tests were performed using a mini slump cone, at ½ length scale of the standard slump cone (ASTM C1611/C1611M - 18). The initial slump flow (S.flow0) was measured 15 min after the contact of cement and water (i.e., 0 min of rest). The test was repeated after 30 and 60 min of rest (45 and 75 min of age), and the results were used to determine the filling ability index of each mortar mixture (FAI_m) based on Eq. (4-1). Previous researchers (Megid and Khayat 2017, 2019) have shown that the layer-to-layer bond strength is strongly correlated with the filling ability index of SCC.

$$FAI_m = S.flow_0 * R_{s,flow} \quad (4\text{-}1)$$

4.3.4.3 Workability measurements of SCC

The initial workability of each SCC mixture was characterized using common field workability tests so as to establish their characteristics within the ranges of workability reported in the literature. The standard slump flow test (ASTM C1611/C1611M - 18) was used to characterize the filling ability, the slump flow time, T50 (ASTM C1611/C1611M - 18) and v-funnel time (EN12350-9) were measured to estimate the viscosity, and the J-ring flow (ASTM C1621/C1621M - 17) was measured to quantify the passing ability. All these measurements were performed 15 min (0 min of rest) after the initial contact of cement and water.

4.3.5 Layer-to-layer bond strength measurements of multi-layer SCC

Two methods were used to characterize the effects of the experimental factors on the layer-to-layer bond strength between two successive layers of SCC: 1) direct shear strength; and 2) flexural strength. The specimen dimensions, casting, test set-up, and procedure for direct shear strength and flexural strength tests are shown in Figure 4.5 and 4.6, respectively, based on Megid and Khayat (Megid and Khayat 2017, 2019) and ASTM C78/C78M - 18.

The flexural strength was determined from four-point bending tests using the following equation:

$$\sigma_F(DT) = \frac{PL}{bd^2} \tag{4-2}$$

where, $\sigma_F(DT)$ is the flexural strength in MPa at a specific DT, P is the failure load in N, b and d are the width and height of the sample in m, and L is the loading span in m.

In both testing methods, three specimens were cast for each experimental run and delay time, DT. The DT between the first and second layers was set to 30 and 60 min to measure the residual shear and flexural bond strengths at different DTs. The second layer consisted of SCC without any rest. The free fall height, H_{FF} between the top of the first

layer and the release point of the second layer SCC was varied between 200 and 400 mm. Another three specimens per testing condition were cast monolithically (i.e., single layer casting) to provide reference control samples for the residual shear and flexural bond strengths, RB_{DSh} and RB_{F}, respectively. The reduction in these residual bond strengths with time was used to determine the critical delay time, DT_c of each experimental run.

All of the specimens were demolded at the age of 1 day, wrapped in plastic sheeting to prevent moisture loss, and stored for 28 days prior to the direct shear and flexural tests. In each test, the load was continuously applied at a loading rate of 0.15 MPa/s without shock until failure using a hydraulically operated testing machine.

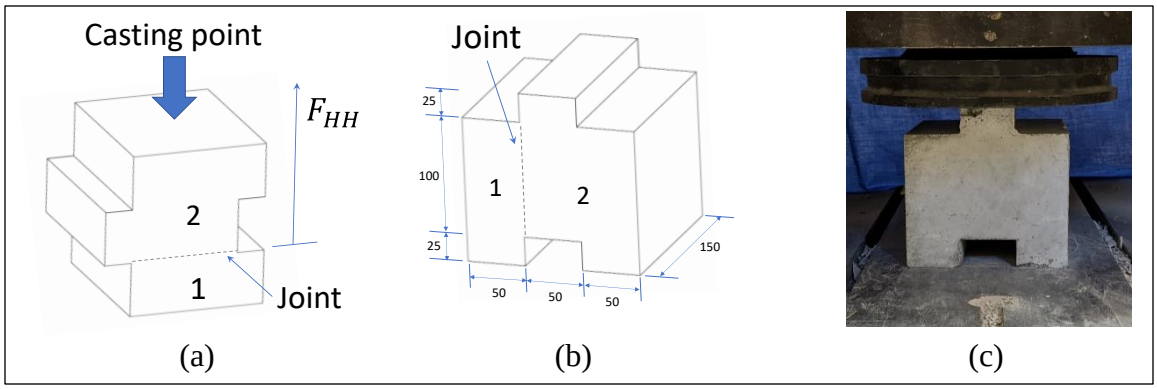

Figure 4.5: Casting (a), sample dimensions in mm (b), and testing set up (c) of the direct shear strength test. Note: Numbers 1 and 2 represent the two layers used during the casting of the specimens.

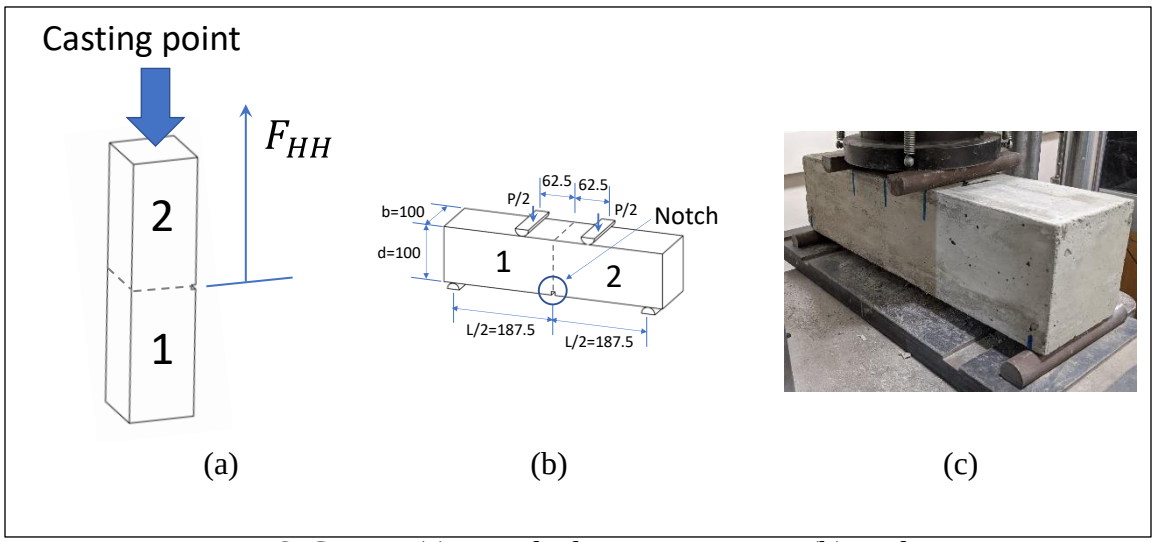

Figure 4.6: Casting (a), sample dimensions in mm (b), and testing set up (c) of the flexural strength test. Note: Numbers 1 and 2 represent the two layers used during the casting of the specimens.

4.4 Results and discussion

4.4.1 Fresh properties of SCC

Table 4.5 summarizes the common field initial workability test results for the Series I and Series II SCC mixtures immediately after mixing. The slump flow ranged between 660 and 810 mm, which is within the range of initial slump flow to achieve the required filling ability of SCC (ACI Committee 238 2008; EFNARC 2005). According to European guidelines (EFNARC 2005), SCC mixtures with a slump flow in this range are suitable for many normal construction applications, such as walls and columns.

The slump flow time, T50 of all the mixtures ranged between 1.2 and 2.0 s. In addition, the v-funnel time ranged between 4.2 and 7.0 s. Considering these results and the European guidelines for SCC (EFNARC 2005), the tested mixtures would provide good filling ability even when used in the construction of structural members with congested reinforcement.

The difference between the slump flow and J-ring flow of each mixture was below 50 mm, with most of the differences below 25 mm. According to ASTM C1621/C1621M-17, these results indicate that minimal or no visible blocking of the mixture would occur, again demonstrating that the tested materials have good passing ability.

Table 4.5: Workability properties of SCC mixtures at 0 min of resting time

	Mix Design Code	Slump flow (mm)	J-ring flow (mm)	T_{50} (s)	V-funnel time (s)
Series I	SCC-100OPC_{ES}/0CFA - 33.6%	660	655	1.6	5.8
	SCC-100OPC_{ES}/0CFA - 35.2%	760	790	1.8	5.7
	SCC-100OPC_{ES}/0CFA - 37.0%	790	795	2.0	7.0
	SCC-85OPC_{ES}/15CFA - 33.6%	690	700	1.8	4.7
	SCC-85OPC_{ES}/15CFA - 35.2%	750	720	1.2	4.3
	SCC-85OPC_{ES}/15CFA - 37.0%	810	800	1.2	4.2
	SCC-70OPC_{ES}/30CFA - 33.6%	660	640	1.4	6.2
	SCC-70OPC_{ES}/30CFA - 35.2%	750	740	1.2	4.4
	SCC-70OPC_{ES}/30CFA - 37.0%	800	770	1.4	4.1
Series II	SCC-85OPC_{ES}/15BFS - 35.2%	660	650	1.2	4.6
	SCC-70OPC_{ES}/30BFS - 35.2%	750	770	1.2	4.5
	SCC-70OPC_{ES}/30BFS - 34.4%	700	700	1.6	5.2

4.4.2 Structural build-up of cement paste and mortar

Figure 4.7 shows the τ_0^s measurements for the cementitious pastes (CPs) at different resting times. All of the CPs presented a similar nonlinear trend, defined by a stage of near-linear increase of τ_0^s, followed by a stage of accelerated increase of τ_0^s. This trend has been observed by previous researchers as well (Bentz et al. 2017; Lecompte and Perrot 2017; Navarrete et al. 2020; Yuan et al. 2017, 2018). Navarrete et al. (Navarrete et al. 2020) proposed a bi-linear relationship to approximate this trend. This method was used to determine the Athix for the initial linear stage and for the following accelerated stage of τ_0^s

(i.e., A^1_{thix} and A^2_{thix}, respectively). The resulting A^1_{thix} and A^2_{thix} for each CP are listed in Table 4.6.

Table 4.6 shows that the replacement of OPC_{ES} by SCMs produces a significant change in the Athix of both stages. Specifically, the replacement of OPC_{ES} by CFA in the Series I mixtures resulted in reductions of A^1_{thix} and A^2_{thix} by up to 34 and 60%, respectively. Similarly, the use of BFS in the Series II mixtures produced reductions of 54% and 22% in A^1_{thix} and A^2_{thix}, respectively. The negative (i.e., decreasing) effect of SCM replacement on Athix can be explained by the smaller N_{PSD} of CFA and BFS with respect to the N_{PSD} of OPC_{ES} (Mostafa and Yahia 2017; Navarrete et al. 2020).

Figure 4.8 shows the reduction in mini slump flow with time of the Series I and Series II mortar mixtures, where a linear trend can be seen for each mortar mixture. The slope of this trend line was used to calculate $R_{s,flow}$ as an indirect measurement of A^m_{thix}.

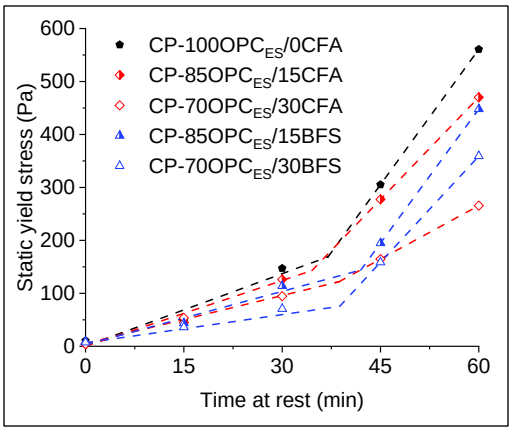

Figure 4.7: Growth of static yield stress of cementitious pastes with time. Discontinuous lines represent the best linear fits for the initial near-linear stage of τ_0^s and for the subsequent accelerated stage of τ_0^s.

Table 4.6: Structural build-up A_{thix}^1 and A_{thix}^2 of cementitious pastes.

	Mix code	A_{thix}^1 (Pa/min)	A_{thix}^2 (Pa/min)
Series I	CP-100OPC$_{ES}$/0CFA	4.56	17.04
	CP-85OPC$_{ES}$/15CFA	4.07	12.84
	CP-70OPC$_{ES}$/30CFA	3.01	6.75
Series II	CP-85OPC$_{ES}$/15BFS	3.51	16.87
	CP-70OPC$_{ES}$/30BFS	2.11	13.37

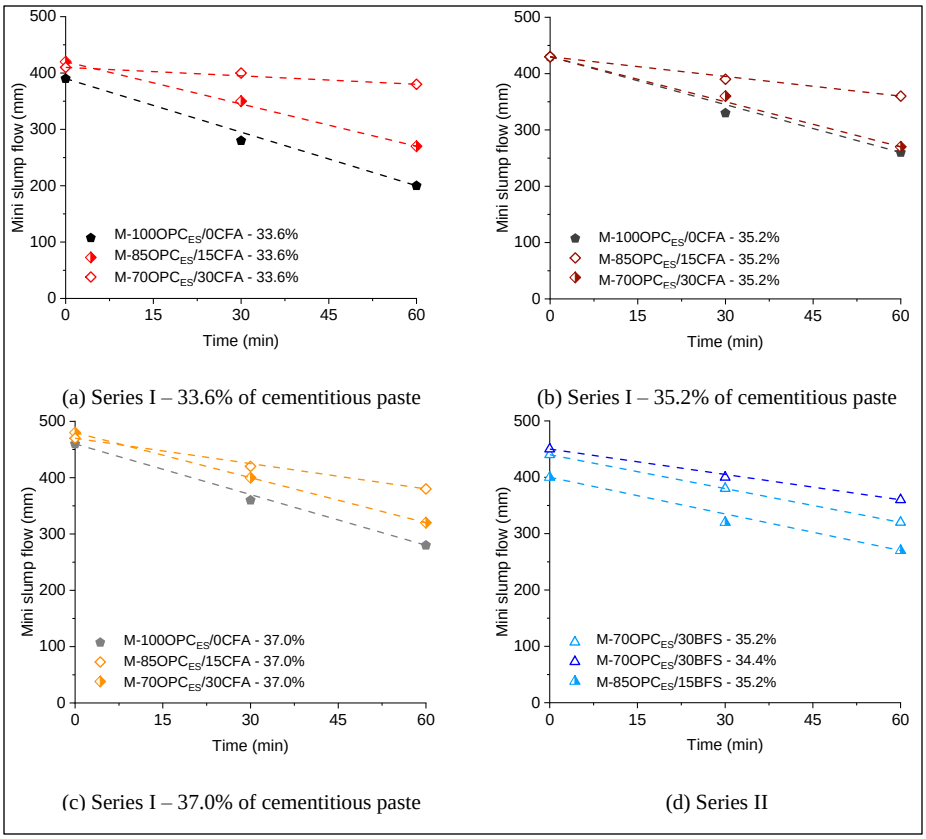

Figure 4.8: Reduction of mortar mini slump flow with time. Dash lines represent linear fit of the results for each experimental run.

Table 4.7 summarizes the initial mini slump flow (i.e., $S.\,flow_0$) and the $R_{s,flow}$ results of each mortar mixture. The FAI_m parameter of each mixture, calculated using Eq. (4-1) with these $S.\,flow_0$ and $R_{s,flow}$ values, are also listed in Table 4.7.

Table 4.7: Slump flow, $S.flow_0$, change in slump flow with time of rest $R_{s,flow}$ and filing ability index FAI_m of mortar mixtures.

	Mix Design Code	$S.flow_0$ (mm)	$R_{s,flow}$ (mm/min)	FAI_m (mm^2/min)
Series I	M-100OPC_{ES}/0CFA - 33.6%	390	3.16	1232.4
	M-100OPC_{ES}/0CFA - 35.2%	430	2.83	1216.9
	M-100OPC_{ES} /0CFA - 37.0%	460	3.00	1380.0
	M-85OPC_{ES}/15CFA - 33.6%	420	2.50	1050.0
	M-85OPC_{ES}/15CFA - 35.2%	430	2.67	1148.1
	M-85OPC_{ES}/15CFA - 37.0%	480	2.66	1276.8
	M-70OPC_{ES} /30CFA - 33.6%	410	0.50	205.0
	M-70OPC_{ES}/30CFA - 35.2%	430	1.16	498.8
	M-70OPC_{ES}/30CFA - 37.0%	470	1.50	705.0
Series II	M-85OPC_{ES}/15BFS - 35.2%	400	2.17	868.0
	M-70OPC_{ES}/30BFS - 35.2%	440	2.00	880.0
	M-70OPC_{ES}/30BFS - 34.4%	450	1.50	675.0

The mixtures with a larger $CP_{\%vol}$ presented a larger $S.flow_0$ and a larger $R_{s,flow}$ in all of the cases, except for the mixtures with no SCMs (i.e., 100OPC_{ES}/0CFA). In addition, the use of CPs with smaller Athix (i.e., mixtures with SCMs) resulted in smaller $R_{s,flow}$. As such, changing the $CP_{\%vol}$ and Athix of CP, it was possible to obtain a wide range of FAI_m, between 205.0 and 1380 mm^2/min. In addition, the mortar mixtures with larger $CP_{\%vol}$ and/or produced with CPs with larger Athix had larger FAI_m.

4.4.3 Residual bond strength of SCC

Figure 4.9 and Figure 4.10 show the residual shear and flexural bond strengths, RB_{DSh} and RB_F, respectively, of the Series I and Series II layered SCC mixtures measured

at delay times of 30 and 60 min. The results have been normalized with respect to the measured shear strength and flexural strength of the monolithic control specimens, $\sigma_{DSh}(0)$ and $\sigma_F(0)$, respectively, listed in Table 4.8. Reductions of up to 37% with increasing delay time can be seen in RB_{DSh}, while the RB_F results had smaller reductions of up to 21%. Therefore, the delay time had a greater effect on the inter-layer residual strength from the direct shear test than the flexural test.

Through second order polynomial regression (SOPR) models, it was found that 84% and 70% of the observed variability in RB_{DSh} and RB_F, respectively, can be explained with the mixture design (i.e., FAI_m and $CP_{\%vol}$) and casting process (i.e., H_{FF} and DT) parameters. Figure 4.11 shows the standardized coefficient of each parameter, which indicates the number of standard deviations the dependent variables (i.e. RB_{DSh} and RB_F) will change per standard deviation increase in the independent variables (Verdugo et al. 2005). These standardized coefficients are used below to evaluate the relative effects of the independent variables on the dependent variables.

Table 4.8: Shear strength $\sigma_{DSh}(0)$ and flexural strength $\sigma_F(0)$ of the monolithic control specimens in the SCC mixtures.

	Mix Design Code	$\sigma_{DSh}(0)$ (MPa)	$\sigma_F(0)$ (MPa)
Series I	SCC-100OPC$_{ES}$/0CFA - 33.6%	14.2	4.6
	SCC-100OPC$_{ES}$/0CFA - 35.2%	14.8	4.7
	SCC-100OPC$_{ES}$/0CFA - 37.0%	12.4	5.1
	SCC-85OPC$_{ES}$/15CFA - 33.6%	10.2	4.9
	SCC-85OPC$_{ES}$/15CFA - 35.2%	12.5	4.7
	SCC-85OPC$_{ES}$/15CFA - 37.0%	12.6	4.6
	SCC-70OPC$_{ES}$/30CFA - 33.6%	11.7	4.5
	SCC-70OPC$_{ES}$/30CFA - 35.2%	10.4	4.5
	SCC-70OPC$_{ES}$/30CFA - 37.0%	9.7	4.4
Series II	SCC-85OPC$_{ES}$/15BFS - 35.2%	14.3	4.4
	SCC-70OPC$_{ES}$/30BFS - 35.2%	10.5	4.5
	SCC-70OPC$_{ES}$/30BFS - 34.4%	10.9	4.1

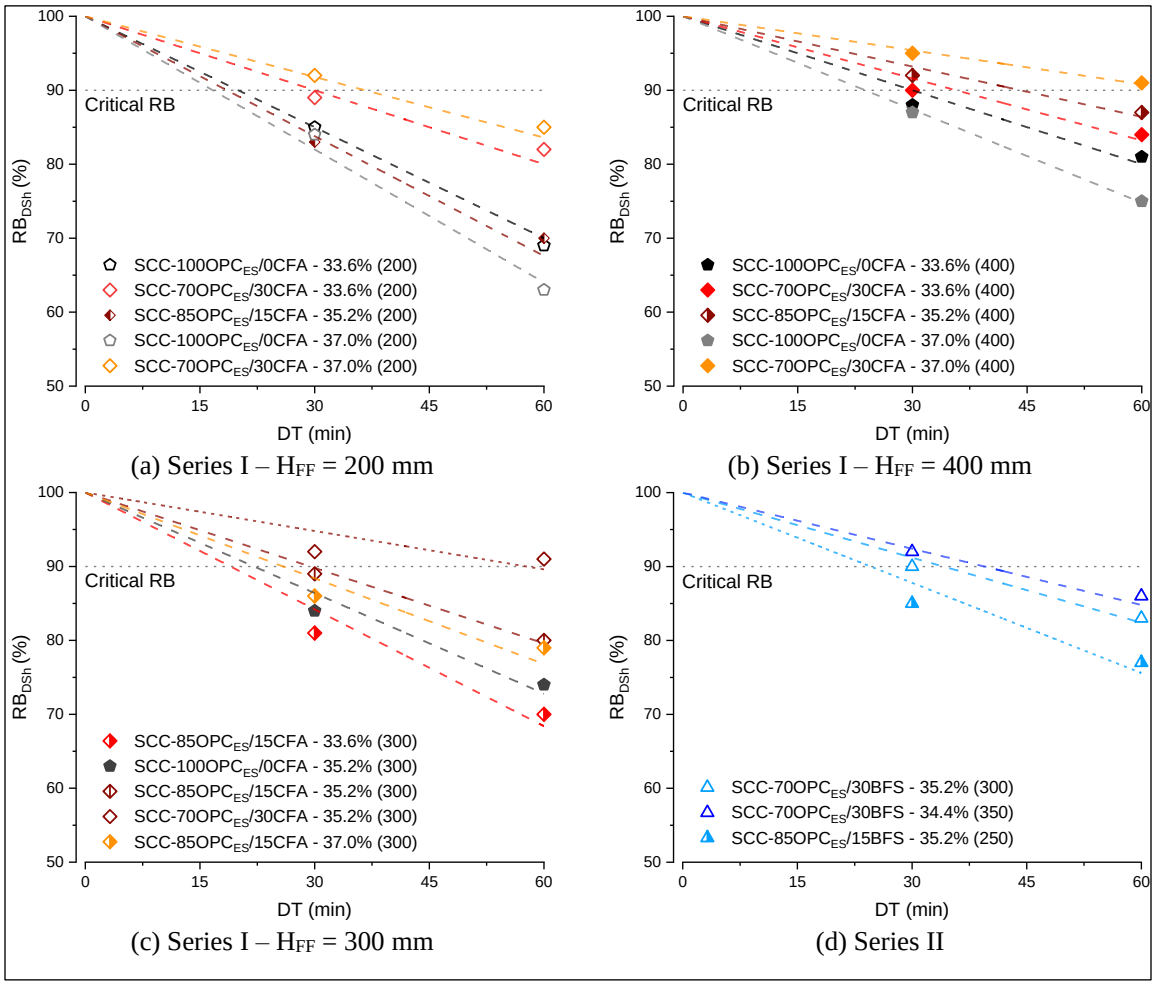

Figure 4.9: Residual shear bond strength, RB_{DSh}, of Series I and Series II SCC mixtures. Dash lines represent the best linear fit for each experimental run.

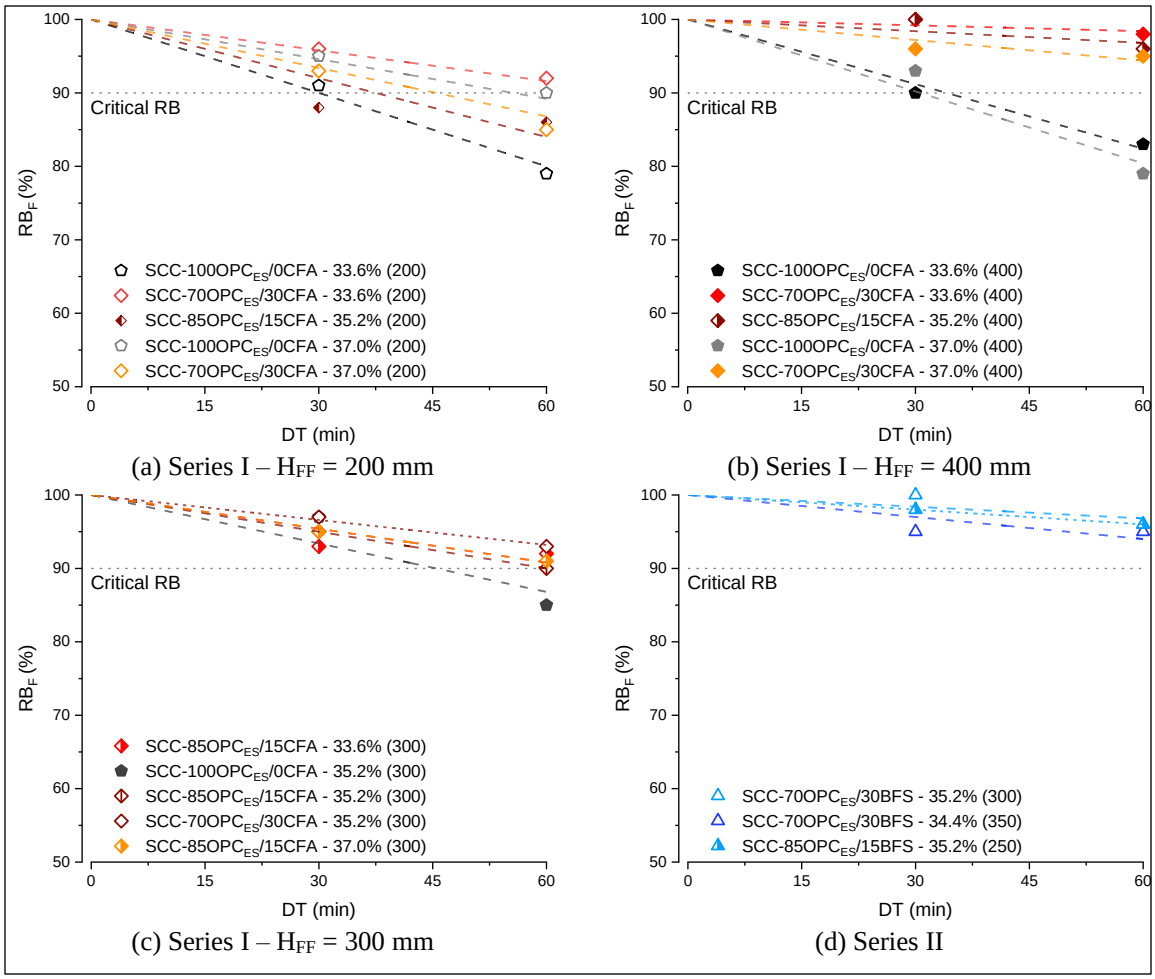

Figure 4.10: RB_F of Series I and Series II SCC mixtures. Dash lines represent the best linear fit for each experimental run.

Looking at the results for FAI_m, the standardized coefficients indicate negative effects on the residual shear and flexural bond strengths, which means that SCCs produced with mortars with larger A_{thix}^{m} are prone to larger bond strength reductions. This is expected, because mixtures with larger FAI_m present larger increase of τ_0^s with time, thus resulting in higher reductions in the intermixing of successive layers with time. In addition,

FAI_m was found to be the most significant parameter for both residual bond strengths, with a greater effect on the flexural strength, RB_F than on the shear strength, RB_{DSh}.

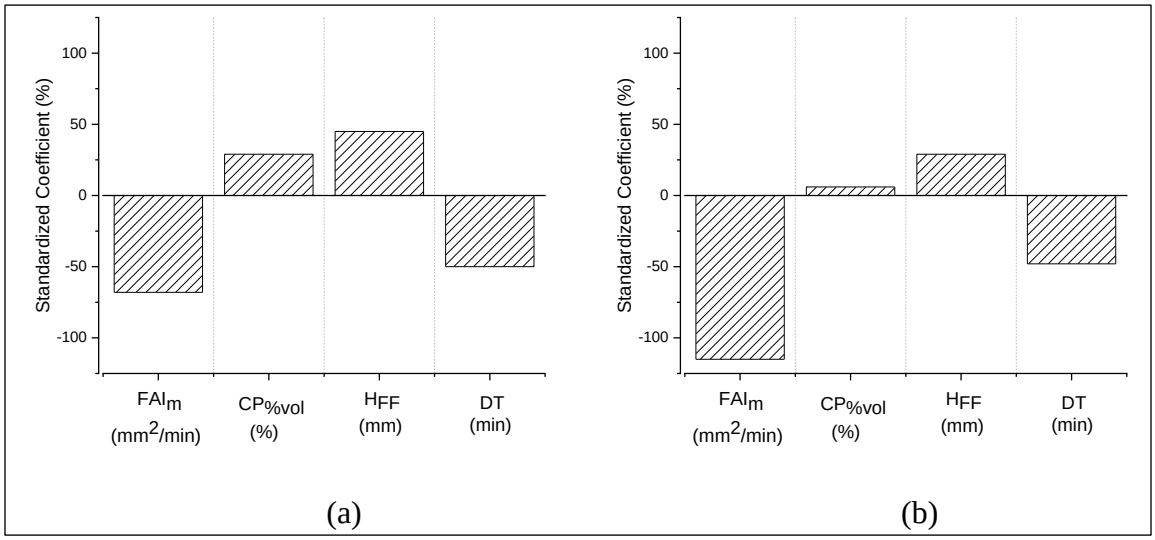

Figure 4.11: Standardized coefficients for the effect of studied factors on RB_{DSh} (a) and RB_F (b).

Among the parameters studied, $CP_{\%vol}$ presented the lowest effects on the residual shear and flexural bond strengths, with a less significant effect on RB_F than on RB_{DSh}. Overall, an increase in $CP_{\%vol}$ produced positive (i.e., increasing) effects on both residual bond strengths. Note that increased $CP_{\%vol}$ has two opposing trends on the residual bond strength as follows: 1) a positive trend from increased intermixing of successive SCC layers (due to a reduction in the initial τ_0^s); and 2) a negative trend from decreased aggregate interlock and surface roughness of the first layer. As such, the overall positive standardized coefficients for $CP_{\%vol}$ indicate that the former trend is more prominent than the latter trend.

Increases in H_{FF} also resulted in increases in both residual bond strengths. This is expected, because an increase in H_{FF} increases the interlock resulting from the penetration of the top SCC layer into the lower layer (Megid and Khayat 2019). The effect of H_{FF} was more significant on RB_{DSh} than on RB_F.

In comparison, increases in DT resulted in decreases in both residual bond strengths, with similar effects in both cases. This was also expected, because an increase in DT increases the τ_0^s, thus reducing the intermixing of the successive SCC layers.

Overall, the tested mixture design and casting process parameters had greater effects on RB_{DSh} than on RB_F. Therefore, it is concluded that RB_{DSh} is a better measure to control the mixture design and casting process for inter-layer bond strength, as investigated further in the analysis of the RB_{DSh} results below.

The SOPR model for RB_{DSh} was developed using FAI_m, $CP_{\%vol}$, H_{FF}, and DT as the independent parameters. The resulting model is presented in Eq. (4-3), with summary and coefficients (i.e., $\alpha_0..\alpha_5$) of the terms given in Table 4.9.

$$RB_{DSh} = \alpha_0 + \alpha_1 FAI_m + \alpha_2 CP_{\%vol} + \alpha_3(FAI_m \cdot DT) + \alpha_4(FAI_m \cdot CP_{\%vol}) + \alpha_5(FAI_m \cdot H_{FF}) \quad (4\text{-}3)$$

Table 4.9: SOPR model coefficients for RB_{DSh}

	Coefficient	Standard error	T-statistic	P-value	95% C.I. ($\pm$)
α_0	- 8.56 x 10^{1}	4.33 x 10^{1}	- 2.12	0.045	8.34 x 10^{-3}
α_1	+ 1.11 x 10^{-1}	3.90 x 10^{-2}	+ 2.85	0.009	8.00 x 10^{0}
α_2	+ 5.18 x 10^{3}	1.17 x 10^{2}	+ 4.40	0.000	2.44 x 10^{0}
α_3	- 2.64 x 10^{-4}	3.88 x 10^{-5}	- 6.83	0.000	8.02 x 10^{-5}
α_4	- 3.56 x 10^{-1}	1.12 x 10^{-1}	- 3.19	0.004	2.31 x 10^{-1}
α_5	+ 4.35 x 10^{-5}	7.35 x 10^{-6}	+ 5.92	0.000	1.52 x 10^{-5}

Figure 4.12 presents comparisons between the experimental measurements and the results predicted with the SOPR model. It can be seen that the deviations between the experimental and predicted results for the Series II runs are smaller than the confidence interval of the SOPR model, thus validating this model.

According to Eq. (4-3), the interaction between FAI_m and DT has a negative effect on RB_{DSh}, which means that SCCs with larger FAI_m are more greatly affected by DT. This is expected, because mixtures with larger FAI_m develop greater increases of τ_0^s with DT, which results in greater reductions in the intermixing of successive layers with DT. In addition, Eq. (4-3) shows that the interaction between FAI_m and H_{FF} presents a positive effect on RB_{DSh}, which means that SCCs with larger FAI_m are more affected by H_{FF}. This can be explained because mixtures with lower FAI_m show lower increases of τ_0^s and, therefore, the H_{FF} required to produce adequate penetration of the top concrete layer into the lower layer is smaller, reducing the effect of H_{FF} on RB_{DSh}.

Considering the interactions between FAI_m and the casting process parameters (i.e., H_{FF} and DT), it can be concluded that mixtures with lower FAI_m are less affected by the casting process. Therefore, the use of SCC mixtures with lower A_{thix} can reduce effects of common field issues, such as delivery delays, on the residual bond strength in multi-layer casting.

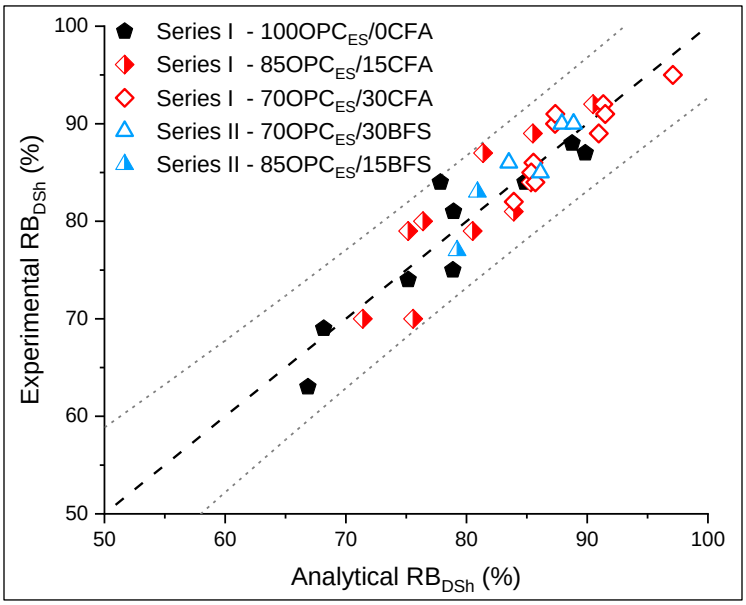

Figure 4.12: Relationship between experimental and analytical RB_{DSh} results. Gray discontinuous lines represent the 95% confidence interval limits of the model. Black (thicker) discontinuous line represents perfect correlation between the experimental and analytical results.

Eq. (4-3) also shows that the interaction between FAI_m and $CP_{\%vol}$ has a negative effect on RB_{DSh}. This can be expected because SCC mixtures with larger $CP_{\%vol}$ have larger mortar volume fractions, thus increasing the negative effect of FAI_m on RB_{DSh}.

The validated SOPR model given by Eq. (4-3) was used to map the combined effects of the mixture design parameters on RB_{DSh}, for two combinations of DT and H_{FF}. These response surfaces allow for a better understanding of the interactions of the mixture design parameters. Figure 13.a presents the results for a scenario were the casting process parameters reduce RB_{DSh}, which means a long DT (i.e., 60 min) and low H_{FF} (i.e., 200 mm). In contrast, Figure 13.b presents a scenario were the casting process parameters increase RB_{DSh}, which means a short DT (i.e., 30 min) and large H_{FF} (i.e., 400 mm).

The results suggest that for the case with the more critical construction conditions (i.e., long DT and low H_{FF} in Figure 13.a) for RB_{DSh}, the combined effect of the mixture design parameters is more significant, since the relative distances between the iso-response curves in Figure 13.a are smaller than those in Figure 13.b. In addition, in the more critical scenario of Figure 13.a, FAI_m has a larger effect than $CP_{\%vol}$ for all the combinations studied, since the slope of all the iso-response curves are over 45 degrees to the horizontal axis. In the less critical scenario of Figure 13.b, the effect of $CP_{\%vol}$ relative to the effect of FAI_m is more significant for lower values of FAI_m, and less significant for higher values of FAI_m.

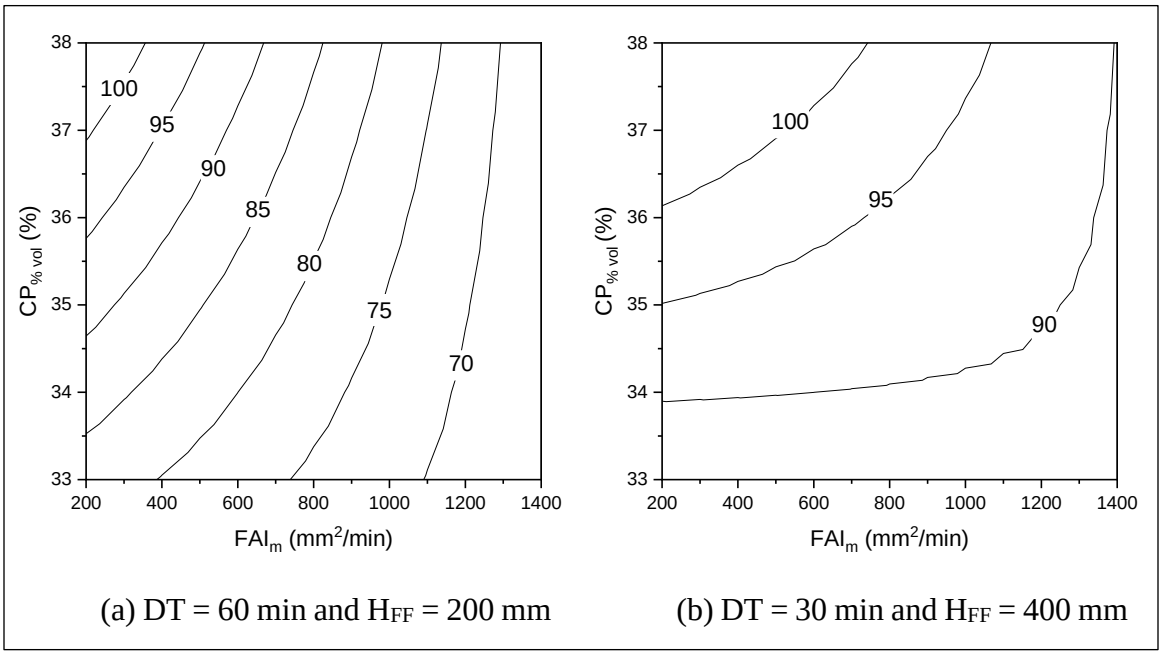

Figure 4.13: Effect of mixture design parameters on RB_{DSh}, as estimated with the SOPR model, for two different DT and H_{FF} combinations.

RB_{DSh} values estimated with the SOPR model for different combinations of casting process parameters are analyzed next. Specifically, Figure 14.a shows the results for a mixture design that produces a more negative effect on RB_{DSh} (i.e., low $CP_{\%vol}$ and high FAI_m), while Figure 14.b shows the results for a mixture design with a more positive effect on RB_{DSh} (i.e., high $CP_{\%vol}$ and low FAI_m).

The results suggest that in the case of mixture designs with a more negative effect on RB_{DSh}, the combined effect of the casting process parameters is more significant, since the relative distances between the iso-response curves in Figure 14.a are smaller than those in Figure 14.b. In addition, H_{FF} has a larger effect than DT for all of the combinations

studied and both mixture designs evaluated, since the slopes of all of the iso-response curves are below 45 degrees to the horizontal axis.

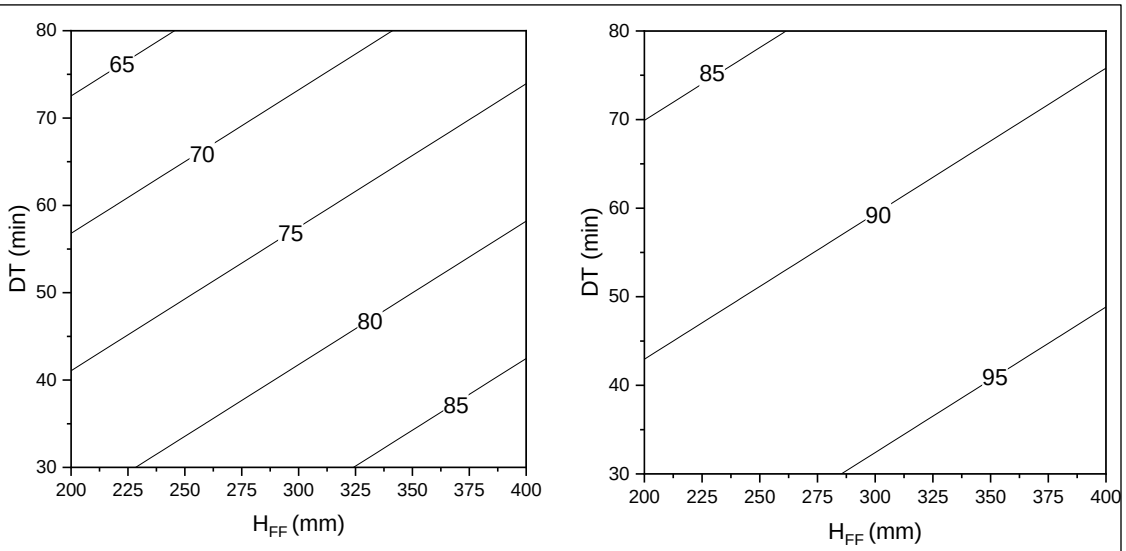

(a) $CP_{\%vol}$ = 33.6% and FAI_m = 1200 mm^2/min

(b) $CP_{\%vol}$ = 37.0% and FAI_m = 700 mm^2/min

Figure 4.14: Effect of casting process on RBDSh, as estimated with the SORP model, for two different FAI_m and $CP_{\%vol}$ combinations.

4.4.4 Critical delay time analysis of SCC

Table 4.10 shows the critical time, DT_c for each mixture, defined as the maximum time that allows 90% residual bond strength, calculated using the linear fit of the RB_{DSh} and RB_F results in Figure 4.9 and Figure 4.10, respectively. In all of the mixtures, the DT_c

calculated using the RB_{DSh} results were smaller than the DT_c calculated using the RB_F results. Therefore, DT_c is governed by the residual bond strength measured with the direct shear test.

Table 4.10: DT_c from direct shear strength (RB_{DSh}) and flexural strength (RB_F) results.

			DT_c (min)	
	Mixture Design ID	H_{FF} (mm)	RB_{DSh}	RB_F
Series I	SCC-70OPC_{ES}/30CFA - 33.6%	200	20.0	29.41
	SCC-100OPC_{ES}/0CFA - 33.6%	200	30.3	71.43
	SCC-70OPC_{ES}/30CFA - 37.0%	200	16.7	55.56
	SCC-100OPC_{ES}/0CFA - 37.0%	200	37.0	45.45
	SCC-70OPC_{ES}/30CFA - 33.6%	400	30.3	34.09
	SCC-100OPC_{ES}/0CFA - 33.6%	400	35.7	333.33
	SCC-70OPC_{ES}/30CFA - 37.0%	400	23.8	31.25
	SCC-100OPC_{ES}/0CFA - 37.0%	400	66.7	107.53
	SCC-70OPC_{ES}/30CFA - 35.2%	300	22.2	45.45
	SCC-100OPC_{ES}/0CFA - 35.2%	300	58.8	90.91
	SCC-85OPC_{ES}/15CFA - 33.6%	300	19.0	65.23
	SCC-85OPC_{ES}/15CFA - 37.0%	300	25.8	25.64
	SCC-85OPC_{ES}/15CFA - 35.2%	200	18.5	37.50
	SCC-85OPC_{ES}/15CFA - 35.2%	400	44.1	187.62
	SCC-85OPC_{ES}/15CFA - 35.2%	300	29.4	59.99
Series II	SCC-85OPC_{ES}/15BFS - 35.2%	350	24.6	149.93
	SCC-70OPC_{ES}/30BFS - 35.2%	250	34.1	149.93
	SCC-70OPC_{ES}/30BFS - 34.4%	300	39.5	120.05

A SOPR model was developed to analyze the effect of the free fall height, H_{FF}, cement paste volume, $CP_{\%vol}$, and filling ability index, FAI_m on DT_c. The resulting model

is presented in Eq. (4-4), with a summary and coefficients (i.e., $\beta_0, .., \beta_4$) of all the terms given in Table 4.11.

$$DT_c = \beta_0 + \beta_1 FAI_m + \beta_2 CP_{\%vol} + \beta_3 (FAI_m \cdot CP_{\%vol}) + \beta_4 (CP_{\%vol} \cdot H_{FF}) \quad (4\text{-}4)$$

Table 4.11: SOPR model coefficients for DT_c

	Coefficient	Standard error	T-statistic	P-value	95% C.I. ($\pm$)
β_0	- 5.12 x 10^2	1.18 x 10^2	- 4.33	0.001	- 2.50 x 10^2
β_1	+ 4.03 x 10^{-1}	1.11 x 10^{-1}	+ 3.63	0.005	+ 6.51 x 10^{-1}
β_2	+ 1.58 x 10^3	3.45 x 10^2	+ 4.58	0.001	+ 2.35 x 10^3
β_3	- 1.24 x 10^0	3.23 x 10^{-1}	- 3.85	0.003	- 5.23 x 10^{-1}
β_4	+ 2.26 x 10^{-1}	6.00 x 10^{-2}	+ 3.73	0.004	+ 3.60 x 10^{-1}

Comparisons between the experimental measurements and the results estimated using the SOPR model are shown in Figure 4.15. This model explains 85.3% of the observed variability in the Series I results. In addition, the deviations between the experimental and predicted results for the Series II runs are within the confidence interval of the SOPR model, thus validating this model.

The standardized coefficients in Figure 4.16 indicate that out of the three model parameters, FAI_m had the largest effect on DT_c, followed by $CP_{\%vol}$ and H_{FF}, which presented similar effects. Therefore, the DT_c of a SCC mixture is more affected by the mixture design parameters than the H_{FF}.

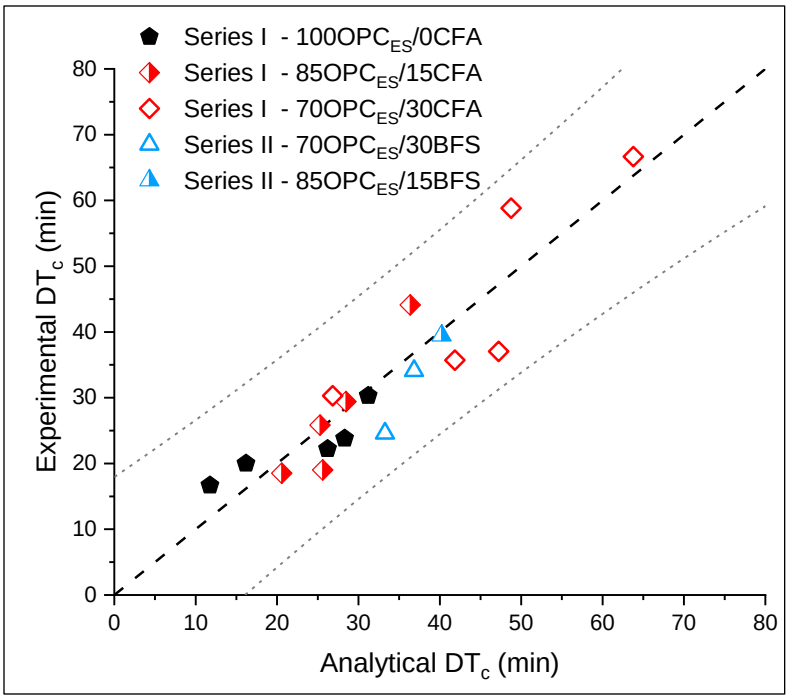

Figure 4.15: Relationship between experimental and analytical DT_c. Gray discontinuous lines represent the 95% confidence interval limits of the model. Black (thicker) discontinuous line represents perfect correlation between the experimental and analytical results.

Figure 4.16 also shows that increases in FAI_m result in decreases in DT_c. This is expected because a larger FAI_m produces a larger rate of decrease for RB_{DSh} with time, due to a faster increase in the τ_0^s of the mortar. In contrast, increases in $CP_{\%vol}$ and H_{FF} lead to increased DT_c. This can be explained since an increase in $CP_{\%vol}$ reduces the τ_0^s of the mortar at different ages, which reduces the rate of decrease for RB_{DSh} with time, thus increasing DT_c. In addition, a higher H_{FF} increases the intermixing of successive layers, which reduces the rate of decrease for RB_{DSh} with time, increasing DT_c.

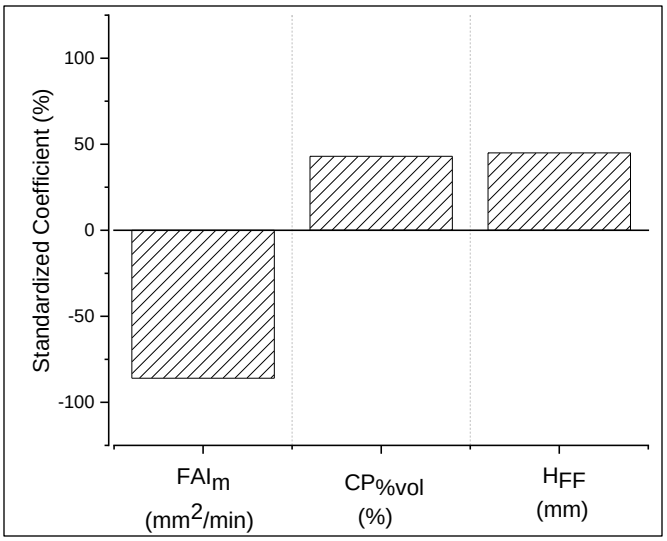

Figure 4.16: Standardized coefficients for FAI_m, cement paste volume, and free fall height of the SOPR model of DT_c.

Eq. (4-4) shows that the interaction between FAI_m and $CP_{\%vol}$ has a negative effect on DT_c, which means that SCC mixtures with larger $CP_{\%vol}$ are more significantly affected by FAI_m. This is because mixtures with larger $CP_{\%vol}$ have larger mortar volumes and, therefore, the rheological behavior of the mortar (i.e., FAI_m) is more significant in the rate of decrease for RB_{DSh}.

In addition, the interaction between H_{FF} and $CP_{\%vol}$ has a positive effect on DT_c. As H_{FF} increases, the intermixing of successive layers also increases and as $CP_{\%vol}$ increases the τ_0^s of the bottom layer decreases. Therefore, combinations of high H_{FF} and high $CP_{\%vol}$ result in higher RB_{DSh} through better intermixing of the successive layers.

4.5 Conclusions

This research investigated the effects of the cementitious paste volume, $CP_{\%vol}$, structural build-up of mortar, A_{thix}^{m}, and their interactions with casting process parameters (i.e., free fall height, H_{FF}, and delay time, DT) on the residual shear and flexural bond strengths of multi-layer SCC. In addition, the effect of cementitious paste volume, structural build-up of mortar, and their interaction with the free fall height on the critical delay time is analyzed. The measured results from a face centered central composite experimental design, composed of 15 mixtures, were used to conduct analysis of variance and develop second order polynomial regression (SOPR) models, which were validated with three additional experimental runs. Important conclusions from this study are listed below:

1. The residual shear and flexural bond strengths of multi-layer SCC (RB_{DSh} and RB_F, respectively) are affected mostly by the structural build-up of mortar. In contrast, the cementitious paste volume is the parameter with the lowest effect on RB_{DSh} and RB_F.
2. An SOPR model to predict RB_{DSh} provided good correlations with the experimental results of self-consolidating concrete (SCC) mixtures with different structural build-up of mortar, cementitious paste volume, free fall height, and delay time.
3. Multi-layer casting of SCC results in a greater reduction in RB_{DSh} than RB_F, negatively affecting the structural performance of SCC structural elements.

4. SCC mixtures with greater cementitious paste volume show lower reductions in RB_{DSh} and RB_F making them more resilient to the casting conditions.
5. SCC mixtures with lower structural build-up of mortar can mitigate the effects of common field issues on RB_{DSh} and RB_F, such as on-site concrete delivery delays.
6. The critical delay time, defined as the maximum time that allows 90% residual bond strength in multi-layer casting of SCC, is governed more by RB_{DSh} than by RB_F.
7. An SOPR model to predict DT_c provided good correlations with the experimental results of SCC mixtures with different structural build-up of mortar, cementitious paste volume, and free fall height.
8. The critical delay time is affected mostly by the structural build-up of mortar, followed by the cementitious paste volume and the free fall height, which have similar effects.

CHAPTER 5: CONCLUSIONS AND FUTURE DIRECTIONS

This chapter repeats (for the convenience of the reader) the conclusions listed at the ends of Chapters 2-4 regarding each specific objective and discusses future directions.

5.1 Conclusions

1. A second order polynomial regression (SOPR) model to predict the structural build up of cementitious paste as a function of supplementary cementitious material (SCM) properties and primary mixture parameters was developed and validated. The model shows good accuracy to predict the structural build up of mixtures prepared with various SCMs, SCM replacement amounts, water to cement ratios, and cement with different reactivities.
2. The effect of particle size of SCM on the structural build up of cementitious paste is governed by the particle density which determines the number of contact points instead of the specific surface area.

3. The effect of physicochemical properties of SCM on the structural build up of cementitious paste is governed by the surface potential instead of the chemical reactivity at early age.
4. The structural build up of cementitious paste is affected mostly by the water to cementitious ratio. In contrast, the replacement level of SCM is the least significant parameter affecting structural build up. Among the SCM properties, the particle density has a greater effect than the surface potential. In addition, reactivity of cement has a similar effect as the particle density of SCM.
5. The structural build up of mixtures with more reactive cement is less affected by the SCM properties. In addition, the structural build up of mixtures with a higher water to cement ratio is less affected by the particle density of SCM and by the level of replacement of SCM.
6. Changes in the particle number density of SCM and water to cement ratio result in slight variations in the nucleation and growth rates of the cement particles. This means that the effects of these parameters on the structural build up of cementitious paste are produced by a reduction in the distance between the particles rather than improved cement hydration.
7. The effect of the particle size on the viscosity of cementitious paste is better explained by the particle number density than by the specific surface area.
8. The SOPR models were able to predict the viscosity of cementitious pastes at different shear rate ranges. The parameters that governed these models are the solid

volume fraction, the interparticle force, and particle number density of the cementitious particles. The models showed good accuracy to estimate the viscosity of mixtures produced with different SCMs, SCM-cement proportions, solid volume fractions, and different cement types.

9. The viscosity of the cementitious paste is more affected by the solid volume fraction, which is determined by the water-to-cementitious materials ratio, than by the properties of the cementitious particles.
10. The interparticle force is a good predictor of the bonding strength of cementitious particles, and the combined effect of particle number density and solid volume fraction is a good estimator of the amount of contact points of this network, which explains most of the observed variability in the viscosity of cementitious paste.
11. The viscosity of cementitious paste is more affected by the number of contact points between the cementitious particles than the interparticle force between them.
12. The interparticle force is governed by the surface roughness of the cementitious materials and the water-to-cementitious materials ratio, which affects the zeta potential of the cementitious paste.
13. The residual shear and flexural bond strengths of multi-layer SCC (RB_{DSh} and RB_{F}, respectively) are affected mostly by the structural build-up of mortar. In contrast, the cementitious paste volume is the parameter with the lowest effect on RB_{DSh} and RB_{F}.

14. An SOPR model to predict RB_{DSh} provided good correlations with the experimental results of self-consolidating concrete (SCC) mixtures with different structural build-up of mortar, cementitious paste volume, free fall height, and delay time.
15. Multi-layer casting of SCC results in a greater reduction in RB_{DSh} than RB_F, negatively affecting the structural performance of SCC structural elements.
16. SCC mixtures with greater cementitious paste volume show lower reductions in RB_{DSh} and RB_F making them more resilient to the casting conditions.
17. SCC mixtures with lower structural build-up of mortar can mitigate the effects of common field issues on RB_{DSh} and RB_F, such as on-site concrete delivery delays.
18. The critical delay time, defined as the maximum time that allows 90% residual bond strength in multi-layer casting of SCC, is governed more by RB_{DSh} than by RB_F.
19. An SOPR model to predict DT_c provided good correlations with the experimental results of SCC mixtures with different structural build-up of mortar, cementitious paste volume, and free fall height.
20. The critical delay time is affected mostly by the structural build-up of mortar, followed by the cementitious paste volume and the free fall height, which have similar effects.

5.2 Future Directions

The main focus of this research is on the use of SCMs to improve the rheology of cementitious paste, and one specific application of the results to multi-layer SCC. Future

work related to this research includes: 1) interactions of chemical admixtures (e.g., water reducers) with SCMs and primary mixture design parameters influencing the rheology of cementitious paste; 2) layer-to-layer residual bond strength in larger-scale and reinforced SCC structures; 3) improvement of the structural-build up of 3D concrete printing through the use of SCMs; 4) residual layer-to-layer bond strength of 3D concrete printing structures; and 5) segregation control of stratified concrete mixtures through the use of SCMs.

BIBLIOGRAPHY

ACI Committee 238. (2008). *Report on Measurements of Workability and Rheology of Fresh Concrete*. Farmington Hills.

Adjoudj, M., Ezziane, K., Hadj, E., Ngo, T., and Kaci, A. (2014). "Evaluation of rheological parameters of mortar containing various amounts of mineral addition with polycarboxylate superplasticizer." *Construction and Building Materials*, Elsevier Ltd, 70, 549–559.

Allen, D. M. (1971). "Mean Square Error of Prediction as a Criterion for Selecting Variables." *Technometrics*, 13(3), 469–475.

Assaad, J. J., and Issa, C. A. (2016). "Preliminary study on interfacial bond strength due to successive casting lifts of self-consolidating concrete – Effect of thixotropy." *Construction and Building Materials*, Elsevier Ltd, 126, 351–360.

Assaad, J. J., and Khayat, K. H. (2006a). "Effect of Mixture Consistency on Formwork Pressure Exerted by Highly Flowable Concrete." *Journal of Materials in Civil Engineering*, 18(6), 786–791.

Assaad, J., and Khayat, K. H. (2004). "Assessment of Thixotropy of Self-Consolidating Concrete and Concrete-Equivalent-Mortar - Effect of Binder Composition and

Content.” *ACI Materials Journal*, 101(5), 400–408.

Assaad, J., and Khayat, K. H. (2006b). “Formwork Pressure of Self-Consolidating Concrete Made with Various Binder Types and Contents.” *ACI Materials Journal*, 23(102), 215–224.

Assaad, J., Khayat, K. H., and Mesbah, H. (2004). “Assessment of Thixotropy of Flowable and Self-Consolidating Concrete.” *ACI Materials Journal*, (100).

ASTM International. (2019). *ASTM C595/C595M-19, Standard Specification for Blended Hydraulic Cements*. West Conshohocken, PA.

ASTM Standard C150/C150M. (2016). “Standard Specification for Portland Cement.” *Annual Book of ASTM Standards*, ASTM International, West Conshohocken, PA.

Balmforth, N. J., Frigaard, I. A., and Ovarlez, G. (2013). “Yielding to Stress: Recent Developments in Viscoplastic Fluid Mechanics.” *Annual Review of Fluid Mechanics*, 46(1), 121–146.

Barnes, J. M., and Johnston, D. W. (2003). “Fresh Concrete Lateral Pressure On Formwork.” *Construction Research Congress*, American Society of Civil Engineers, Reston, VA, 1–8.

Bellotto, M. (2013). “Cement paste prior to setting: A rheological approach.” *Cement and Concrete Research*, Elsevier Ltd, 52, 161–168.

Bendapudi, S., and Saha, P. (2011). “Contribution of fly ash to the properties of mortar and concrete.” *Int J Earth Sci Eng*, 04(06), 1017–1023.

Bentz, D. P., Ferraris, C. F., Galler, M. A., Hansen, A. S., and Guynn, J. M. (2012).

"Influence of particle size distributions on yield stress and viscosity of cement – fl y ash pastes." *Cement and Concrete Research*, Elsevier B.V., 42(2), 404–409.

Bentz, D. P., Ferraris, C. F., Jones, S. Z., Lootens, D., and Zunino, F. (2017). "Limestone and silica powder replacements for cement: Early-age performance." *Cement and Concrete Composites*, Elsevier Ltd, 78, 43–56.

Bentz, D. P., Jones, S. Z., Bentz, I. R., and Peltz, M. A. (2018). "Towards the formulation of robust and sustainable cementitious binders for 3-D additive construction by extrusion." *Construction and Building Materials*, Elsevier Inc., 175, 215–224.

Bentz, D. P., Jones, S. Z., Bentz, I. R., and Peltz, M. A. (2019). *Towards the Formulation of Robust and Sustainable Cementitious Binders for 3D Additive Construction by Extrusion*. *3D Concrete Printing Technology*, Elsevier Inc.

Bingham, E. C. (1922). *Fluidity and plasticity*. McGraw-Hill, New York.

Bouvet, A., Ghorbel, E., and Bennacer, R. (2010a). "The mini-conical slump fl ow test : Analysis and numerical study." *Cement and Concrete Research*, Elsevier Ltd, 40(10), 1517–1523.

Bouvet, A., Ghorbel, E., and Bennacer, R. (2010b). "The mini-conical slump flow test: Analysis and numerical study." *Cement and Concrete Research*, Elsevier Ltd, 40(10), 1517–1523.

Bullard, J. W., Jennings, H. M., Livingston, R. A., Nonat, A., Scherer, G. W., Schweitzer, J. S., Scrivener, K. L., and Thomas, J. J. (2011). "Mechanisms of cement hydration." *Cement and Concrete Research*, Elsevier B.V., 41(12), 1208–1223.

Burgos, D. M., Cardona, L. M., and Delvasto, S. (2014). “Estudio de dos materiales volcánicos y efecto del tipo de molienda en su reactividad.” *Revista Ingenieria de Construccion*, 29(2), 159–174.

Buswell, R. A., Leal de Silva, W. R., Jones, S. Z., and Dirrenberger, J. (2018). “3D printing using concrete extrusion: A roadmap for research.” *Cement and Concrete Research*, Elsevier, 112(October 2017), 37–49.

Chen, J. J., Thomas, J. J., Taylor, H. F. W., and Jennings, H. M. (2004). “Solubility and structure of calcium silicate hydrate.” *Cement and Concrete Research*, 34(9), 1499–1519.

Chen, T. (2020). “Preventing Wall Slip in Rheology Experiments.” *TA Instruments*.

Chen, Y., Figueiredo, S. C., Yalçinkaya, Ç., Çopuroğlu, O., Veer, F., and Schlangen, E. (2019). “The effect of viscosity-modifying admixture on the extrudability of limestone and calcined clay-based cementitious material for extrusion-based 3D concrete printing.” *Materials*, 12(9), 9–12.

Cheng, D. C. H. (1986). “Yield stress: A time-dependent property and how to measure it.” *Rheologica Acta*, 25(5), 542–554.

Chia, K., Kho, C., and Zhang, M. (2005). “Stability of fresh lightweight aggregate concrete under vibration.” *ACI materials journal*, 102(5), 347–354.

Choi, B. Il, Kim, J. H., and Shin, T. Y. (2019). “Rheological model selection and a general model for evaluating the viscosity and microstructure of a highly-concentrated cement suspension.” *Cement and Concrete Research*, Elsevier, 123(May), 105775.

Chong, J. S., Christiansen, E. B., and Baer, A. D. (2018). “Rheology of concentrated suspensions.” *Journal of Applied Polymer Science*, Wiley-Blackwell, 15(8), 2007–2021.

Derjaguin, B., and Landau, L. (1941). “Theory of the stability of strongly charged lyophobic sols and of the adhesion of strongly charged particles in solutions of electrolytes.” *Acta Physicochimica U.R.S.S.*, 14, 633–662.

Dhanya, B. S., Santhanam, M., Gettu, R., and Pillai, R. G. (2018). “Performance evaluation of concretes having different supplementary cementitious material dosages belonging to different strength ranges.” *Construction and Building Materials*, Elsevier Ltd, 187, 984–995.

EFNARC. (2005). *The European Guidelines for Self-Compacting Concrete*. *The European Guidelines for Self Compacting Concrete*.

Elakneswaran, Y., Nawa, T., and Kurumisawa, K. (2009). “Zeta potential study of paste blends with slag.” *Cement and Concrete Composites*, Elsevier Ltd, 31(1), 72–76.

Ersoy, B., Evcin, A., Uygunoglu, T., Akdemir, Z. B., Brostow, W., and Wahrmund, J. (2014). “Zeta Potential-Viscosity Relationship in Kaolinite Slurry in the Presence of Dispersants.” *Arabian Journal for Science and Engineering*, 39(7), 5451–5457.

Esmaeilkhanian, B., Khayat, K. H., Yahia, a., and Feys, D. (2014). “Effects of mix design parameters and rheological properties on dynamic stability of self-consolidating concrete.” *Cement and Concrete Composites*, Elsevier Ltd, 54, 21–28.

Felekoğlu, B., Tosun, K., Baradan, B., Altun, A., and Uyulgan, B. (2006). “The effect of

fly ash and limestone fillers on the viscosity and compressive strength of self-compacting repair mortars.” *Cement and Concrete Research*, 36(9), 1719–1726.

Ferrari, L., Kaufmann, J., Winnefeld, F., and Plank, J. (2010). “Interaction of cement model systems with superplasticizers investigated by atomic force microscopy, zeta potential, and adsorption measurements.” *Journal of Colloid and Interface Science*, Elsevier Inc., 347(1), 15–24.

Ferraris, C., Billberg, P., Ferron, R., Feys, D., Hu, J., Kawashima, S., Koehler, E., Sonebi, M., Tanesi, J., and Tregger, N. (2017). “Role of Rheology in Achieving Successful Concrete Performance.” *Concrete International*, 39(6), 43–51.

Ferraris, C. F. (1999). “Measurement of the rheological properties of high performance concrete: State of the art report.” *Journal of Research of the National Institute of Standards and Technology*, 104(5), 461.

Ferraris, C. F., Obla, K. H., and Hill, R. (2001a). “The influence of mineral admixtures on the rheology of cement paste and concrete.” *Cement and Concrete Research*, 31(2), 245–255.

Ferraris, C., Larrard, F., and Martys, N. (2001b). “Fresh concrete rheology: recent developments.” *Materials Science of Concrete*, VI, 215–241.

Ferron, R. D., Shah, S., Fuente, E., and Negro, C. (2013). “Aggregation and breakage kinetics of fresh cement paste.” *Cement and Concrete Research*, Elsevier B.V., 50, 1–10.

Feys, D., and Asghari, A. (2019). “Influence of maximum applied shear rate on the

measured rheological properties of flowable cement pastes." *Cement and Concrete Research*, Elsevier, 117(January 2018), 69–81.

Feys, D., Cepuritis, R., Jacobsen, S., Lesage, K., Secrieru, E., and Yahia, A. (2017). "Measuring Rheological Properties of Cement Pastes: Most common Techniques, Procedures and Challenges." *RILEM Technical Letters*, 2(June 2018), 129–135.

Feys, D., De Schutter, G., Khayat, K. H., and Verhoeven, R. (2016). "Changes in rheology of self-consolidating concrete induced by pumping." *Materials and Structures/Materiaux et Constructions*, Springer Netherlands, 49(11), 4657–4677.

Feys, D., De Schutter, G., and Verhoeven, R. (2013). "Parameters influencing pressure during pumping of self-compacting concrete." *Materials and Structures/Materiaux et Constructions*, 46(4), 533–555.

Finger, F. B., González, M. S., and Kern, A. P. (2015). "Control of finished work - Final quality inspection in a social housing project." *Revista Ingenieria de Construccion*, 30(2), 147–153.

Flatt, R. J. (2004). "Dispersion forces in cement suspensions." *Cement and Concrete Research*, 34(3), 399–408.

Flatt, R. J., and Bowen, P. (2006). "Yodel: A yield stress model for suspensions." *Journal of the American Ceramic Society*, 89(4), 1244–1256.

Flatt, R. J., and Bowen, P. (2007). "Yield stress of multimodal powder suspensions: An extension of the YODEL (yield stress mODEL)." *Journal of the American Ceramic Society*, 90(4), 1038–1044.

Franks, G. V., Zhou, Z., Duin, N. J., and Boger, D. V. (2000). “Effect of interparticle forces on shear thickening of oxide suspensions.” *Journal of Rheology*, 44(4), 759–779.

Fuentes, M., Zúñiga, A., Díaz, M., Rocha, E., and Díaz, S. (2014). “Molienda mecánica por alta energía de minerales mexicanos para producir concreto de alto desempeño (CAD).” *Revista Ingenieria de Construccion*, 29(3), 256–269.

García-Alvarado, R., Martínez, A., González, L., and Auat, F. (2020). “Projections of 3D-printed construction in Chile.” *Revista ingeniería de construcción*, 35(1), 60–72.

Grzeszczyk, S., and Lipowski, G. (1997). “Effect of Content and Particle Size Distribution of High-Calcium Fly Ash on the Rheological Properties of Cement Pastes.” *Cement and Concrete Research*, 27(6), 907–916.

He, X., and Shi, X. (2008). “Chloride Permeability and Microstructure of Portland Cement Mortars Incorporating Nanomaterials.” *Transportation Research Record: Journal of the Transportation Research Board*, 2070(1), 13–21.

Honorio, T., Bary, B., Benboudjema, F., and Poyet, S. (2016). “Modeling hydration kinetics based on boundary nucleation and space-filling growth in a fixed confined zone.” *Cement and Concrete Research*, 83(March 2018), 31–44.

Hot, J., Bessaies-Bey, H., Brumaud, C., Duc, M., Castella, C., and Roussel, N. (2014). “Adsorbing polymers and viscosity of cement pastes.” *Cement and Concrete Research*, Elsevier Ltd, 63(October 2012), 12–19.

Huang, H., Huang, T., Yuan, Q., Zhou, D., Deng, D., and Zhang, L. (2019). “Temperature dependence of structural build-up and its relation with hydration kinetics of cement

paste.” *Construction and Building Materials*, Elsevier Ltd, 201, 553–562.

Jalal, M., Fathi, M., and Farzad, M. (2013). “Mechanics of Materia ls Effects of fly ash and TiO 2 nanoparticles on rheological , mechanical , microstructural and thermal properties of high strength self compacting concrete.” *INTERNATIONAL JOURNAL OF MECHANICS AND MATERIALS*, Elsevier Ltd, 61, 11–27.

Jallo, L. J., Chen, Y., Bowen, J., Etzler, F., and Dave, R. (2011). “Prediction of inter-particle adhesion force from surface energy and surface roughness.” *Journal of Adhesion Science and Technology*, 25(4–5), 367–384.

Jiao, D., Shi, C., Yuan, Q., An, X., Liu, Y., and Li, H. (2017). “Effect of constituents on rheological properties of fresh concrete-A review.” *Cement and Concrete Composites*, Elsevier Ltd, 83, 146–159.

Juenger, M. C. G., and Siddique, R. (2015). “Recent advances in understanding the role of supplementary cementitious materials in concrete.” *Cement and Concrete Research*, Elsevier Ltd, 78, 71–80.

Kashani, A., San, R., Qiao, G. G., Deventer, J. S. J. Van, and Provis, J. L. (2014). “Modelling the yield stress of ternary cement – slag – fl y ash pastes based on particle size distribution.” *Powder Technology*, Elsevier B.V., 266, 203–209.

Khan, S. U., Nuruddin, M. F., Ayub, T., and Shafiq, N. (2014). “Effects of different mineral admixtures on the properties of fresh concrete.” *The Scientific World Journal*, Hindawi Publishing Corporation, 2014(February).

Khayat, K. H., and Assaad, J. J. (2007). “Effect of w/cm and High-Range Water-Reducing

Admixture on Formwork Pressure and Thixotropy of Self-Consolidating Concrete." *ACI Materials Journal*, 21(103).

Khayat, K. H., and Feys, D. (2010). *Design, Production and Placement of Self-Consolidating Concrete*. Springer, Montreal, Canada.

Khayat, K. H., Omran, A. F., Naji, S., Billberg, P., and Yahia, A. (2012). "Field-oriented test methods to evaluate structural build-up at rest of flowable mortar and concrete." *Materials and Structures/Materiaux et Constructions*, 45(10), 1547–1564.

Kim, J. H., Han, S. H., and Choi, B. Il. (2020). "Influence of pumping pressure on the viscosity curve and rheological stability of mortar incorporating polycarboxylate." *Cement and Concrete Composites*, Elsevier Ltd, 105(February 2019), 103419.

Kim, J. H., Jang, H. R., and Yim, H. J. (2015). "Sensitivity and accuracy for rheological simulation of cement-based materials." *Computers and Concrete*, 15(6), 903–919.

Krieger, I. M., and Dougherty, T. J. (1959). "A Mechanism for Non-Newtonian Flow in Suspensions of Rigid Spheres." *Transactions of the Society of Rheology*, 3(1), 137–152.

De la Varga, I., Castro, J., Bentz, D. P., Zunino, F., and Weiss, J. (2018). "Evaluating the hydration of high volume fly ash mixtures using chemically inert fillers." *Construction and Building Materials*, Elsevier Ltd, 161, 221–228.

de Larrard, F., Ferraris, C. F., and Sedran, T. (1998). "Fresh concrete: A Herschel-Bulkley material." *Materials and Structures*, 31(7), 494–498.

Larson, R. G. (1999). *The Structure and Rheology of Complex Fluids*. Oxford University

Press Inc, New York.

Laskar, A. I., and Talukdar, S. (2008). “Rheological behavior of high performance concrete with mineral admixtures and their blending.” *Construction and Building Materials*, 22(12), 2345–2354.

Le, T. T., Austin, S. A., Lim, S., Buswell, R. A., Gibb, A. G. F., and Thorpe, T. (2012). “Mix design and fresh properties for high-performance printing concrete.” *Materials and Structures/Materiaux et Constructions*, 45(8), 1221–1232.

Lecompte, T., and Perrot, A. (2017). “Non-linear modeling of yield stress increase due to SCC structural build-up at rest.” *Cement and Concrete Research*, Elsevier Ltd, 92, 92–97.

Lee, S. H., Kim, H. J., Sakai, E., and Daimon, M. (2003). “Effect of particle size distribution of fly ash-cement system on the fluidity of cement pastes.” *Cement and Concrete Research*, 33(5), 763–768.

Lionberger, R. A. (2002). “Viscosity of bimodal and polydisperse colloidal suspensions.” *Physical Review E*, 65(6), 11.

Liu, D. M. (2000). “Particle packing and rheological property of highly-concentrated ceramic suspensions: φm determination and viscosity prediction.” *Journal of Materials Science*, 35(21), 5503–5507.

Lowke, D., and Gehlen, C. (2017). “The zeta potential of cement and additions in cementitious suspensions with high solid fraction.” *Cement and Concrete Research*, Elsevier Ltd, 95, 195–204.

Lu, C., Yang, H., and Mei, G. (2015). “Relationship between slump flow and rheological properties of self compacting concrete with silica fume and its permeability.” *Construction and Building Materials*, Elsevier Ltd, 75, 157–162.

Ma, G., and Wang, L. (2018). “A critical review of preparation design and workability measurement of concrete material for largescale 3D printing.” *Frontiers of Structural and Civil Engineering*, 12(3), 382–400.

Ma, S., Qian, Y., and Kawashima, S. (2018). “Experimental and modeling study on the non-linear structural build-up of fresh cement pastes incorporating viscosity modifying admixtures.” *Cement and Concrete Research*, Elsevier, 108(March), 1–9.

Mahmoodzadeh, F., and Chidiac, S. E. (2013). “Rheological models for predicting plastic viscosity and yield stress of fresh concrete.” *Cement and Concrete Research*, Elsevier Ltd, 49, 1–9.

Malaeb, Z., Hachem, H., Tourbah, A., Maalouf, T., El Zarwi, N., and Hamzeh, F. (2015). “3D Concrete Printing: Machine and Mix Design.” *International Journal of Civil Engineering and Technology*, 6(April), 14–22.

Malvern Instruments. (2012). *Understanding Yield Stress Measurements*.

Malvern Instruments Limited. (2015). *Overcoming and quantifying “Wall Slip” in measurements made on a rotational rheometer*.

Mantellato, S., Palacios, M., and Flatt, R. J. (2019). “Relating early hydration , specific surface and flow loss of cement pastes.” *Materials and Structures*, Springer Netherlands, 52(1), 1–17.

Mardani-Aghabaglou, A., Tuyan, M., Yilmaz, G., Ariöz, Ö., and Ramyar, K. (2013). "Effect of different types of superplasticizer on fresh, rheological and strength properties of self-consolidating concrete." *Construction and Building Materials*, Elsevier Ltd, 47, 1020–1025.

Maron, S. H., and Pierce, P. E. (1956). "Application of ree-eyring generalized flow theory to suspensions of spherical particles." *Journal of Colloid Science*, 11(1), 80–95.

Matos, P. R. de, Oliveira, A. L. de, Pelisser, F., and Prudêncio, L. R. (2018). "Rheological behavior of Portland cement pastes and self-compacting concretes containing porcelain polishing residue." *Construction and Building Materials*, Elsevier Ltd, 175, 508–518.

McKinsey Global Institute. (2017). "Reinventing Construction: A Route To Higher Productivity." *McKinsey & Company*, (February), 20.

Megid, W. A., and Khayat, K. H. (2017). "Bond strength in multilayer casting of self-consolidating concrete." *ACI Structural Journal*, 114(3), 467–476.

Megid, W. A., and Khayat, K. H. (2019). "Effect of structural buildup at rest of self-consolidating concrete on mechanical and transport properties of multilayer casting." *Construction and Building Materials*, Elsevier Ltd, 196, 626–636.

Mehdipour, I., and Khayat, K. H. (2017). "Effect of particle-size distribution and specific surface area of different binder systems on packing density and flow characteristics of cement paste." *Cement and Concrete Composites*, Elsevier Ltd, 78, 120–131.

Mo, K. H., Ling, T.-C., Alengaram, U. J., Yap, S. P., and Yuen, C. W. (2017). "Overview

of supplementary cementitious materials usage in lightweight aggregate concrete." *Construction and Building Materials*, Elsevier Ltd, 139, 403–418.

Montgomery, D., and Runger, G. (2014). *Applied Statistics and Probability for Engineers*. Wiley and Sons, Hoboken, NJ.

Montgomery, D., and Runger, G. C. (2003). *Applied Statistics and Probability for Engineers*. Wiley, Phoenix.

Mostafa, A. M., and Yahia, A. (2016). "New approach to assess build-up of cement-based suspensions." *Cement and Concrete Research*, Elsevier Ltd, 85, 174–182.

Mostafa, A. M., and Yahia, A. (2017). "Physico-chemical kinetics of structural build-up of neat cement-based suspensions." *Cement and Concrete Research*, Elsevier Ltd, 97, 11–27.

Nägele, E. (1986). "The Zeta-potential of cement part II: Effect of ph-value." *Cement and Concrete Mineral Admixtures*, 16(c), 853–863.

Narasimha Reddy, P., and Kavyateja, B. V. (2020). "Durability performance of high strength concrete incorporating supplementary cementitious materials." *Materials Today: Proceedings*, Elsevier Ltd, (xxxx).

Navarrete, I., Hube, M. A., Kurama, Y., and Lopez, M. (2017a). "Flexural behavior of stratified reinforced concrete: construction, testing, analysis, and design." *Materials and Structures/Materiaux et Constructions*, 50(4).

Navarrete, I., Hube, M. A. M. A., Kurama, Y., and Lopez, M. (2017b). "Flexural behavior of stratified reinforced concrete: construction, testing, analysis, and design."

Materials and Structures/Materiaux et Constructions, 50(4).

Navarrete, I., Kurama, Y., Escalona, N., and Lopez, M. (2020). "Impact of physical and physicochemical properties of supplementary cementitious materials on structural build-up of cement-based pastes." *Cement and Concrete Research*, Elsevier, 130(January), 105994.

Navarrete, I., and Lopez, M. (2016). "Estimating the segregation of concrete based on mixture design and vibratory energy." *Construction and Building Materials*, Elsevier Ltd, 122, 384–390.

Navarrete, I., and Lopez, M. (2017). "Understanding the relationship between the segregation of concrete and coarse aggregate density and size." *Construction and Building Materials*, 149.

NIST/SEMATECH. (2012). "e-Handbook of Statistical Methods." <https://www.itl.nist.gov/div898/handbook/index.htm> (Aug. 6, 2019).

Oey, T., Kumar, A., Bullard, J. W., Neithalath, N., and Sant, G. (2013). "The filler effect: The influence of filler content and surface area on cementitious reaction rates." *Journal of the American Ceramic Society*, 96(6), 1978–1990.

Ohshima, H., and Makino, K. (2014). *Colloid and Interface Science in Pharmaceutical Research and Development*. Elsevier.

Ojeda-Farías, O., Hebraud, P., Lootens, D., Liard, M., and Mendoza-Rangel, J. M. (2019). "Thixotropy of reactive suspensions: The case of cementitious materials." *Construction and Building Materials*, 212, 121–129.

Ouyang, J., Han, B., Cheng, G., Zhao, L., and Ou, J. (2018). “A viscosity prediction model for cement paste with nano-SiO2 particles.” *Construction and Building Materials*, 185, 293–301.

Pacheco-Torgal, F., Jalali, S., Labrincha, J., and John, V. M. (2013). *Eco-Efficient Concrete*. Woodhead Publishing, Cambridge, UK.

Panda, B., Wei Tay, Y., Chandra Paul, S., Fai Leong, K., Jen, T. M., and Gibson, I. (2016). “Current Challenges and Future Perspectives of 3D Concrete Printing.” *2nd International Conference on Progress in Additive Manufacturing*, (May), 16–19.

Park, C. K., Noh, M. H., and Park, T. H. (2005). “Rheological properties of cementitious materials containing mineral admixtures.” *Cement and Concrete Research*, 35(5), 842–849.

PCA. (2018). “Chemical admixtures.” <https://www.cement.org/cement-concrete-applications/concrete-materials/chemical-admixtures>.

Perrot, A., Rangeard, D., and Pierre, A. (2016). “Structural built-up of cement-based materials used for 3D-printing extrusion techniques.” *Materials and Structures*, Springer Netherlands, 1213–1220.

Petit, J., Khayat, K. H., and Wirquin, E. (2006). “Coupled effect of time and temperature on variations of yield value of highly flowable mortar.” 36, 832–841.

Petit, J. Y., Wirquin, E., Vanhove, Y., and Khayat, K. (2007). “Yield stress and viscosity equations for mortars and self-consolidating concrete.” *Cement and Concrete Research*, 37(5), 655–670.

Petrou, M. F., Harries, K. A., Gadala-Maria, F., and Kolli, V. G. (2000). "A unique experimental method for monitoring aggregate settlement in concrete." *Cement and Concrete Research*, 30(5), 809–816.

Pierre, A. P. A., and Picandet, S. V. V. (2015). "Prediction of lateral form pressure exerted by concrete at low casting rates." *Materials and Structures*, Springer Netherlands, 2315–2322.

Proverbs, D. G., Holt, G. D., and Olomolaiye, P. O. (1999). "Productivity rates and construction methods for high rise concrete construction: A comparative evaluation of UK, German and French contractors." *Construction Management and Economics*, 17(1), 45–52.

Qian, Y., and Kawashima, S. (2018). "Distinguishing dynamic and static yield stress of fresh cement mortars through thixotropy." *Cement and Concrete Composites*, Elsevier Ltd, 86, 288–296.

Ravina, L. (1998). *Everything you want to know about Coagulation & Flocculation ....* Zeta-Meter, Inc., Staunton, Virginia.

Romero, C. P., Jeldres, R. I., Quezada, G. R., Concha, F., and Toledo, P. G. (2018). "Zeta potential and viscosity of colloidal silica suspensions: Effect of seawater salts, pH, flocculant, and shear rate." *Colloids and Surfaces A: Physicochemical and Engineering Aspects*, Elsevier, 538(August 2017), 210–218.

Roussel, N. (2006). "A thixotropy model for fresh fluid concretes: Theory, validation and applications." *Cement and Concrete Research*, 36(10), 1797–1806.

Roussel, N. (2012). *Understanding the rheology of concrete*. *Understanding the Rheology of Concrete*, (N. Roussel, ed.), Woodhead Publishing, Philadelphia.

Roussel, N., and Cussigh, F. (2008). "Distinct-layer casting of SCC: The mechanical consequences of thixotropy." *Cement and Concrete Research*, 38(5), 624–632.

Roussel, N., Lemaître, A., Flatt, R. J., and Coussot, P. (2010). "Steady state flow of cement suspensions: A micromechanical state of the art." *Cement and Concrete Research*, Elsevier Ltd, 40(1), 77–84.

Roussel, N., Ovarlez, G., Garrault, S., and Brumaud, C. (2012). "The origins of thixotropy of fresh cement pastes." *Cement and Concrete Research*, Elsevier Ltd, 42(1), 148–157.

Roussel, N., Staquet, S., Schwarzentruber, L. D. A., Le Roy, R., and Toutlemonde, F. (2007). "SCC casting prediction for the realization of prototype VHPC-precambered composite beams." *Materials and Structures/Materiaux et Constructions*, 40(9), 877–887.

Rubio-Hernández, F. J. (2018). "Rheological behavior of fresh cement pastes." *Fluids*, 3(4).

Saleh Ahari, R., Kemal Erdem, T., and Ramyar, K. (2015). "Effect of various supplementary cementitious materials on rheological properties of self-consolidating concrete." *Construction and Building Materials*, Elsevier Ltd, 75, 89–98.

Saleh, R., Kemal, T., and Ramyar, K. (2015). "Thixotropy and structural breakdown properties of self consolidating concrete containing various supplementary

cementitious materials.” *CEMENT AND CONCRETE COMPOSITES*, Elsevier Ltd, 59, 26–37.

Sant, G., Ferraris, C. F., and Weiss, J. (2008). “Rheological properties of cement pastes : A discussion of structure formation and mechanical property development.” *Cement and Concrete Research*, Elsevier Ltd, 38(11), 1286–1296.

Scherer, G. W., Zhang, J., and Thomas, J. J. (2012). “Nucleation and growth models for hydration of cement.” *Cement and Concrete Research*, Elsevier Ltd, 42(7), 982–993.

Schneider, M., Romer, M., Tschudin, M., and Bolio, H. (2011). “Sustainable cement production—present and future.” *Cement and Concrete Research*, 41(7), 642–650.

Secrieru, E., Mohamed, W., Fataei, S., and Mechtcherine, V. (2020). “Assessment and prediction of concrete flow and pumping pressure in pipeline.” *Cement and Concrete Composites*, Elsevier Ltd, 107(November 2019), 103495.

Shen, L., Bahrami Jovein, H., Sun, Z., Wang, Q., and Li, W. (2015). “Testing dynamic segregation of self-consolidating concrete.” *Construction and Building Materials*, Elsevier Ltd, 75, 465–471.

Shen, L., Jovein, H. B., and Li, M. (2014). “Measuring static stability and robustness of self-consolidating concrete using modified Segregation Probe.” *Construction and Building Materials*, 70, 210–216.

Shen, L., Struble, L., and Lange, D. (2009). “Modeling dynamic segregation of self-consolidating concrete.” *ACI Materials Journal*, 106(4), 375–380.

Shen, Y., Wang, Y., Yang, Y., Sun, Q., Luo, T., and Zhang, H. (2019). “Influence of

surface roughness and hydrophilicity on bonding strength of concrete-rock interface." *Construction and Building Materials*, Elsevier Ltd, 213, 156–166.

Shirzadi Javid, A. A., Ghoddousi, P., Ghodrati Amiri, G., and Donyadideh, K. (2019). "A new photogrammetry method to study the relationship between thixotropy and bond strength of multi-layers casting of self-consolidating concrete." *Construction and Building Materials*, Elsevier Ltd, 204, 530–540.

Snee, R. D. (1977). "Validation of Regression Models: Methods and Examples." *Technometrics*, 19(4), 415–428.

Solak, A. M., Tenza-Abril, A. J., and Baeza-Brotons, F. (2018). "Image analysis applications for the study of segregation in lightweight concretes." *International Journal of Computational Methods and Experimental Measurements*, 6(4), 835–846.

Sonebi, M., and Amziane, S. (2017). "3D Printing of Fibre Cement-Based Materials: Fresh and Rheological Performances." *2nd International Conference On bio-Based Building Materials*.

Srinivasan, S., Barbhuiya, S. A., Charan, D., and Pandey, S. P. (2010). "Characterising cement-superplasticiser interaction using zeta potential measurements." *Construction and Building Materials*, Elsevier Ltd, 24(12), 2517–2521.

Stern, O. (1924). "Zur Theorie der Elektrolytischen Doppelschicht." *Zeitschrift für Elektrochemie*, 30(508), 508–516.

Struble, L., and Sun, G. K. (1995). "Viscosity of Portland cement paste as a function of concentration." *Advanced Cement Based Materials*, 2(2), 62–69.

Sun, A., and Gunasekaran, S. (2009). *Yield stress in foods: Measurements and applications*. *International Journal of Food Properties*.

Tattersall, G. H., and Baker, P. H. (1988). "The effect of vibration on the rheological properties of fresh concrete." *Magazine of Concrete Research*, 40(143), 79–89.

Tattersall, G. H., and Banfill, P. F. G. (1983). *The Rheology of Fresh Concrete*. Pitman Books Limited, London, England.

Thomas, J. J. (2007). "A new approach to modeling the nucleation and growth kinetics of tricalcium silicate hydration." *Journal of the American Ceramic Society*, 90(10), 3282–3288.

Vance, K., Kumar, A., Sant, G., and Neithalath, N. (2013). "The rheological properties of ternary binders containing Portland cement, limestone, and metakaolin or fly ash." *Cement and Concrete Research*, Elsevier Ltd, 52, 196–207.

Vanhove, Y., Helnan-Moussa, B., and Wirquin, E. (2013). "Effect of temperature on the thixotropic behaviour of self-consolidating concrete." *Magazine of Concrete Research*, 65(1), 52–62.

Vargas, R., and Sciaraffia, R. (2006). "Diseño y evaluación de hormigones autocompactantes (HAC)." *Ingeniería de Construcción*, 21(1), 57–70.

Verdugo, M., Cal, M., and Fernández, C. (2005). *Análisis Econométrico: Una Aproximación Práctica con Shazam*. DELTA.

Verwey, E. J. W. (1947). "Theory of the stability of lyophobic colloids." *Journal of Physical and Colloid Chemistry*, 51(3), 631–636.

Wallevik, O. H., Feys, D., Wallevik, J. E., and Khayat, K. H. (2015). "Avoiding inaccurate interpretations of rheological measurements for cement-based materials." *Cement and Concrete Research*, Elsevier Ltd.

Wangler, T., Lloret, E., Reiter, L., Hack, N., Gramazio, F., Kohler, M., Bernhard, M., Dillenburger, B., Buchli, J., Roussel, N., and Flatt, R. (2016). "Digital Concrete: Opportunities and Challenges." *RILEM Technical Letters*, 1, 67.

Yahia, A., and Khayat, K. H. (2001). "Analytical models for estimating yield stress of high-performance pseudoplastic grout." *Cement and Concrete Research*, 31(5), 731–738.

Yim, H. J., Kim, J. H., and Shah, S. P. (2013). "Cement particle flocculation and breakage monitoring under Couette flow." *Cement and Concrete Research*, Elsevier Ltd, 53, 36–43.

Youness, D., Mechaymech, A., and Al Wardany, R. (2020). "Flow assessment and development towards sustainable self-consolidating concrete using blended basalt and limestone-cement systems." *Journal of Cleaner Production*, Elsevier Ltd.

Yuan, Q., Zhou, D., Khayat, K. H., Feys, D., and Shi, C. (2017). "On the measurement of evolution of structural build-up of cement paste with time by static yield stress test vs. small amplitude oscillatory shear test." *Cement and Concrete Research*, Elsevier, 99(September 2016), 183–189.

Yuan, Q., Zhou, D., Li, B., Huang, H., and Shi, C. (2018). "Effect of mineral admixtures on the structural build-up of cement paste." *Construction and Building Materials*, Elsevier Ltd, 160, 117–126.

Yun, K., Choi, S., and Heum, J. (2015). "Effects of admixtures on the rheological properties of high-performance wet-mix shotcrete mixtures." *Construction and Building Materials*, Elsevier Ltd, 78, 194–202.

Zeta-Meter Inc. (1997). *The Interaction of Colloids*. *Technial Note*.

Zhang, J., Weissinger, E. A., Peethamparan, S., and Scherer, G. W. (2010). "Early hydration and setting of oil well cement." *Cement and Concrete Research*, Elsevier Ltd, 40(7), 1023–1033.

Zhao, Y., Xing, W., Xu, N., and Wong, F. (2005). "Effects of inorganic electrolytes on zeta potentials of ceramic microfiltration membranes." 42(71), 117–121.

Zhou, Z., Solomon, M. J., Scales, P. J., and Boger, D. V. (1999). "The yield stress of concentrated flocculated suspensions of size distributed particles." *Journal of Rheology*, 43(3), 651–671.

Zhu, J., Shu, X., Tang, J., Li, T., Ran, Q., and Liu, J. (2020). "Effect of microfines from manufactured sand on yield stress of cement paste." *Construction and Building Materials*, Elsevier Ltd, 120987.